

Summer 8-28-2011

FUNCTIONAL TWO-DIMENSIONAL ELECTRONIC GASES AT INTERFACES OF OXIDE HETEROSTRUCTURES

Yong Wang

University of Nebraska-Lincoln, tumble2000cn@gmail.com

Follow this and additional works at: <http://digitalcommons.unl.edu/physicsdiss>

 Part of the [Condensed Matter Physics Commons](#)

Wang, Yong, "FUNCTIONAL TWO-DIMENSIONAL ELECTRONIC GASES AT INTERFACES OF OXIDE HETEROSTRUCTURES" (2011). *Theses, Dissertations, and Student Research: Department of Physics and Astronomy*. 13.
<http://digitalcommons.unl.edu/physicsdiss/13>

This Article is brought to you for free and open access by the Physics and Astronomy, Department of at DigitalCommons@University of Nebraska - Lincoln. It has been accepted for inclusion in Theses, Dissertations, and Student Research: Department of Physics and Astronomy by an authorized administrator of DigitalCommons@University of Nebraska - Lincoln.

FUNCTIONAL TWO-DIMENSIONAL ELECTRONIC GASES AT INTERFACES OF
OXIDE HETEROSTRUCTURES

By

Yong Wang

A DISSERTATION

Presented to the Faculty of

The Graduate College at University of Nebraska

In Partial Fulfillment of Requirements

For the Degree of Doctor of Philosophy

Major: Physics and Astronomy

Under the Supervision of Professor Evgeny Y. Tsymbal

Lincoln, Nebraska

August, 2011

FUNCTIONAL TWO-DIMENSIONAL ELECTRONIC GASES AT INTERFACES OF
OXIDE HETEROSTRUCTURES

Yong Wang, PhD

University of Nebraska, 2011

Adviser: Evgeny Y. Tsymbal

A quasi-two dimensional electron gas (2DEG) in oxide heterostructures such as $\text{LaAlO}_3/\text{SrTiO}_3$ has unique properties that are promising for applications in all-oxide electronic devices. In this dissertation, we focus on understanding and predicting novel properties of the 2DEG by performing first-principles electronic calculations within the frame work of density-functional theory (DFT). The investigation is made upon adding new functionalities in oxide heterostructures, such as ferroelectric polarization, epitaxial strain, and spin polarization that can be employed to control 2DEG properties.

Based on first-principles calculations the effects of different polarization magnitudes and alignments in all-oxide heterostructures incorporating different ferroelectric constituents, such as $\text{KNbO}_3/\text{ATiO}_3$ ($A = \text{Sr, Ba, Pb}$), are investigated. It is found that screening charge at the interface that counteracts the depolarizing electric field in the ferroelectric material significantly changes the free electron density of 2DEG at the interface. Using this mechanism, nonvolatile metal-insulating transition can be achieved at the interface by switching the ferroelectric spontaneous polarization.

Growing on different substrates, $\text{LaAlO}_3/\text{SrTiO}_3$ heterostructures experience different epitaxial strains. Our first-principles calculations reveal that compressive epitaxial strain introduces a polarization in SrTiO_3 pointing away from the interface, which is consistent with the experimental observations. This polarization strongly affects the 2DEG carrier density through a polarization charge formed at the interface. Our theoretical investigation finds that the critical thickness to form a 2DEG at the interface of the heterostructure increases with the compressive strain, while the saturated carrier density decreases which is consistent with the experimental results.

Adding a spin degree of freedom to 2DEG may be interesting for the application of 2DEGs in a spintronic device. We explore a $\text{LaAlO}_3/\text{EuO}$ interface as a potential candidate to create a spin-polarized 2DEG. The exchange splitting of unoccupied Eu-5*d* conduction band in bulk EuO makes it possible to realize spin-polarized 2DEG. We predict that $\text{LaAlO}_3/\text{EuO}$ interface forms a spin-polarized 2DEG with spin polarization of about 50%. We hope that this prediction will stimulate experimental investigations to achieve the spin-polarized 2DEG.

Acknowledgements

I would like to thank all the friends, colleagues and my family for their support and guidance during my doctoral studies.

First and foremost, I would like to thank my advisor, Professor Evgeny Tsymbal. He provided an excellent guidance on my graduate research and dissertation. I am greatly influenced and educated by his strong interest in physics, erudite scientific knowledge, and perspective physical intuition. He provided many opportunities for me to participate in different research projects and obtain experience of writing proposals and applications for fellowship. I sincerely appreciate his support and interest in my scientific development and future career.

I would like to thank Professor Sitaram Jaswal, Professor Peter Dowben, and Professor Mathias Schubert for serving on my Supervisory Committee. I am grateful to them for their careful and critical reading of this dissertation.

I would like to thank Professor Sitaram Jaswal for his insightful comments and helpful discussion during my doctoral studies, as well as for collaborating with me on the work presented in Chapter 3.

I am indebted to Professor Manish Niranjana from Indian Institute of Technology Hyderabad for instructing me in VASP simulation package, and for many helpful discussions we had during his work in the group of Professor Evgeny Tsymbal, as well as collaborating with me on majority of the research projects presented in this dissertation.

I would like to thank Professor Kirill Belashchenko and Dr. Joonhee An for helping me with the LDA+U calculations of bulk EuO, as well as collaborating with me on the work presented in Chapter 5.

I am grateful for helpful and interesting discussions with Professor J.D. Burton during my graduate studies, as well as collaborating with me on the work presented in Chapter 5.

The experiments on strain effect on 2DEG presented in Chapter 4 were led by Professor Chang-Beom Eom and performed by Dr. Chung Wung Bark, Dr. H. W. Jang, C. M. Folkman, Dr. J. W. Park, Dr. Seung Hyub Baek, Mr. David A Felker and Professor Mark Rzchowski from University of Wisconsin-Madison, in collaboration with Dr. Y. Zhang, Professor Xiaoqing Pan from University of Michigan, Dr. H. Zhou and Dr. Dillon Fong from Argonne National Laboratory. I am grateful for having the opportunity to make contribution to their research project as well as another one not presented in this dissertation.

The following people also deserve my thanks for collaborating with me on other research projects that are not presented in this dissertation: Dr. Mikhail Zhuravlev, Professor Sadamichi Maekawa, Professor Julian Velev, Professor Alexei Gruverman, Mr. Dong Wu, Mr. Haidong Lu, Mr. C. T. Nelson, Mr. D. Su, Mr. Sanghan Lee, Ms. Karolina Janicka and Mr. Y. Zhu.

The work presented in this dissertation was supported by the National Science Foundation (Grant No. DMR-0906443), the Nanoelectronic Research Initiative through the Materials Research Science and Engineering Center at the University of Nebraska

(NSF-DMR under Grant No. 0820521), and the Nebraska Research Initiative. Computations were performed utilizing the Research Computing Facility of the University of Nebraska-Lincoln.

At last but not the least, I would like to thank my wife Lingmei and our daughter Nicky. I was motivated by their love. Their support during my whole doctoral studies is so important to keep me on pace. I am also very grateful to my parents and parents-in-law for their great support.

Contents

Chapter 1	Introduction	1
1.1	Oxide heterostructures	1
1.2	2DEG at oxide interfaces	5
1.3	Motivation and organization of this dissertation	13
Chapter 2	Theoretical methods	17
2.1	Many-body Schrödinger equation	17
2.2	Kohn-Sham equation	18
2.3	LDA and GGA approximations	21
2.4	LDA+U approximation	23
2.5	Plane wave pseudopotential methods	26
2.6	Vienna Ab-initio Simulation Package (VASP)	30
Chapter 3	Ferroelectric polarization effect on 2DEG	32
3.1	Introduction	33
3.1.1	Ferroelectricity in perovskite oxides	33
3.1.2	Field controlled 2DEG	35
3.2	Theoretical approach	38
3.2.1	Computational method	38

3.2.2	Properties of bulk perovskites SrTiO ₃ , KNbO ₃ , BaTiO ₃ and PbTiO ₃ ···	39
3.2.3	Structural model for superlattice	40
3.3	Results and discussion	43
3.3.1	SrTiO ₃ /KNbO ₃	43
3.3.2	PbTiO ₃ /KNbO ₃	53
3.3.3	BaTiO ₃ /KNbO ₃	58
3.4	Summary	65
Chapter 4 Strain effect on 2DEG		67
4.1	Introduction	68
4.2	Experimental investigation	68
4.3	Theoretical studies	75
4.4	Summary	84
Chapter 5 Spin-polarized 2DEG		86
5.1	Introduction	86
5.1.1	Overview of spin-polarized 2DEG	86
5.1.2	Ferromagnetic insulator EuO	87
5.2	Spin-polarized 2DEG in EuO based heterostructure	89
5.2.1	LaAlO ₃ /EuO	90
5.2.2	EuO/LaO/EuO	100

5.3 Summary	103
References	104
Publications	123
Presentations	125

List of Figures

- Figure 1.1 High-resolution TEM image of LaAlO₃ on SrTiO₃ (STO) on (LaAlO₃)_{0.3}–(Sr₂AlTaO₆)_{0.7} (LSAT). Intensity differences between LaAlO₃ and SrTiO₃ layers and the individual La and Sr atoms are clearly seen.
- Figure 1.2 LaAlO₃ thickness dependence of the electronic properties of the LaAlO₃/SrTiO₃ interfaces. (A) Sheet conductance and (B) carrier density of the heterostructures plotted as a function of the number of LaAlO₃ unit cells. The data showed in blue and red are those of samples grown at 770-C and 815-C, respectively. The data were taken at 300 K .
- Figure 1.3 Illustration of heterostructure with (LaO)⁺/(TiO₂)⁰ interface showing the atomic arrangement and ionic charge for each layer.
- Figure 1.4 Schematic of the polar catastrophe at the n-type interface of LaAlO₃/SrTiO₃ heterostructure. (a). Before electronic reconstruction, alternating positive and negative atomic layers produce on average a constant electric field in LaAlO₃. The potential increases with the thickness of LaAlO₃. (b) -0.5e is transferred to TiO₂ layers, alternating electric fields form at LaAlO₃, and the overall effective electric field in LaAlO₃ is zero.
- Figure 1.5 Schematic band diagrams for the SrTiO₃/LaAlO₃ heterostructures with thickness smaller and larger than the critical thickness. (a) When the LaAlO₃

thickness is smaller than the critical thickness, the valence band maximum (VBM) of LaAlO_3 on the surface lies below the conduction band minimum (CBM) of SrTiO_3 at the interface and no charge is transferred. (b) When the LaAlO_3 thickness exceeds the critical thickness, VBM of LaAlO_3 on the surface lies above the CBM of SrTiO_3 at the interface and charge is transferred from the surface layer of LaAlO_3 , i.e. AlO_2 to the interface layer of SrTiO_3 , i.e. TiO_2 . The red dashed line indicates the position of the Fermi energy. Ref. [52]

Figure 3.1 (a) cubic perovskite structure ABO_3 . B (gray) is at center of oxygen (red) octahedron. A (blue) is at the center of a hole formed by these octahedral. (b) ferroelectric tetragonal phase of ABO_3 in (010) direction.

Figure 3.2 $(\text{NbO}_2)^+ / (\text{AO})^0$ interface in $\text{KNbO}_3 / \text{ATiO}_3$ heterostructure (a) as an analogue of $(\text{LaO})^+ / (\text{TiO}_2)^0$ interface in $\text{LaAlO}_3 / \text{SrTiO}_3$ heterostructure (b).

Figure 3.3 Atomic structure of the unit cell and the $(\text{NbO}_2)^+ / (\text{AO})^0$ interfaces in a $(\text{KNbO}_3)_{8.5} / (\text{ATiO}_3)_{8.5}$ (001) superlattice with parallel (a) and antiparallel (b) polarization indicated by white and black arrows respectively.

Figure 3.4 Layer-projected density of states (DOS) on 4d-orbitals of Nb atoms (a, b, c) and 3d-orbitals of Ti atoms (d, e, f) located at different NbO_2 or TiO_2 monolayers l or k from the $(\text{NbO}_2)^+ / (\text{SrO})^0$ interface respectively in the $(\text{KNbO}_3)_{8.5} / (\text{SrTiO}_3)_{8.5}$ superlattice for either interface in the paraelectric state (a, d), the right interface (b, e) and the left interface (c, f) in the ferroelectric state. The shaded plots are the DOS of atoms in the central monolayer. The zero

along the horizontal axis refers to the Fermi energy.

Figure 3.5 Cation (Nb, Ti, K, Sr) displacements with respect to oxygen anions in $(\text{KNbO}_3)_{8.5}/(\text{SrTiO}_3)_{8.5}$ superlattice with eight middle monolayers of SrTiO_3 fixed (a), with all the ions fully relaxed (b) and displacements of all the ions in fully relaxed ferroelectric state (c). Open and solid symbols in (a) and (b) indicate Sr-O (K-O) and Ti-O₂ (Nb-O₂) displacements, respectively. Solid circles and squares in (c) indicate Sr (K) and Ti (Nb) displacements respectively. Open circles and squares in (c) indicate displacements of O atoms in SrO (KO) and TiO₂ (NbO₂) layers, respectively. The two dashed vertical lines indicate left and right NbO₂/SrO interfaces.

Figure 3.6 The free charge (in units of electron) on Nb and Ti atoms across the unit cell of $(\text{KNbO}_3)_{8.5}/(\text{SrTiO}_3)_{8.5}$ superlattices in paraelectric state and ferroelectric state when the middle layers in SrTiO_3 is fixed (a) and all the ions are fully relaxed (b). The screening charge is obtained by calculating the difference of the free charges on Nb and Ti atoms for ferroelectric and paraelectric states. The directions of polarization for the ferroelectric state are from left to right.

Figure 3.7 Layer-projected density of states (DOS) on 4d-orbitals of Nb atoms (a,b,c) and 3d-orbitals of Ti atoms (d,e,f) located in different monolayers l and k respectively from the $(\text{NbO}_2)^+ / (\text{PbO})^0$ interface in the $(\text{KNbO}_3)_{8.5}/(\text{PbTiO}_3)_{8.5}$ superlattice for either interface in the paraelectric state (a, d), the right interface (b, e) and the left interface (c, f) in the ferroelectric state. Layer number

indicates the layer from the interface. The shaded plots are the DOS of atoms in the central monolayer. The zero along the horizontal axis refers to the Fermi energy

Figure 3.8 Cation (Nb, Ti, K, Pb) displacements with respect to oxygen anions in $(\text{KNbO}_3)_{8.5}/(\text{PbTiO}_3)_{8.5}$ superlattice. Open and solid symbols indicate Pb-O (K-O) and Ti-O₂ (Nb-O₂) displacements, respectively. The two dashed vertical lines indicate left and right $(\text{NbO}_2)^0/(\text{PbO})^0$ interfaces.

Figure 3.9 The free charge (in units of electron) on Nb and Ti atoms across the unit cell of $(\text{KNbO}_3)_{8.5}/(\text{PbTiO}_3)_{8.5}$ superlattices in paraelectric state and ferroelectric state. The screening charge is the difference of the free charges on Nb and Ti atoms for the ferroelectric and paraelectric states. The direction of polarization for the ferroelectric state is from left to right.

Figure 3.10 Layer-projected density of states (DOS) on 4d-orbitals of Nb atoms (a,b,c) and 3d-orbitals of Ti atoms (d,e,f) located in different monolayers l and k respectively away from the $(\text{NbO}_2)^+/(\text{BaO})^0$ interface in the $(\text{KNbO}_3)_{8.5}/(\text{BaTiO}_3)_{8.5}$ superlattice for either interface in the paraelectric state (a, d), the right interface (b, e) and the left interface (c, f) in the ferroelectric state. Layer number indicates the layer from the interface. The shaded plots are the DOS of atoms in the central monolayer. The zero along the horizontal axis refers to the Fermi energy.

Figure 3.11 Cation (Nb, Ti, K, Ba) displacements with respect to oxygen anions in

$(\text{KNbO}_3)_{8.5}/(\text{BaTiO}_3)_{8.5}$ superlattice with parallel polarizations pointing from left to right (a) and with antiparallel polarizations pointing toward each other (b). Open and solid symbols indicate Ba-O (K-O) and Ti-O₂ (Nb-O₂) displacements respectively. The two dashed vertical lines indicate left and right $(\text{NbO}_2)^0/(\text{BaO})^0$ interfaces.

Figure 3.12 The free charge (in units of electron) on Nb and Ti atoms across the unit cell of $(\text{KNbO}_3)_{8.5}/(\text{BaTiO}_3)_{8.5}$ superlattices in paraelectric state and ferroelectric state with (a) polarizations in the same direction from left to right and (b) opposite polarizations. The screening charge is the difference of the free charges on Nb and Ti atoms for ferroelectric and paraelectric states.

Figure 4.1 Schematic diagram of grown structures. Thickness of LaAlO₃ layer was varied from 1 to 30 unit cells on STO on LSAT, NGO, Si, DSO, GSO substrate

Figure 4.2 Effect of strain on 2DEG. (A) Critical thickness of LaAlO₃ under bi-axial strain. While all others samples have a 50 unit cell-thick SrTiO₃ layer, sample LAO/STO/Si has 100nm-thick STO and is the nominally unstrained STO layer on silicon. The conductivity versus thickness of LaAlO₃ in the LAO/STO interface on various substrates is given in the inset. (B) Room-temperature carrier concentrations at the LAO/STO interface under various biaxial strains. The carrier concentrations in tensile strain state were above our measurement limit.

Figure 4.3 The calculated atomic structure of unstrained (A) and compressively strained

(B) LaAlO_3 (3 unit cell.)/ SrTiO_3 system. In Figure B Ti-O and Sr-O displacements are amplified by a factor of eight as compared to the calculated results for visual comprehension. The left and right panels show schematically the 2DEG formation and the effect of the polarization P in the strained SrTiO_3 on the 2DEG as described in text.

Figure 4.4 The symmetric atomic structure of $(\text{LaAlO}_3)_3/(\text{SrTiO}_3)_5$ separated by a 8 Å thick vacuum gap.

Figure 4.5 B (Ti, Al) c-site atom – oxygen (O) atom displacements in the unstrained (squares), 1.2% (circles) and 2% (half circle) compressively strained $(\text{LaAlO}_3)_3/(\text{SrTiO}_3)_5$ structure.

Figure 4.6: Density of electronic states at the TiO_2 monolayer located at the interface of the unstrained, and the -2% strained $(\text{LaAlO}_3)_3/(\text{SrTiO}_3)_5$ structure. The vertical line indicates the position of the Fermi energy. The filled area under the curve for the unstrained system indicates the free electron charge responsible for the formation of the 2DEG. The strain eliminates this charge making the system insulating.

Figure 5.1 Rocksalt crystal structure of EuO.

Figure 5.2 The density of states (DOS) of bulk EuO for different orbitals. The positive and negative values show the DOS for the spin-up and spin-down electrons, respectively. Fermi energy is located at zero, indicated by the dashed line.

Figure 5.3 Atomic structure of the LaO/EuO interface in the $(\text{LaAlO}_3)_{8.5}/(\text{EuO})_{15}$ (001)

superlattice containing 8.5 unit cells of LaAlO_3 and 15 monolayers of EuO within the supercell. Indices l and m denote atomic monolayers and are increasing with separation from the interface. $l = 8$ in EuO and $m = 9$ in LaAlO_3 correspond the middle of the respective layers.

Figure 5.4 The density of state (DOS) of bulk EuO under strain by LaAlO_3 (blue) and without strain (red).

Figure 5.5 Atomic displacements in the $(\text{LaAlO}_3)_{8.5}/(\text{EuO})_{15}$ (001) superlattice with respect to the atomic “bulk” positions. The latter are determined by fixing the in-plane lattice constant and optimizing the interlayer distance, as described in text. The vertical lines indicate interfaces.

Figure 5.6 Layer- and spin-resolved density of states (DOS) on EuO (a) LaO (b) and AlO_2 (c) monolayers located at different planes l and m away from the LaO/EuO interface (as labeled in Figure.1). Top (bottom) panels show the majority(minority)-spin. In panel (a) the majority-spin states at energies below -1eV are the occupied Eu-4f states. The vertical lines denote the Fermi energy (E_F).

Figure 5.7 Spin-dependent charge distribution across the $(\text{LaAlO}_3)_{8.5}/(\text{EuO})_{15}$ (001) supercell. The notation for the atomic layers is the same as in Figure.1. The dashed lines indicate interfaces.

Figure 5.8 Atomic structure of $\text{LaO}/(\text{EuO})_{19}$ (001) superlattice containing one monolayer LaO and 19 monolayers of EuO . Indices l denote atomic monolayers

and are increasing with separation from the interface layer LaO.

Figure 5.9 Atomic displacements in the LaO/(EuO)₁₉ (001) superlattice with respect to the atomic “bulk” positions. The latter are determined by fixing the in-plane lattice constant and optimizing the interlayer distance, as described in the text. The vertical dashed line indicates the interface layer LaO.

Figure 5.10 Spin-dependent charge distribution across the LaO/(EuO)₁₉ (001) supercell. The notation for the atomic layers is the same as in Figure. 4.8. The dashed lines indicate the LaO interface layer.

List of Tables

Table 3.1 Number of electrons on Nb and Ti atoms per lateral unit cell area at two interfaces in the $\text{KNbO}_3/\text{ATiO}_3$ ($A = \text{Sr, Ba, Pb}$) heterostructures without polarizations, with parallel and with antiparallel polarizations in each constituent.

Table 4.1 Results from high-resolution x-ray diffraction measurements on the films at room temperature are given. The in-plane (a) and out-of-plane (c) lattice constants and lattice mismatch between the SrTiO_3 films and single crystal substrates on average of two orthogonal directions. The a- and c-lattice parameters of single-crystalline SrTiO_3 are 3.905 Å. All SrTiO_3 templates were fully coherent except STO/Si (12). (002), (101) of SrTiO_3 and cubic substrates, LSAT, Silicon (200) pseudo-cubic of (101) pseudo-cubic of orthorombic substrate, GdScO_3 and DyScO_3 , NdGdO_3 were observed to determine in-plane and out-of-plane lattice parameters.

Chapter 1 *Introduction*

1.1 Oxide heterostructures

The field of research related to oxide materials has been developing vigorously in the last few decades. There has been a significant experimental and theoretical effort to understand fundamental properties of oxide materials and to elucidate the origin of their complex behavior [1-3]. This effort is largely motivated by the fact that oxide materials provide more structural and functional choices than conventional semiconductors used in the electronic industry today. Oxide materials have enormous range of structure combinations from simplest binary monoxides like ZnO to much more complex oxides like $\text{Mo}_2\text{P}_4\text{O}_{15}$ containing a remarkable 441 crystallographically distinct atoms in its asymmetric unit [4]. Their transport properties span from insulating to semiconducting to metallic. Oxide materials possess a broad range of functional properties such as ferroelectricity, ferromagnetism, multiferroicity, and high-temperature superconductivity. For example, MgO, an insulator with simple rock-salt structure, is widely used as a barrier in magnetic tunnel junctions [5] which nowadays find applications in magnetic field sensors and magnetic random access memories (MRAM). Ferroelectric $\text{Pb}(\text{Zr}, \text{Ti})\text{O}_3$ plays an important role in ferroelectric random access memory (FeRAM) due to its large electric polarization at low Zr concentration. This material is also used in sensors and actuators [6], due to its excellent piezoelectric properties. $\text{La}_{1-x}\text{Sr}_x\text{MnO}_3$ exhibits different phases and depends on the concentration x . It

exhibits ferromagnetic or antiferromagnetic order with properties of conductivity ranging from metallic to insulating. Multiferroics BiFeO_3 simultaneously possesses ferroelectric and ferromagnetic properties which may be interesting for applications in multifunctional devices. Complex oxide $\text{YBa}_2\text{Cu}_3\text{O}_7$ exhibits a high-temperature superconductivity with the critical temperature above the boiling point (77 K) of liquid nitrogen [7]. All these properties are sensitive to stoichiometry, structural distortions, and chemistry [8, 9]. These factors provide many possible ways to engineering the functionalities of the oxide materials.

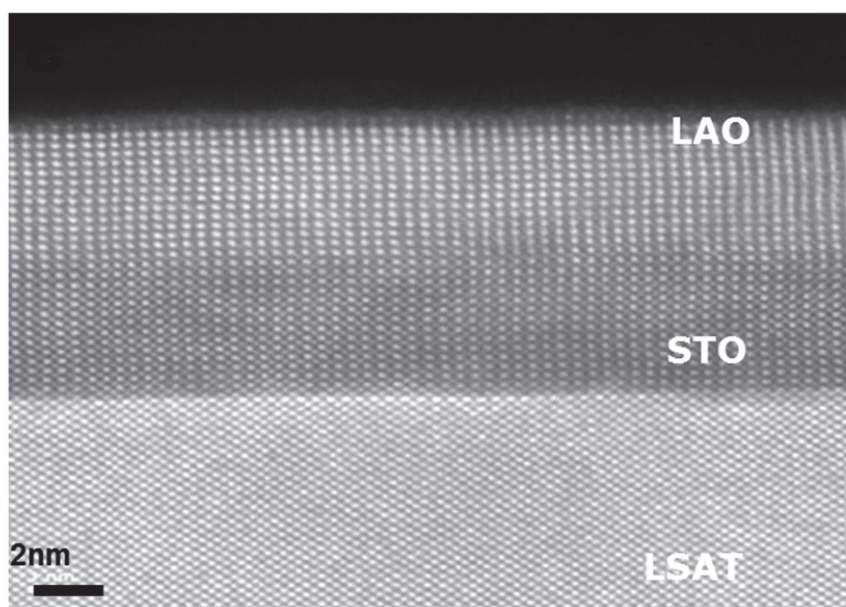


Figure 1.1 High-resolution TEM image of LaAlO_3 (LAO) / SrTiO_3 (STO) grown on $(\text{LaAlO}_3)_{0.3}-(\text{Sr}_2\text{AlTaO}_6)_{0.7}$ (LSAT). Intensity differences between separate LaAlO_3 and SrTiO_3 layers and the individual La and Sr atoms are clearly seen. [10]

Even more interesting physical phenomena and an even broader spectrum of functional properties occur if two or more complex oxides are combined with atomic-scale precision in a heterostructure to form a new nanoscale material. Recent advances in thin-film deposition and characterization techniques, such as pulsed laser deposition (PLD) [11], molecular beam epitaxy (MBE)[12] and the *in situ* monitoring techniques like reflection high-energy electron diffraction (RHEED) [13], have made the experimental realization of such oxide heterostructures possible. With these progresses, complex oxide heterostructures with atomically abrupt interfaces have been experimentally grown [10] [2, 14]. As an example the sharp interfaces between $\text{SrTiO}_3/(\text{LaAlO}_3)_{0.3}-(\text{Sr}_2\text{AlTaO}_6)_{0.7}$ (LSAT) and $\text{LaAlO}_3/\text{SrTiO}_3$ are shown in Figure 1.1.

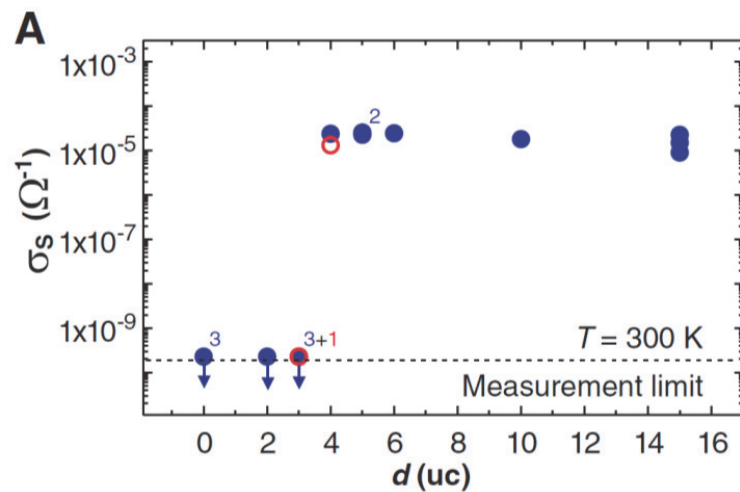
With the ability to create the oxide interfaces with atomic precision, many interesting and unexpected physical properties have been found [3, 9, 15]. For example, in $\text{Mg}_x\text{Zn}_{1-x}\text{O}/\text{ZnO}$ heterostructure grown on ScAlMgO_4 substrate, polarizations are developed in $\text{Mg}_x\text{Zn}_{1-x}\text{O}$ and ZnO layers. Due to the uncompensated polarizations at the interface, two dimensional electron gas (2DEG) and fractional quantum Hall effect are observed at the $\text{Mg}_x\text{Zn}_{1-x}\text{O}/\text{ZnO}$ interface [16]. Also extraordinary properties were discovered in all oxide superconductor/ferromagnet $\text{YBa}_2\text{Cu}_3\text{O}_7/\text{La}_{2/3}\text{Ca}_{1/3}\text{MnO}_3$ (YBCO/LCMO) heterostructures such as a very large magnetoresistance effect [17] and a coexistence of magnetism and superconductivity [18, 19]. Superconductivity and ferromagnetism normally do not coexist because of their competing long-range order. However, across the YBCO/LCMO interface charge is transferred from Mn to Cu atoms leading to a

covalent bond between Mn to Cu, and thus induces electronic reconstructions in the interfacial CuO_2 layer. As a result of the orbital rearrangement and strong hybridization, Cu ions in YBCO at interface are ferromagnetically ordered [19]. Another appealing phenomenon observed in oxide heterostructures is the localized ferromagnetic ordering at the interface between A-type antiferromagnetic LaMnO_3 and G-type antiferromagnetic SrMnO_3 [20] and possible magnetoelectric coupling [21]. When LaMnO_3 is deposited on SrMnO_3 (or vice versa), difference in the chemical potential at the interface causes a charge transfer which interacts with the spin and orbital degree of freedom and leads to the formation of two-dimensional ferromagnetic layers [20]. In addition, the interface between LaMnO_3 and SrMnO_3 is polar due to the broken symmetry. By combining three layers LaMnO_3 , SrMnO_3 and LaAlO_3 , the macroscopic inversion symmetry breaking could be retained and leads to an overall polar structure, and thus permits magnetoelectric coupling. The examples given above are just a few demonstrations of the new physics and novel functionalities that could arise from oxide interfaces.

One of the most exciting discoveries recently is the demonstration of a 2DEG at the interface between two perovskite oxide insulators LaAlO_3 and SrTiO_3 as we will discuss in detail in the next section. This discovery has attracted intense research activities both in experiment [22-28] and in theory [29-43].

1.2 2DEG at oxide interfaces

A two dimensional electron gas has been discovered at the LaO/TiO₂ interface between two wide-bandgap insulators SrTiO₃ and LaAlO₃ [44]. This electron gas presents an extremely high electron density up to $10^{14}/\text{cm}^2$ [45], and high mobility up to $10^4 \text{cm}^2/\text{Vs}$ at low temperatures [44]. This 2DEG is attractive for applications as all-oxide field-effect transistors [46, 47]. It was found that there is a critical thickness of LaAlO₃ with value of 4 unit cells above which the 2DEG emerges, as seen in Figure 1.2 [46]. By applying a gate voltage on LaAlO₃ with thickness of 3u.c just below the critical thickness, reversible control of insulator-metal transition was realized in LaAlO₃/SrTiO₃ heterostructure. There are also indications of ferromagnetic [48] and antiferromagnetic [49] ordering at the interfaces of LaAlO₃/SrTiO₃ heterostructures grown under high and low oxygen pressure respectively. Moreover, superconductivity is observed in LaAlO₃/SrTiO₃ at low temperature around a few hundred mK [50]. These interesting properties of this 2DEG make it promising for future generation electronics.



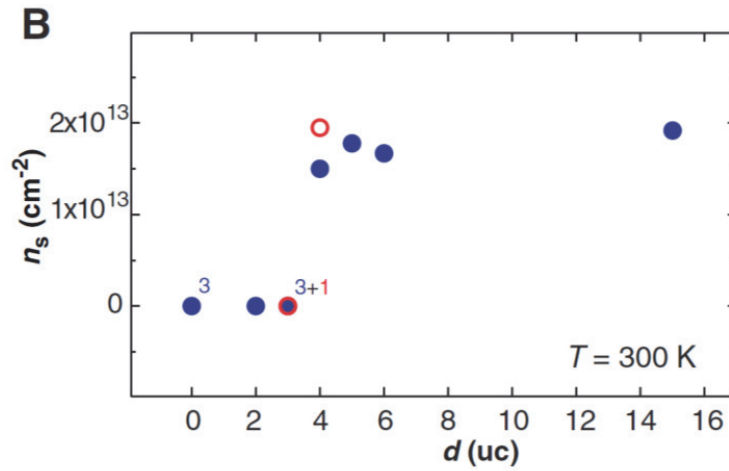


Figure 1.2 LaAlO₃ thickness dependence of the electronic properties of the LaAlO₃/SrTiO₃ interfaces. (A) Sheet conductance and (B) carrier density of the heterostructures plotted as a function of the number of LaAlO₃ unit cells. The data showed in blue and red are those of samples grown at 770-C and 815-C, respectively. The data were taken at 300 K [46].

SrTiO₃ and LaAlO₃ are all wide-bandgap insulators with $E_g = 3.2\text{eV}$ and 5.6eV respectively. Both of them have perovskite structure and have well matched lattice constants of 3.789 \AA and 3.905 \AA for LaAlO₃ and SrTiO₃ respectively. In these structures the conventional valence states for each element are La^{3+} , Al^{3+} , Sr^{2+} , Ti^{4+} and O^{2-} . Along the [001] direction, the perovskite can be considered consisting alternating planes of AO and BO₂. The major difference between LaAlO₃ and SrTiO₃ is that LaAlO₃ is formed of alternately charged atomic layers $(\text{LaO})^+$ and $(\text{AlO}_2)^-$ while SrTiO₃ is composed of neutral layers $(\text{SrO})^0$ and $(\text{TiO}_2)^0$ as shown in Figure 1.3.

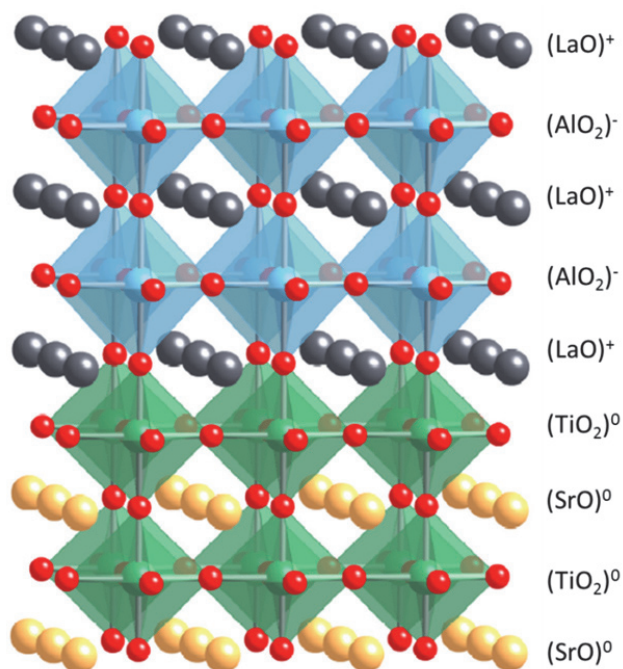


Figure 1.3 Illustration of $\text{LaAlO}_3/\text{SrTiO}_3$ heterostructure with $(\text{LaO})^+ / (\text{TiO}_2)^0$ interface showing the atomic arrangement and ionic charge for each layer.

When LaAlO_3 is deposited on top of SrTiO_3 in $[001]$ direction, there are two types of interface terminations: LaO/TiO_2 , as shown in Figure 1.3, and AlO_2/SrO called *n*-type and *p*-type interface respectively. It was found that a metallic phase can be formed at the LaO/TiO_2 terminated interface as long as the thickness of LaAlO_3 exceeds the critical thickness of 4 unit cells [44]. This metallic phase is confined within a couple of nanometers near the interface [51] and therefore can be regarded as a two dimensional electron gas. There are three proposed origins of the metallic state observed at the LaO/TiO_2 interface of $\text{SrTiO}_3/\text{LaAlO}_3$ heterostructure: polar catastrophe [52], oxygen

vacancies [23-25] and cation intermixing [53, 54].

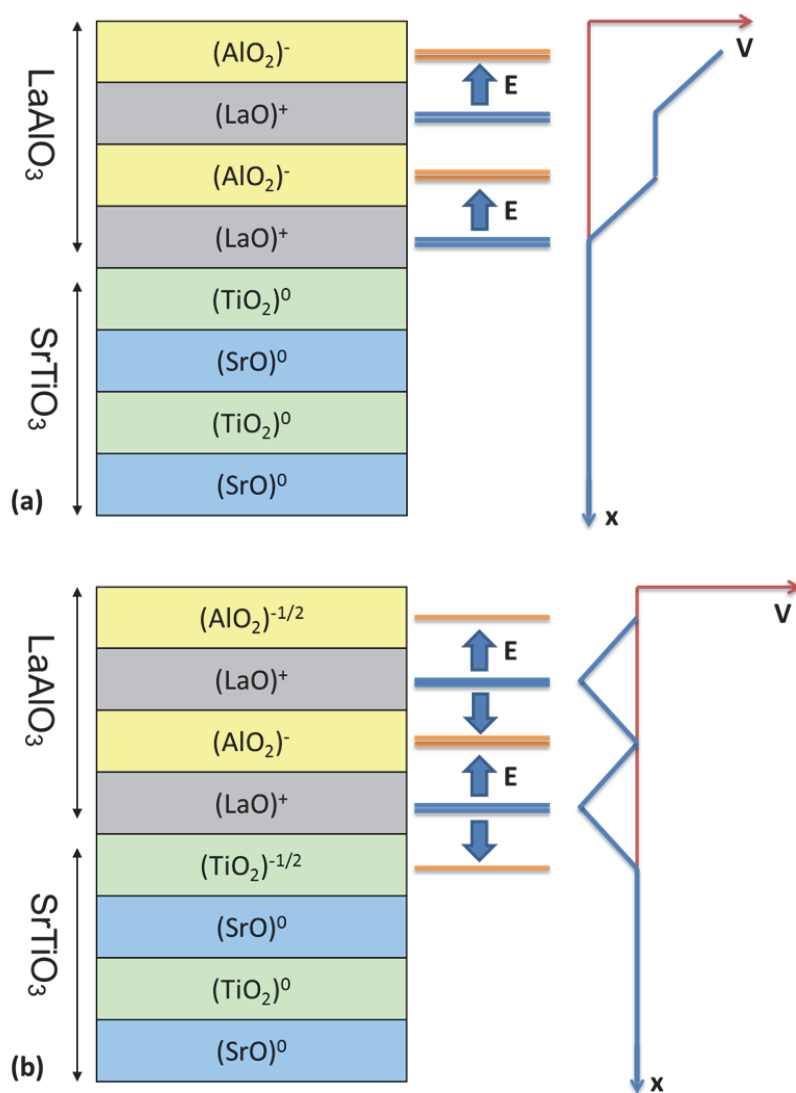


Figure 1.4 Schematic of the polar catastrophe at the n-type interface of LaAlO₃/SrTiO₃ heterostructure. (a). Before electronic reconstruction, alternating positive and negative atomic layers produce on average a constant electric field in LaAlO₃. The potential

increases with the thickness of LaAlO_3 . (b) $-0.5e$ is transferred to TiO_2 layers, alternating electric fields form at LaAlO_3 , and the overall effective electric field in LaAlO_3 is zero.

The polar catastrophe scenario is demonstrated in Figure 1.4. Polar discontinuity at the $(\text{LaO})^+ / (\text{TiO}_2)^0$ interface occurs as the consequence of the alternating positive and negative charged planes of LaAlO_3 on top of neutral planes of SrTiO_3 . This polar discontinuity creates an internal electric field in LaAlO_3 and thus an increase electric potential across the LaAlO_3 layers. From the electrostatic point of view, as the thickness of LaAlO_3 increases, the potential also increases and the system becomes unstable. In semiconductor heterointerfaces such a polar discontinuity is well-known, and which often causes atomic reconstruction at the interface to avoid the diverging electrostatic potential [55, 56]. In contrast, transition metals in perovskite oxide can be mixed-valence and make electronic reconstruction possible, which is more favorable in energy than atomic reconstruction [53]. Half an electron per two-dimensional unit cell is transferred through the interface from LaAlO_3 to SrTiO_3 causing the interfacial titanium ion in SrTiO_3 to be in the mixed valence state ($\text{Ti}^{+3.5}$). This half an electron per unit cell at the $(\text{LaO})^+ / (\text{TiO}_2)^{-0.5}$ interface forms the 2DEG.

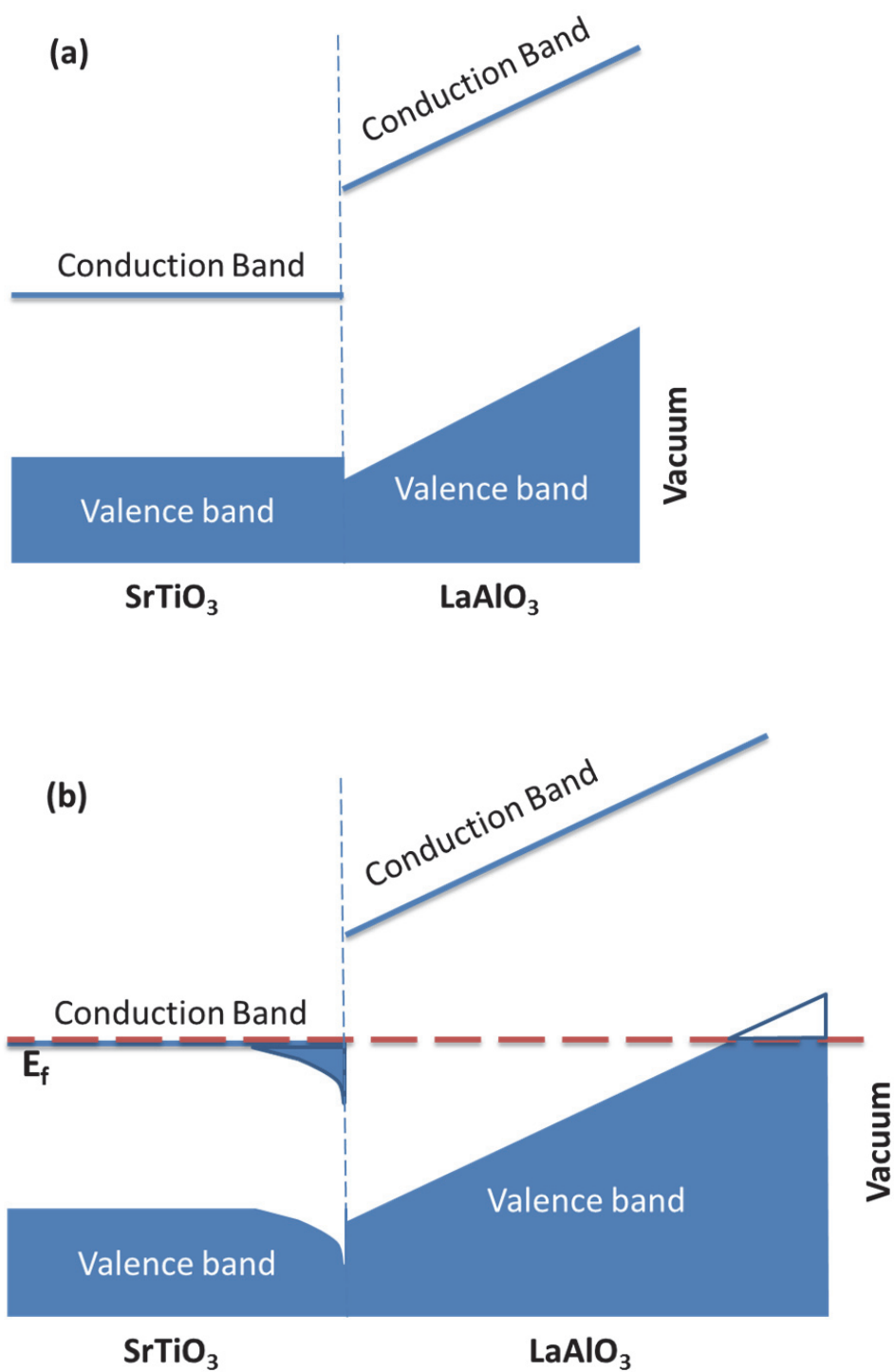


Figure 1.5 Schematic band diagrams for the SrTiO₃/LaAlO₃ heterostructures with

thickness smaller and larger than the critical thickness. (a) When the LaAlO_3 thickness is smaller than the critical thickness, the valence band maximum (VBM) of LaAlO_3 on the surface lies below the conduction band minimum (CBM) of SrTiO_3 at the interface and no charge is transferred. (b) When the LaAlO_3 thickness exceeds the critical thickness, VBM of LaAlO_3 on the surface lies above the CBM of SrTiO_3 at the interface and charge is transferred from the surface layer of LaAlO_3 , i.e. AlO_2 to the interface layer of SrTiO_3 , i.e. TiO_2 . The red dashed line indicates the position of the Fermi energy. Ref. [52]

This scenario has been confirmed more rigorously by first-principles calculations [38, 42, 52] and can be understood from a simple band diagram, as illustrated in Figure 1.5. Due to the polar nature of LaAlO_3 resulting in the intrinsic electric field, the macroscopically averaged local potential increases across the LaAlO_3 layer. When the thickness of LaAlO_3 is smaller than the critical thickness the potential change is not large enough to make the valence band maximum (VBM) of LaAlO_3 on the surface to exceed the SrTiO_3 band gap and therefore there is no charge transfer to the $\text{LaAlO}_3/\text{SrTiO}_3$ interface. However, when the LaAlO_3 thickness is larger than the critical thickness, the VBM of LaAlO_3 at the surface exceeds the conduction band minimum (CBM) of SrTiO_3 at the interface, and charge is transferred to the interface. Due to the insulating nature of LaAlO_3 and SrTiO_3 layers away from the interface, the conducting electrons are quantum confined at the interface [37].

There are a number of experimental results suggesting the electronic reconstruction is the primary mechanism responsible for the 2DEG formation at oxide interfaces. In particular, the built-in electric field in LaAlO_3 was recently experimentally observed [57]. In addition, 2DEG was also found at the interfaces in other heterostructures, such as $\text{LaVO}_3/\text{SrTiO}_3$ [22], consistent with electronic reconstruction mechanism. In some systems, however, it was argued the polar discontinuity may also be eliminated by the competition between the electronic and atomic reconstruction mechanisms [56, 58].

The properties of a 2DEG strongly depend on the thin film grow conditions, which influence the oxygen vacancy concentration. It is well known that oxygen vacancy rich SrTiO_3 is metallic [59]. Depending on the oxygen pressure during the film growth process, the carrier mobility and carrier concentration at the $\text{SrTiO}_3/\text{LaAlO}_3$ interface can be different by orders of magnitude [23]. The maximum carrier density at the interface can be as high as $10^{17}/\text{cm}^2$ which is much larger than the maximum theoretical value $3.5 \times 10^{14}/\text{cm}^2$. Apparently oxygen vacancies are responsible for the metallic behavior. Several experiments have demonstrated that during the growth oxygen vacancies appear in the SrTiO_3 substrate which makes it conducting [23-25]. However, if heterostructures are grown at high oxygen pressure, oxygen vacancies may be avoided and the dominant mechanism of the conducting interface in this situation is the electronic reconstruction [53].

The cation intermixing may also be the reason for the 2DEG formed at the $\text{LaAlO}_3/\text{SrTiO}_3$ interface. It follows from the fact that La^+ doped SrTiO_3 , i.e., $\text{Sr}_{1-x}\text{La}_x\text{TiO}_3$

$x\text{La}_x\text{TiO}_3$ with $0.1 < x < 0.95$, is metallic [60]. Experimentally La and Sr intermixing at interface of SrTiO_3 and LaAlO_3 has been observed, which leads to the formation of a thin layer of $\text{Sr}_{1-x}\text{La}_x\text{TiO}_3$ at interface, and thus to a conducting phase [53, 54]. Cation intermixing was also considered theoretically as a possible mechanism of the conducting interface [54]. However, fabrication of stoichiometric interfaces with a precise control of oxide constituents at the interface eliminates this mechanism of the 2DEG formation.

In contrast, no metallic phase is found at p-type AlO_2/SrO interfaces. This is because there are no proper multiple valence states (e.g. $\text{Ti}^{+4.5}$ and O^-) and thus it is highly unlikely to accommodate a hole [45, 53]. Oxygen vacancy also plays an important role in this insulating p-type interface [53].

1.3 Motivation and organization of this dissertation

As pointed out by a recent review paper published in Science [15], incorporation of functional oxides into electronic circuits or their use in other applications requires mastering their interfaces. This implies understanding, predicting and tailoring the physical properties of the interfaces between complex oxide materials. Having these challenges in mind, in this thesis by performing first-principles calculations based on density functional theory, we investigate the effect of ferroelectric polarization and effect of epitaxial strain on 2DEG formed at the oxide interfaces, and propose a method to realize a spin-polarized 2DEG.

In chapter 2, we review the theoretical methods based on density functional theory

that are used in this dissertation. We first introduce the Schrödinger equation to describe a many-body interacting electron system and explain the difficulties of solving this equation in a general form. Then we describe the Hohenberg-Kohn theorems and the corresponding Kohn-Sham equation. In the next two sections, we briefly introduce the local density approximation (LDA), the generalized gradient approximation (GGA) and the LDA+U approximation for the exchange and correlation effects of interacting electrons. Then a projector augmented wave (PAW) method is introduced to approximate the ionic potential. In the last section of this chapter, we introduce the Vienna Ab-initio Simulation Package (VASP) in which our DFT calculations are implemented.

In chapter 3, the properties of 2DEG in the presence of ferroelectric materials are investigated and the ability to manipulate 2DEG by spontaneous polarization is demonstrated. We first give an introduction to some basic concepts and properties of perovskite ferroelectrics. Then, a method to control the properties of the 2DEG by external field known from literature is briefly reviewed. Further, we provide details of the electronic and atomic structures of the $\text{KNbO}_3/\text{ATiO}_3$ interfaces, which are considered to demonstrate the mechanisms responsible for the modulation of the 2DEG properties by ferroelectric polarization. The central part of this chapter is the prediction of the influence of ferroelectric polarizations on the 2DEG formed at three different systems: $\text{KNbO}_3/\text{ATiO}_3$ ($A = \text{Sr}, \text{Ba}$ and Pb). Finally, we discuss a possibility of the controllable metal-insulator transition at the interface driven by polarization reversal.

In chapter 4, the epitaxial strain effect on 2DEG at the $\text{LaAlO}_3/\text{SrTiO}_3$ interface is

investigated. Strain could change the crystal field, bonding properties and electron interactions and thus have strong impact on properties of materials. We first introduce the experimental results for the $\text{LaAlO}_3/\text{SrTiO}_3$ systems grown on different substrates, such as NdGaO_3 , $(\text{LaAlO}_3)_{0.3}-(\text{Sr}_2\text{AlTaO}_6)_{0.7}$, DyScO_3 and GdScO_3 , which provides epitaxial strain ranging from -1.2% to 1.59%. Then we discuss this phenomenon theoretically based on our first-principles calculations. We show that the critical thickness for 2DEG formation increases with the compressive strain. We demonstrate that the increased critical thickness under compressive strain can be explained by the electric polarization formed in SrTiO_3 due to the strain.

In chapter 5, we explore possibilities to create a spin-polarized 2DEG at EuO/LaO interfaces. First, spin-polarized 2DEG systems known from literature are introduced. Bulk properties of ferroelectric insulator EuO are briefly described. Then we consider two systems $\text{LaAlO}_3/\text{EuO}$ and $\text{EuO}/\text{LaO}/\text{EuO}$. We demonstrate that in both systems 2DEG is formed due to extra charge at LaO^+ interface layer. The 2DEG becomes spin-polarized as the result of the electron population of the Eu-5d state in the EuO conduction band which is exchange split due to the hybridization with Eu-5f states.

Chapter 2 *Theoretical methods*

2.1 Many-body Schrödinger equation

Properties of materials are governed by the interactions between the constituting electrons and nuclei. From the point of view of quantum mechanics, these properties are determined by the many-body Schrödinger equation:

$$\hat{H}\psi(\{\mathbf{R}_I, \mathbf{r}_i\}) = E\psi(\{\mathbf{R}_I, \mathbf{r}_i\}) , \quad (2.1)$$

where the Hamiltonian is given by

$$\hat{H} = -\sum_I \frac{\hbar^2}{2M_I} \nabla_{\mathbf{R}_I}^2 - \frac{\hbar^2}{2m_e} \sum_i \nabla_{\mathbf{r}_i}^2 - \sum_{i,I} \frac{Z_I e^2}{|\mathbf{r}_i - \mathbf{R}_I|} + \frac{1}{2} \sum_{i \neq j} \frac{e^2}{|\mathbf{r}_i - \mathbf{r}_j|} + \frac{1}{2} \sum_{I \neq J} \frac{e^2}{|\mathbf{R}_I - \mathbf{R}_J|} . \quad (2.2)$$

The first and second terms here are the kinetic energy of ions and electrons respectively. The third term is the ion-electron potential energy. The fourth and fifth terms are electron-electron and ion-ion potential energy. As the masses of ions are very large and the ions move very slowly compared to electrons, according to the Born-Oppenheimer approximation, the system can be excellently described by the motion of electrons alone and the kinetic energy of ions can be ignored in the Hamiltonian. Since we are interested in the electronic structures, the ion-ion interaction term is irrelevant and can be dropped. Thus, the Hamiltonian can now be simplified as

$$\hat{H} = \hat{T} + \hat{V}_{ion} + \hat{V}_{ee} , \quad (2.3)$$

where

$$\hat{T} = -\sum_i \nabla_{\mathbf{r}_i}^2 \quad (2.4)$$

$$\hat{V}_{ion} = -\sum_{i,I} \frac{Z_I}{|\mathbf{r}_i - \mathbf{R}_I|} \quad (2.5)$$

$$\hat{V}_{ee} = \frac{1}{2} \sum_{i \neq j} \frac{1}{|\mathbf{r}_i - \mathbf{r}_j|} , \quad (2.6)$$

and we used the atomic units to simplify the description.

The major difficulty in solving Eq. (2.1) is that the electron-electron interaction energy \hat{V}_{ee} (2.6) could not be simply expressed as a sum of isolated single-particle energies. Consequently, the correlation interaction of electrons, $\psi(\{\mathbf{r}_i\})$ can not simply written as a production of isolated electron wavefunctions. These facts make solution of Eq. (2.1) very difficult and even not possible at present time for realistic systems. Approaches such as the Hartree-Fock approximation and density functional theory to replacing the many-body particle equations by a non-interacting single particle equation have been proposed to go around these difficulties. Density functional theory excels the Hartree-Fock method in the sense that it only deals with the one simple function, i.e. density of electron $n(\mathbf{r})$, and includes both the exchange and correlation interaction while the Hartree-Fock method only includes the exchange effect. Density functional theory had an enormous impact on the electronic structure calculations and is the most widely used method today. The following three sections are devoted to the essential ideas behind density functional theory including the Kohn-Sham equation and the approximation for exchange-correlation potential and the approximation of the electron-ion potential.

2.2 Kohn-Sham equation

The density functional theory is based on two theorems proposed by Hohenberg and Kohn [61]. The first theorem states the ground state properties of many-body interacting electron system are uniquely defined by the ground state electron density $n_0(\mathbf{r})$. The second theorem states that the expectation value of energy E is a functional of electron density, i.e. $E = E[n(\mathbf{r})]$, and this functional reaches its minimum at the ground state density $n_0(\mathbf{r})$, i.e. $E_{\min} = E[n_0(\mathbf{r})]$. The energy functional is naturally divided into two contributions: one depends purely on electronic motions and another depends on ionic potentials, which can be written as

$$E[n(\mathbf{r})] = F[n(\mathbf{r})] + \int V_{ion}(\mathbf{r})n(\mathbf{r})d\mathbf{r} \quad (2.7)$$

with

$$V_{ion}(\mathbf{r}) = -\sum_I \frac{Z_I}{|\mathbf{r} - \mathbf{R}_I|}. \quad (2.8)$$

As proposed by Kohn and Sham [62], the many-body electron system can be replaced by an auxiliary system of non-interacting particles as long as the ground state density of the auxiliary system is identical to the ground state density of many-body electrons. Assuming the single particle orbital is $\phi_i(\mathbf{r})$, the density of the auxiliary system is then expressed as

$$n(\mathbf{r}) = \sum_i |\phi_i(\mathbf{r})|^2. \quad (2.9)$$

By evaluating Eq. (2.3) the functional $F[n(\mathbf{r})]$ in Eq. (2.7) takes the form

$$F[n(\mathbf{r})] = T[n(\mathbf{r})] + \frac{1}{2} \iint \frac{n(\mathbf{r})n(\mathbf{r}')}{|\mathbf{r}-\mathbf{r}'|} d\mathbf{r}d\mathbf{r}' + E_{xc}[n(\mathbf{r})] \quad (2.10)$$

where the first term on the right hand side

$$T[n(\mathbf{r})] = -\sum_i \langle \phi_i(\mathbf{r}) | \nabla_{\mathbf{r}}^2 | \phi_i(\mathbf{r}) \rangle \quad (2.11)$$

is the kinetic energy, and the second term is the Hartree energy due to the Coulomb repulsion between particles. The third term is defined to include all the many-body effects of exchange and correlation and is not known explicitly yet as a function of $n(\mathbf{r})$.

The approximation form of this term will be discussed in the next section. Performing variation calculation to Eq. (2.7) and taking account the restriction condition $\int \delta n(\mathbf{r}) = \int \delta \phi_i(\mathbf{r}) \phi_i^*(\mathbf{r}) d\mathbf{r} = 0$ through a Lagrange multiplier ε_i , we obtain the Kohn-Sham equations:

$$\left[-\nabla_{\mathbf{r}}^2 + V_{eff}(\mathbf{r}, n(\mathbf{r})) \right] \phi_i(\mathbf{r}) = \varepsilon_i \phi_i(\mathbf{r}) \quad (2.12)$$

with

$$V_{eff}(\mathbf{r}, n(\mathbf{r})) = V_{ion}(\mathbf{r}) + V_{Hartree}(\mathbf{r}, n(\mathbf{r})) + V_{xc}(\mathbf{r}, n(\mathbf{r})) , \quad (2.13)$$

where

$$V_{Hartree}(\mathbf{r}, n(\mathbf{r})) = \int \frac{n(\mathbf{r}')}{|\mathbf{r}-\mathbf{r}'|} d\mathbf{r}' \quad (2.14)$$

$$V_{xc}(\mathbf{r}, n(\mathbf{r})) = \frac{\delta E_{xc}[n(\mathbf{r})]}{\delta n(\mathbf{r})} \quad (2.15)$$

are Hartree and exchange-correlation potential respectively. The single particle wavefunction $\phi_i(\mathbf{r})$ is called the Kohn-Sham orbital and is not the true electron wavefunction. However it provides the correct density as in real many-body electron

system. The eigenvalues ε_i are not the true excitation energy of the electron since they are introduced just as Lagrange multipliers. The determination of the excitation energy is normally done by the Quantum Monte Carlo [63] and many-body perturbation theory calculation [64] with the assistance of the eigenstates obtained from Kohn-Sham equation. All the properties that can be derived from the ground state energy are given correctly. For a collinear spin-polarized system, spin up and spin down particles are treated separately. To extend to this case, all the functions in Kohn-Sham equations should be written as function of both position \mathbf{r} and spin direction σ i.e. $\phi_i(\mathbf{r}, \sigma)$ and $V_{eff}(\mathbf{r}, \sigma)$.

2.3 LDA and GGA approximation

Since the electron density function in the effective potential of the Kohn-Sham equation can only be obtained after Eq. (2.12) is solved for example using an iteration algorithm. The major issue in the Kohn-Sham approach is how to obtain the expression of the exchange-correlation potential V_{xc} or equivalently energy $E_{xc}[n(\mathbf{r})]$. Considering that the effective potential V_{eff} in Eq. (2.13) includes the ionic potential $V_{ion}(\mathbf{r})$ and long range Coulomb potential $V_{Hartree}$, the remaining exchange-correlation potential V_{xc} should be reasonably approximated by a local functional of density. The exchange-correlation energy

$$E_{xc}[n(\mathbf{r})] = \int n(\mathbf{r})\varepsilon_{xc}(\mathbf{r})d\mathbf{r} \quad (2.16)$$

is an integral of energy density over the whole space

Within this local density approximation (LDA), the exchange-correlation energy density $\varepsilon_{xc}(\mathbf{r})$ at each space point \mathbf{r} is assumed to be the same as energy density $\varepsilon_{xc}^{\text{hom}}(\mathbf{r})$ in the homogeneous electron gas with the same particle density $n(\mathbf{r})$. In the homogeneous system, $\varepsilon_{xc}^{\text{hom}}$ is purely a function of the electron density and can be divided to the exchange and correlation part separately i.e. $\varepsilon_{xc}^{\text{hom}} = \varepsilon_x^{\text{hom}}(n) + \varepsilon_c^{\text{hom}}(n)$. Therefore the exchange-correlation energy in the LDA approximation is

$$\begin{aligned} E_{xc}^{LDA}[n(\mathbf{r})] &= \int n(\mathbf{r}) \varepsilon_{xc}^{\text{hom}}(n(\mathbf{r})) d\mathbf{r} \\ &= \int n(\mathbf{r}) \left[\varepsilon_x^{\text{hom}}(n(\mathbf{r})) + \varepsilon_c^{\text{hom}}(n(\mathbf{r})) \right] d\mathbf{r} \end{aligned} \quad (2.17)$$

The exchange energy $\varepsilon_x^{\text{hom}}(n)$ of a homogeneous electron gas is represented by a simple analytic form $\varepsilon_x^{\text{hom}}(n) = -\frac{3}{4} \left(\frac{3n}{\pi} \right)^{1/3}$ [65], while the correlation energy $\varepsilon_c^{\text{hom}}(n)$ can be parameterized with great accuracy using the results from Quantum Monte Carlo calculation [66]. As soon as the exchange-correlation energy $E_{xc}^{LDA}[n(\mathbf{r})]$ is known, the exchange-correlation potential in the Kohn-Sham equation can be easily obtained from the variation of $E_{xc}^{LDA}[n(\mathbf{r})]$:

$$\delta E_{xc}^{LDA}[n(\mathbf{r})] = \int \left[\varepsilon_{xc}^{\text{hom}}(n(\mathbf{r})) + n \frac{\partial \varepsilon_{xc}^{\text{hom}}(n(\mathbf{r}))}{\partial n} \right] \delta n(\mathbf{r}) d\mathbf{r}. \quad (2.18)$$

Thus by definition

$$V_{xc}^{LDA}[n(\mathbf{r})] = \varepsilon_{xc}^{\text{hom}} + n \frac{\partial \varepsilon_{xc}^{\text{hom}}}{\partial n}. \quad (2.19)$$

This LDA works very well even in case of very inhomogeneous system, although strictly speaking both exchange and correlation in this case should be non-local [67].

When the electron spin is taken into account, the approximation is extended to local spin density approximation (LSDA) in which the exchange-correlation energy and potential are the functional of both spin-up and spin-down electron densities. And the Eq. (2.17) is modified as

$$E_{xc}^{LSDA}[n(\mathbf{r})] = \int n(\mathbf{r}) \varepsilon_{xc}^{\text{hom}}(n^{\uparrow}(\mathbf{r}), n^{\downarrow}(\mathbf{r})) d\mathbf{r} \quad (2.20)$$

Generalized-gradient approximations (GGA) [68-70] extend the LDA assuming that E_{xc} not only depends on the density $n(\mathbf{r})$, but also on the magnitude of its gradients $|\nabla n(\mathbf{r})|$. Thus the exchange-correlation energy is written as

$$\begin{aligned} E_{xc}^{GGA}[n(\mathbf{r})] &= \int n(\mathbf{r}) \varepsilon_{xc}^{\text{hom}}(n(\mathbf{r}), |\nabla n(\mathbf{r})|) d\mathbf{r} \\ &= \int n(\mathbf{r}) \varepsilon_x^{\text{hom}}(n(\mathbf{r})) F_{xc}(n(\mathbf{r}), |\nabla n(\mathbf{r})|) d\mathbf{r} \end{aligned} \quad (2.21)$$

where the gradient of density is included in dimensionless functional $F_{xc}(n(\mathbf{r}), |\nabla n(\mathbf{r})|)$. As $\varepsilon_x^{\text{hom}}$ is already known, the most important step for evaluating E_{xc}^{GGA} is to obtain both the exchange F_x and correlation F_c part of F_{xc} . By expanding both of them, various forms of F_{xc} have been proposed such as Perdew and Wang (PW91) [69] and Perdew, Burke and Enzerhof (PBE) [70]. Similar to LDA once E_{xc}^{GGA} is obtained; the exchange-correlation potential can be derived via variational method:

$$\delta E_{xc}^{GGA}[n(\mathbf{r})] = \int \left[\varepsilon_{xc}^{\text{hom}}(n(\mathbf{r})) + n \frac{\partial \varepsilon_{xc}^{\text{hom}}(n, \nabla n)}{\partial n} + n \frac{\partial \varepsilon_{xc}^{\text{hom}}(n, \nabla n)}{\partial \nabla n} \nabla \right] \delta n(\mathbf{r}) d\mathbf{r}, \quad (2.22)$$

$$V_{xc}^{GGA}[n(\mathbf{r})] = \varepsilon_{xc}^{\text{hom}}(n(\mathbf{r})) + n \frac{\partial \varepsilon_{xc}^{\text{hom}}(n, \nabla n)}{\partial n} - \nabla \left(n \frac{\partial \varepsilon_{xc}^{\text{hom}}(n, \nabla n)}{\partial \nabla n} \right). \quad (2.23)$$

GGA provides better agreement with experiment over LDAs in many cases especially in predicting the binding energy for many finite systems like molecules and

surfaces, etc.

2.4 LDA+U approximation

Despite the success of LDA and GGA, both of them have problems to describe systems with localized (strongly correlated) d and f electrons such as transition metal compound and rare earth elements and compound. Because $V_{xc} = \frac{\delta E_{xc}[n]}{\delta n}$ obtained from LDA or GGA is like a mean-field solution. The LDA or GGA functional tend to over-delocalize the electrons and the on-site Coulomb repulsion is not well taken into account for localized orbitals. To improve the description, an additional orbital dependent interactions of the same form as the ‘U’ interaction in Hubbard models can be introduced [71]. In this method known as the ‘LDA+U’ and ‘GGA+U’, the added term shifts the energy of localized orbitals relative to other orbitals and thus corrects errors usually large in LDA and GGA calculations [67].

More specifically, within atomic spheres where the atomic characteristics of the electronic state largely survived, wave function is expanded in a localized orthonormal basis $|inlm\sigma\rangle$ (i denotes the site, n is the magnetic number, l is the orbital quantum number, m is the magnetic quantum number, σ is the spin index). The partly filled localized electrons are assumed to be in nl shell. The density matrix for these electrons is defined as [72]:

$$n_{mm'}^{\sigma} = -\frac{1}{\pi} \int^{E_F} \text{Im} G_{ilm,ilm'}^{\sigma}(E) dE, \quad (2.24)$$

where $G_{ilm,ilm'}^\sigma(E)$ are the elements of the green-function matrix in the localized representation.

The generalized LDA+U functional containing three terms: the standard LDA functional E_{LDA} , the Hubbard-like term E_{Hub} including effective on-site interaction, and the ‘double counting’ term E_{dc} . Since the Hubbard-like term is added explicitly, the energy contribution of these orbitals included in LDA functional should be removed to avoid twice counting by subtracting E_{dc} . In terms of density matrix, LDA+U energy functional is

$$E_{LDA+U} = E_{LDA}[\rho^\sigma(\mathbf{r})] + E_{Hub}[\{n^\sigma\}] - E_{dc}[\{n^\sigma\}], \quad (2.25)$$

where $\rho^\sigma(\mathbf{r})$ is the charge density for spin σ electrons. In the fully rotational invariant form [73] the Hubbard term is given as

$$E_{Hub}[\{n^\sigma\}] = \frac{1}{2} \sum_{\{m\}, \sigma} \left\{ \langle m, m'' | V_{ee} | m', m''' \rangle n_{mm'}^\sigma n_{m''m'''}^{-\sigma} + \left(\langle m, m'' | V_{ee} | m', m''' \rangle - \langle m, m'' | V_{ee} | m''', m' \rangle \right) n_{mm'}^\sigma n_{m''m'''}^\sigma \right\}, \quad (2.26)$$

where V_{ee} is the screened Coulomb interaction among correlation electrons. From the expansion of $\frac{1}{|\mathbf{r}-\mathbf{r}'|}$ in spherical harmonics, the matrix elements are obtained as:

$$\langle m, m'' | V_{ee} | m', m''' \rangle = \sum_h a_k(m, m', m'', m''') F^k, \quad (2.27)$$

where

$$a_k(m, m', m'', m''') = \frac{4\pi}{2k+1} \sum_{q=-k}^k \langle lm | Y_{kq} | lm' \rangle \langle lm'' | Y_{kq}^* | lm''' \rangle. \quad (2.28)$$

F^k is the effective Slater integral which are specified in terms of the effective on-site Coulomb and exchange parameter U and J [73]. The double counting term is given as

$$E_{dc}[\{n^\sigma\}] = \frac{U}{2}n(n-1) - \sum_{\sigma} \frac{J}{2}n^\sigma(n^\sigma - 1), \quad (2.29)$$

where

$$n^\sigma = \sum_m n_{mm}^\sigma, \quad (2.30)$$

$$n = \sum_{\sigma} n^\sigma. \quad (2.31)$$

The Kohn-Sham Hamiltonian \hat{H}_{LDA+U} including on-site Coulomb interaction is finally obtained by minimizing the LDA+U energy functional $E_{LDA+U}(\rho^\sigma(\mathbf{r}), \{n^\sigma\})$ with respect to $\rho^\sigma(\mathbf{r})$ and $\{n^\sigma\}$ as:

$$\hat{H}_{LDA+U} = \hat{H}_{LDA} + \sum_{mm'} |inlm\sigma\rangle V_{mm}^\sigma \langle inlm'\sigma|, \quad (2.32)$$

where

$$\begin{aligned} V_{mm'}^\sigma = & \sum_{m''m'''} \{ \langle m, m'' | V_{ee} | m', m''' \rangle n_{m''m'''}^{-\sigma} \\ & + (\langle m, m'' | V_{ee} | m', m''' \rangle - \langle m, m'' | V_{ee} | m''', m' \rangle) n_{m''m'''}^\sigma \} \\ & - U(n - \frac{1}{2}) + J(n^\sigma - \frac{1}{2}) \end{aligned} \quad (2.33)$$

2.5 Plane wave pseudopotential methods

A simple and convenient way to solve the Kohn-Sham Schrödinger equation is the plane wave method [74]. From the Bloch theorem, the wavefunction $\psi_{n,k}(\mathbf{r}) = e^{i\mathbf{k}\cdot\mathbf{r}}u(\mathbf{r})$ of an electron in the effective periodic potential V_{eff} can be written as a cell-periodic function $u(\mathbf{r})$ modulated by a plane wave $e^{i\mathbf{k}\cdot\mathbf{r}}$. Expanding the periodic function $u(\mathbf{r})$ by plane waves $e^{i\mathbf{G}\cdot\mathbf{r}}$ with wave vectors \mathbf{G} in the reciprocal space, the electron wavefunction can be expressed as a combination of plane wave i.e.

$$\psi_k(r) = \sum_{\mathbf{G}} c_{\mathbf{k}+\mathbf{G}} e^{i(\mathbf{k}+\mathbf{G})\cdot\mathbf{r}}, \quad (2.34)$$

where $c_{n,\mathbf{k}+\mathbf{G}}$ are determined by solving the matrix of Kohn-Sham equation in reciprocal space

$$\sum_{\mathbf{G}'} \left[|\mathbf{k} + \mathbf{G}|^2 \delta_{\mathbf{G}\mathbf{G}'} + V_{eff}(\mathbf{G} - \mathbf{G}') \right] c_{\mathbf{k}+\mathbf{G}'} = \varepsilon_i c_{\mathbf{k}+\mathbf{G}} \quad (2.35)$$

upon substituting Eq. (2.34) into the equation. In principle, infinite number of reciprocal vectors \mathbf{G} is required to expand the wavefunction. However, $c_{n,\mathbf{k}+\mathbf{G}}$ with smaller kinetic energy $|\mathbf{k} + \mathbf{G}|^2$ are more important than those with larger kinetic energy. Within certain energy accuracy, finite plane wave basis set can be obtained by introducing a cutoff energy E_{cut} such that $\frac{1}{2}|\mathbf{k} + \mathbf{G}|^2 \leq E_{cut}$.

Although the accuracy of the expansion can always be reached by increasing E_{cut} , this direct plane wave method is not practical since the number of plane wave is always extremely large in order to describe the tight bounded electron core state and electron valence state with rapid oscillation near the nucleus. Considering the facts that the core electrons have little interaction with neighbors and physical properties of material are mostly influenced by valence electrons, a ‘pseudo’ ionic potential can be constructed such that a pseudo-wavefunction is generated correspondingly which pertains the identical scattering properties of the ion and core electron for valence electron and is identical to the valence wavefunction outside a critical radius (core radius). The pseudo-wavefunction can be smooth in the core region by choosing proper pseudopotential such

that pseudo-wavefunction is orthogonal to the core states which have many nodes. By replacing the true ionic potential with pseudopotential, the core electron states disappear and character of rapid oscillation of valence electron wave-function in the core region is replaced by smooth behavior of the pseudo-wavefunction [75]. Therefore, the replacing total energy without core-electrons energy is smaller than that in the true system, and the required plane wave set is much smaller due to the smooth nature of pseudo-wavefunction.

There are many pseudopotential approaches such as norm-conserving pseudopotential (NCPP) [76], ultrasoft pseudopotential (USPP) [77] and projector augmented wave (PAW) [78]. The ordinary pseudopotential method like NCPP is either very large or complicated for the first-row elements and system with d or f electrons in order to taking into account the semicore states of them, and is not an economical way to calculate these systems. But both USPP and PAW method allow these systems to be handled in an affordable effect. In this dissertation all the DFT calculations are performed using the PAW method. This all-electron pseudopotential method divides the wave function into an auxiliary smooth valence function $\tilde{\psi}_n$ which can be represented in a plane wave expansion and an auxiliary localized partial-wave function $\tilde{\phi}_i$ which keep all the information of the core states [78]. Mathematically only $\tilde{\psi}_n$ are taken into account in Schrödinger equation calculation and $\tilde{\phi}_i$ are taken into account within a

pseudopotential. PAW method starts with a transformation operator \hat{T} which maps the auxiliary wave function $\tilde{\psi}_n$ to the real wave function ψ_n :

$$|\psi_n(\mathbf{r})\rangle = \hat{T}|\tilde{\psi}_n\rangle. \quad (2.36)$$

To look at the atomic centered contribution to the this transformation, the transformation operator \hat{T} is expressed as

$$\hat{T} = 1 + \sum_{\mathbf{R}_i} \hat{T}_{\mathbf{R}_i}, \quad (2.37)$$

where $\hat{T}_{\mathbf{R}_i}$ acts within some augmentation region enclosing atom at site \mathbf{R}_i and is determined by the transformation

$$|\phi_i(\mathbf{r})\rangle = \hat{T}|\tilde{\phi}_i\rangle, \quad (2.38)$$

where target partial wave ϕ_i are the solution of radial Schrödinger equation for isolated atoms, and auxiliary partial-wave function $\tilde{\phi}_i$ are generated to be orthogonal to the core state and identical to target partial wave ϕ_i outside the augmentation radius. Using Eqs (2.37) and (2.38) and introducing a projector function $\langle\tilde{p}_i|$ which obeys the conditions:

$$\langle\tilde{p}_i|\tilde{\phi}_j\rangle = \delta_{ij} \quad (2.39)$$

and

$$\sum_i |\tilde{\phi}_j\rangle\langle\tilde{p}_i| = 1. \quad (2.40)$$

The transformation \hat{T} is obtained as

$$\hat{T} = 1 + \sum_j (|\phi_j\rangle - |\tilde{\phi}_j\rangle)\langle\tilde{p}_j|. \quad (2.41)$$

With the knowledge of \hat{T} , from variation calculation of the total energy with respect to auxiliary wave function:

$$\frac{\delta E[\psi_n]}{\delta\tilde{\psi}_n^*} = \frac{\delta E[\hat{T}\tilde{\psi}_n]}{\delta\tilde{\psi}_n^*}, \quad (2.42)$$

we obtained the Schrödinger -like equation for auxiliary functions

$$(\tilde{H} - \varepsilon_n \tilde{O})\tilde{\psi}_n = 0, \quad (2.43)$$

where $\tilde{H} = \hat{T}^\dagger H \hat{T}$ and $\tilde{O} = \hat{T}^\dagger \hat{T}$. And the electron density in the Eq. (2.43) can be evaluated as below:

$$\rho(\mathbf{r}) = \sum_n \langle \psi_n | |r\rangle \langle r | | \psi_n \rangle = \sum_n \langle \tilde{\psi}_n | \hat{T}^\dagger | r\rangle \langle r | \hat{T} | \tilde{\psi}_n \rangle. \quad (2.44)$$

Now similar to the direct plane wave method, Eq. (2.43) can be solved by expanding $\tilde{\psi}_n$ to a small number of plane waves.

2.6 Vienna Ab-initio Simulation Package (VASP)

All the computations presented in this dissertation are performed using Vienna Ab-initio Simulation Package (VASP) [79]. This is a computational program package for electronic structure and quantum-mechanical molecular dynamics (MD) calculations from first principles. The approach implemented in VASP is based on DFT using a plane-wave basis set as discussed above and an exact evaluation of the instantaneous electronic ground state at each MD time step.

Plane-wave calculations in VASP always involve integration of smooth periodic functions over the entire Brillouin zone (BZ). This integral can be approximated by discrete set of points in the BZ. VASP includes a full featured symmetry code to determine the symmetry of arbitrary structure automatically. By using point symmetry and selecting special points using Monkhorst-Pack method [80] in VASP, the number of

discrete k-points need to evaluate the integral is greatly reduced. For BZ integrals in metallic systems, discontinued functions at Fermi-level always leads to poor k-points convergence. A finite temperature is artificially introduced to smear the function. Gaussian smearing and Fermi-Direc smearing are available in the VASP for calculation of metals. The VASP code use efficient matrix diagonalisation schemes, such as the blocked Davidson scheme [81] and the residual minimization scheme - direct inversion in the iterative subspace (RMM-DIIS) [82, 83], for the iterative calculation of the lowest Kohn-Sham eigenstates. The VASP use efficient Paulay-Broyden pre-conditioned mixing of the input and output charge densities for iteration calculation [82].

The LDA (LSDA) and GGA approximations for exchange-correlation effect of interacting electrons are implemented in VASP. However, these approximations should be carefully chosen when deal with certain materials. Due to the overbinding tendency inherent in the LDA, LDA underestimated the lattice constant by about 1%. The GGA corrects this intrinsic defect of LDA but overestimates the lattice constant by about the same amount. GGA produces correct ground state for magnetic transition metals while LSDA fails. GGA gives better prediction for surface and adsorption energy over LDA method. LDA works better than GGA for layer crystals such as graphite and molecules crystals where Van Der Waals force is dominant [84]. The interaction between ions and electrons is described by USPP or PAW method which considerably reduces the number of plane waves per atom for transition metals and first row elements. The LDA+U

(GGA+U) approach is also implemented in VASP to take into account strong Coulomb repulsion between electrons in localized orbitals such as $3d$ and $5f$ bands.

Beyond simulations based on DFT, VASP code also allows post-DFT calculations such as many-body perturbation theory (GW) for quasiparticle spectra [85] and dynamical electronic correlations via the random phase approximation [86].

Chapter 3 *Ferroelectric polarization effect on 2DEG*

The 2DEG has unique properties that are promising for applications in all-oxide electronic devices. For such applications it is desirable to have the ability to control 2DEG properties by external stimulus. Here we employ first-principles calculations to investigate $\text{KNbO}_3/\text{ATiO}_3$ (001) ($A = \text{Sr, Pb, Ba}$) heterostructures where perovskites ferroelectrics, KNbO_3 , PbTiO_3 and BaTiO_3 , are used as oxide constituents to create the interface 2DEG. Our results suggest that the polar $(\text{NbO}_2)^+/\text{(AO)}^0$ interface in these heterostructures favors the formation of 2DEG similar to that at the $(\text{LaO})^+/\text{(TiO}_2)^0$ interface in a $\text{LaAlO}_3/\text{SrTiO}_3$ heterostructure. We predict that the presence of spontaneous ferroelectric polarization which can be switched between two stable states allows modulations of the carrier density and consequently the conductivity of the 2DEG. The effect occurs due to the screening charge at the interface that counteracts the depolarizing electric field and depends on polarization orientation. The magnitude of the effect of polarization on the 2DEG properties strongly depends on contrast between polarizations of the two constituents of the heterostructure: the larger is the difference in the two polarizations, the bigger is the effect. For a sufficiently large polarization difference, we predict a metal-insulator transition at the interface driven by polarization reversal. This behavior is found for the $\text{KNbO}_3/\text{PbTiO}_3$ interface and for the $\text{KNbO}_3/\text{BaTiO}_3$ interface when polarizations of KNbO_3 and BaTiO_3 are antiparallel. The

proposed concept of ferroelectrically controlled interface conductivity may be very interesting for memory and logic applications and we hope that our predictions will stimulate experimental studies in this field.

3.1 Introduction

3.1.1 Ferroelectricity in perovskite oxides

Electric polarization created in dielectric and paraelectric materials almost linearly responds to the external electric field. In contrast, a ferroelectric material responds nonlinearly to the external field and has two or more stable states with different nonzero polarization at zero electric field, which is called ‘spontaneous polarization’. Some materials which are not ferroelectric also have the spontaneous polarization, such as wurtzite structure insulators, but their polarization is not switchable. What makes a ferroelectric material interesting is the ability to switch between different spontaneous polarizations states using the external electric field. This property gives ferroelectric materials broad applications in memory and microwave devices [6, 87]. The most studied ferroelectrics nowadays are perovskite oxides. The reason is that these materials are easy to make.

Perovskite oxides are a class of materials with chemical formula ABO_3 , where O is oxygen, A and B are cations. In the high symmetric cubic phase, the A atom is sitting at the corner of the cube, the B atom is located at the center of the cube and oxygens sit at the center of each face, as shown in Figure 3.1(a). In addition, B is at the center of an

octahedron cornered by 6 oxygens, and A is at the center of a hole formed by these octahedral with 12 oxygens at corners. Alternatively viewed from the [001] direction, this structure is formed by alternating the AO and BO₂ layers.

The stability of the cubic phase is fragile, and can be estimated by the empirical criterion of Goldschmidt (1926) [88]. While the ionic radius of A is too small to contact the holes, rotation and tilting will be developed to make the contact possible, as happened in CaTiO₃. When the ionic radius of B is too small to contact the oxygen octahedron, it tends to develop a relative displacement to oxygen in the BO₂ plane and thus forms a dipole moment and possibly creates a ferroelectric polarization [89].

More generally, the polarization in these perovskite ferroelectrics is characterized by relative displacement between cations (both A and B) and oxygen anions, as seen from Figure 3.1 (b). BaTiO₃, PbTiO₃ and KNbO₃ are three representative perovskite ferroelectrics and will be used as components in the heterostructures to be discussed below. BaTiO₃ has a ferroelectric tetragonal phase between 278K and 393K. Above that range it has a cubic paraelectric phase. Below that range it transforms to orthorhombic, and finally to rhombohedral phase at 183K. KNbO₃ has the same transition pattern as BaTiO₃. It has three transitions from paraelectric cubic to ferroelectric tetragonal, to ferroelectric orthorhombic, and to ferroelectric rhombohedral phase at transition temperatures 701K, 488K and 210K respectively [90]. In contrast, PbTiO₃ has only one transition from cubic to ferroelectric tetragonal at 760K. In this chapter, we consider the ferroelectric perovskites in the tetragonal phase under strain applied by SrTiO₃ substrate

at room temperature.

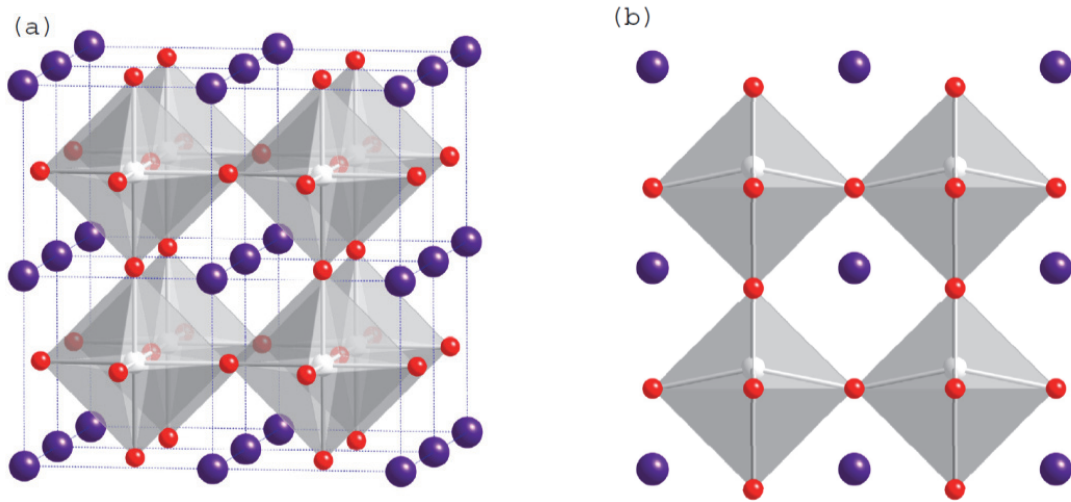


Figure 3.1 (a) cubic perovskite structure ABO_3 . B (gray) is at center of oxygen (red) octahedron. A (blue) is at the center of a hole formed by these octahedral. (b) ferroelectric tetragonal phase of ABO_3 in (010) direction.

3.1.2 Field controlled 2DEG

Using a 2DEG system to make a field-effect device is an important step toward practical applications. The interface of a heterostructure with 3 unit cell thick $LaAlO_3$ on top of $SrTiO_3$ was found insulating. And it was demonstrated that operating at room temperature in field-effect configuration, an insulator-metal phase transition can be achieved by gate voltages [46]. Surprisingly this 2DEG formed at $LaAlO_3/SrTiO_3$ interface has a certain memory behavior which is not observed in conventional dielectric

field-effect device [46].

It was demonstrated that nanosize conducting dots with densities $> 10^{14}$ inch⁻² and lines with widths of about 3nm can be created and erased just using voltage applied by conducting atomic force microscope probe [91]. A possible explanation of this switching behavior is that by application of positive and negative voltage oxygen on the surface of LaAlO₃ is removed and adsorbed respectively. The oxygen vacancy on top of the LaAlO₃ modifies the intrinsic field in LaAlO₃ and thus the carrier density [91]. Other studies imply absorption of hydrogen and water could also play an important role in the switching process [92, 93]. Using the same technique, tunnel junctions and field-effect transistors with characteristic dimensions as small as 2 nanometers were created without using destructive lithography techniques [47].

All of the field-controlled devices above depend on the induced defects or adsorbed molecules which are impossible to control. In this chapter, we propose a prototype for a field-controlled device which is independent on external environment. The switching behavior is completely determined by the internal property, i.e. spontaneous polarization of ferroelectrics.

The effect of spontaneous polarization on the 2DEG has been already demonstrated experimentally. It was observed in ZnO/Mg_xZn_{1-x}O [16][94] and GaN/Al_xGa_{1-x}N [95] heterostructures where a sheet charge is formed at the interface to relax the electrostatically unfavorable state. Using a ferroelectric oxide material as one (or both) constituent of the 2DEG heterostructure allows the control of the 2DEG properties by

ferroelectric polarization switching.

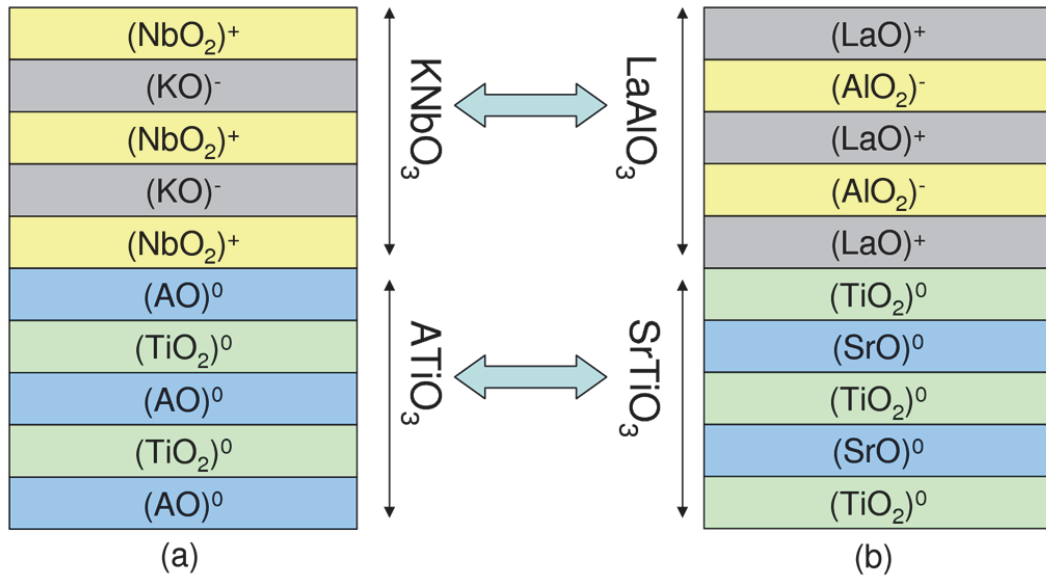


Figure 3.2 $(\text{NbO}_2)^+ / (\text{AO})^0$ interface in $\text{KNbO}_3 / \text{ATiO}_3$ heterostructure (a) as an analogue of $(\text{LaO})^+ / (\text{TiO}_2)^0$ interface in $\text{LaAlO}_3 / \text{SrTiO}_3$ heterostructure (b).

To explore the effect of ferroelectricity on electronic properties at the interface of all oxide heterostructure, we consider oxide heterostructures composed of ferroelectric layers. The particular systems chosen for this study are $\text{KNbO}_3 / \text{ATiO}_3$ (001) (A = Sr, Pb and Ba) oxide heterostructures. Ferroelectric KNbO_3 has alternating charge layers of $(\text{NbO}_2)^+$ and $(\text{KO})^-$ along the [001] direction similar to those of LaAlO_3 as shown in Figure 3.2. A generalized perovskite form ATiO_3 consists of alternating planes of $(\text{TiO}_2)^0$ and $(\text{AO})^0$. A specific analogy is the neutral planes $(\text{TiO}_2)^0$ and $(\text{SrO})^0$ in the SrTiO_3 .

Similar to $(\text{LaO})^+ / (\text{TiO}_2)^0$, the polar discontinuity at the $(\text{NbO}_2)^+ / (\text{AO})^0$ interface in the $\text{KNbO}_3 / \text{ATiO}_3$ heterostructure leads to potential divergence which needs to be removed by electron transfer. The $(\text{NbO}_2)^+ / (\text{SrO})^0$ interface in $\text{KNbO}_3 / \text{ATiO}_3$ is expected to be compensated electronically leading to the conducting interface. On the other hand, the presence of the free charge at the interfaces allows for the growth of a superlattice with stable polarized regions and large polarization discontinuities at the internal interfaces, as was shown recently using first-principles calculations for a $\text{SrTiO}_3 / \text{KNbO}_3$ system [96].

We will show in the next sections that the 2DEG is indeed formed at the $(\text{NbO}_2)^+ / (\text{AO})^0$ interface, and the conducting properties of the 2DEG can be switched by the orientation of the spontaneous polarization.

3.2 Theoretical approach

3.2.1 Computational method

Our theoretical studies are performed using methods described in Chapter 2. The electron wave functions are expanded in a plane wave basis set limited by a cutoff energy of 500eV. Spin-orbit corrections are not included in the calculations. The bulk and superlattice calculations are performed using the 6x6x6 and 8x8x1 Monkhorst-Pack [80] k-point mesh respectively. The self-consistent calculations are converged to 10^{-5} eV/cell and the structures are relaxed until the forces on the ions are less than 0.02 eV/Å.

3.2.2 Properties of bulk perovskites SrTiO₃, KNbO₃, BaTiO₃ and PbTiO₃

We consider perovskite superlattices grown on (001) SrTiO₃ single-crystal substrates. Thus in-plane lattice constant of the superlattice is fixed to the experimental lattice constant of SrTiO₃ which is $a = 3.905 \text{ \AA}$ [97]. By varying the out-of-plane lattice constant c in a paraelectric configuration and minimizing the total energy, the lattice constant c of bulk BaTiO₃, SrTiO₃ and KNbO₃ are calculated to be 4.143 \AA , 3.983 \AA and 4.049 \AA respectively. The obtained tetragonal structures of the perovskites are used as building blocks of all the superlattices with constituents in paraelectric states with mirror plane symmetry and with spontaneous polarization where reflection symmetry is broken [98]. However, the out-of-plane lattice constant c of PbTiO₃ without ionic relaxation (4.018 \AA) is used only in superlattice in paraelectric state. With large polarization in ferroelectric state, the out-of-plane lattice constant of PbTiO₃ in the ferroelectric state will be much different from that in the paraelectric state. When the ferroelectric state is developed in the PbTiO₃ in superlattice, we used an out-of-plane lattice constant of 4.530 \AA obtained by minimizing the total energy with full ionic relaxation. Here, the tetragonal distortion c/a is 1.16, which is consistent with the GGA result of Ref. [99], but which overestimates the experimental value of $c/a = 1.06$ at room temperature [100]. It is known that the GGA approximation in general overestimates the tetragonal distortion in ferroelectrics (see, e.g., Ref. [101]). However, the predicted value of polarization of PbTiO₃ is consistent with experimental data as discussed in the next paragraph.

When the bulk ATiO₃ structures with the in-plane constraint $a = 3.905 \text{ \AA}$ are in the

ferroelectric state, the polarizations of BaTiO₃, KNbO₃ and PbTiO₃ obtained by using the Berry Phase Method [102] are 0.43 C/m², 0.41 C/m², and 1.16 C/m², respectively. These values are consistent with the experimental values of 0.46 C/m² [103], 0.37 C/m² [104], and 0.97 C/m² [105], for polarizations of BaTiO₃, KNbO₃ and PbTiO₃ respectively and the previous theoretical calculations [98, 99, 106]. It is notable that the calculated polarization of PbTiO₃ is much larger than the calculated polarization of both KNbO₃ and BaTiO₃, which has an important implication for our results as discussed in Sec 3.3.

The calculated band gaps of bulk KNbO₃, SrTiO₃, BaTiO₃, and PbTiO₃ with the in-plane constraint are very close in magnitude, i.e. 2.0 eV, 2.0 eV, 1.8 eV and 2.0 eV respectively. These values are lower than the experimental values of 3.3 eV [107], 3.3 eV [108], 3.3 eV and 3.4 eV [109], respectively, due to well-known deficiency of DFT calculations [66]. However, similar to our calculations they are very close in magnitude. This fact has an important implication for the formation of 2DEG at the KNbO₃/ATiO₃ (A = Sr, Pb, and Ba) interfaces, which makes it different from the LaAlO₃/SrTiO₃ interfaces, where both the calculated (3.7 eV) and the experimental (5.6 eV [109]) gaps in LaAlO₃ are much higher than those in SrTiO₃.

3.2.3 Structural model for superlattices

We employed periodic boundary conditions for the superlattice. With building blocks obtained above, the superlattices are constructed as (KNbO₃)_m/(ATiO₃)_n (A = Sr, Ba, and Pb) with $m = 8.5$ unit cells of KNbO₃ and $n = 8.5$ unit cells of ATiO₃ along the [001]

direction. Figure 3.3 shows the interface geometry of the superlattice. The two interfaces have the same termination, i.e. NbO_2/AO . This implies a non-stoichiometric KNbO_3 which is terminated by the NbO_2 monolayers on both sides. In this case an “extra” electron is introduced into the system due to an electron on the additional NbO_2 monolayer. As we will see in Sec 3.3, the Fermi level moves above the conduction band at the interface and thus there is a 2DEG.

The interface separation distance in the $\text{KNbO}_3/\text{ATiO}_3$ heterostructure is determined by minimizing the total energy of a smaller superlattice ($m = 2.5$ and $n = 1.5$) keeping the in-plane and out-of-plane lattice constants in KNbO_3 and ATiO_3 subunits unchanged. The left and right NbO_2/AO interfaces (see Figure 3.3) in the heterostructure are symmetric when both KNbO_3 and ATiO_3 are in paraelectric states. However, when ferroelectric states are developed, the interface to the right is equivalent to the interface to the left with electric polarization reversed. This allows us to study the effects of polarization reversal on the interface electronic properties by considering two interfaces in a single heterostructure.

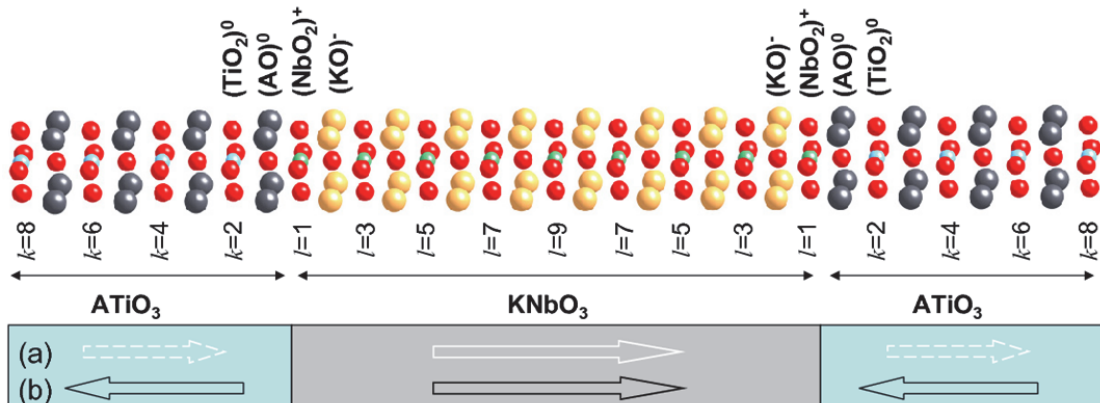


Figure 3.3 Atomic structure of the unit cell and the $(\text{NbO}_2)^+ / (\text{AO})^0$ interfaces in a $(\text{KNbO}_3)_{8.5} / (\text{ATiO}_3)_{8.5}$ (001) superlattice with parallel (a) and antiparallel (b) polarization indicated by white and black arrows respectively.

First, we consider a reference paraelectric state in which lattice parameters of the two components in the heterostructure are kept the same as found above for the bulk structures. Only the interface separation is relaxed to minimize the total energy of the whole system. Next, we consider a ferroelectric state: we relax all the ions in the $\text{KNbO}_3 / \text{ATiO}_3$ superlattices starting with the displacement pattern of the bulk tetragonal soft mode [110, 111] (with polarization pointing from left to right), and minimize the total energy with respect to atomic coordinates of all atoms in the heterostructures keeping the lattice constants unchanged. The ferroelectric states are stable with respect to the paraelectric states by energies -1.18, -1.43 and -0.91 eV/supercell for $\text{KNbO}_3 / \text{BaTiO}_3$, $\text{KNbO}_3 / \text{PaTiO}_3$, $\text{KNbO}_3 / \text{SrTiO}_3$ heterostructures, respectively.

Within the GGA approximation, the SrTiO_3 in the superlattice shows polar atomic

displacements. Since SrTiO₃ is not a ferroelectric material in the bulk, we also investigate the interfaces of the KNbO₃/SrTiO₃ superlattice by fixing the atomic positions in the middle eight monolayers in SrTiO₃. Finally, in KNbO₃/BaTiO₃ heterostructure, we consider polarizations in KNbO₃ and BaTiO₃ pointing opposite to each other in order to verify our explanation of the switching behavior and to introduce one more avenue to realize metal-insulator transition at the interface.

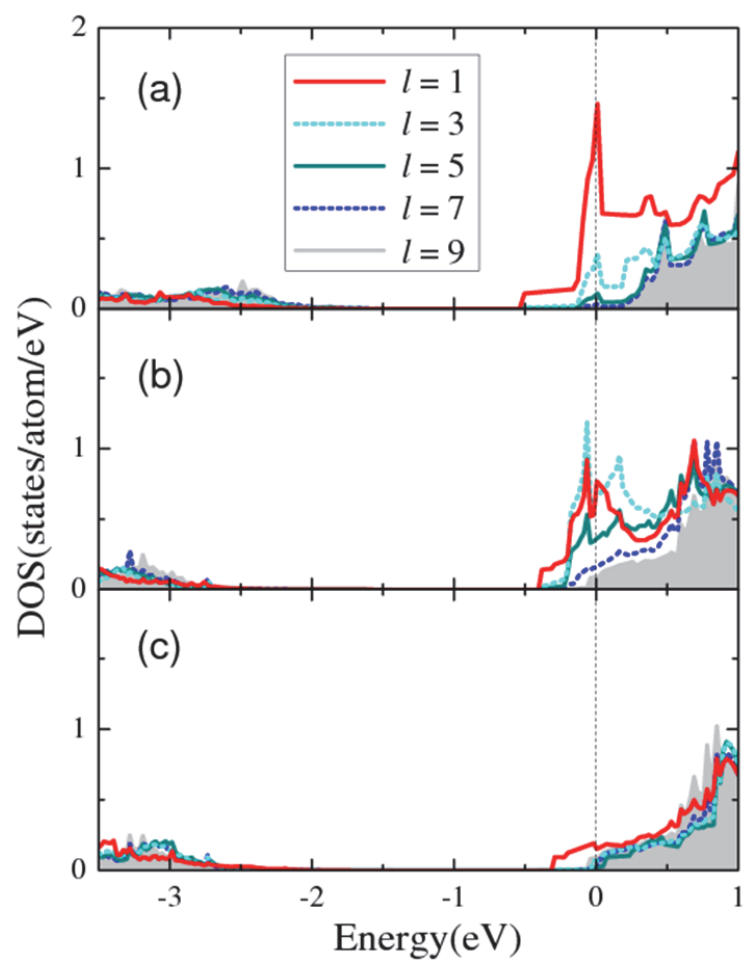
3.3 Results and discussion

3.3.1 SrTiO₃/KNbO₃

First, we investigate properties of (NbO₂)⁺/(SrO)⁰ interface in (KNbO₃)_{8.5}/(SrTiO₃)_{8.5} heterostructure in a paraelectric state. Figures 3.4(a) and 3.4(d) show the density of states (DOS) projected onto 4d-orbitals of Nb atoms (Figure 3.4(a)) and 3d-orbitals of Ti atoms (Figure 3.4(d)), located at different NbO₂ or TiO₂ monolayers l and k respectively away from the (NbO₂)⁺/(SrO)⁰ interface. Apparently, there are occupied conducting states at and below the Fermi energy, thus n -type metallic state is obtained at the interface. As is evident from Figures 3.4(a,d), the occupation of these states is largest near the interface (i.e. for $l = 1$ and $k = 2$) and decreases with increasing distance from the interface. These occupied states are similar to those at the (LaO)⁺/(TiO₂)⁰ interface in LaAlO₃/SrTiO₃ heterostructures. However, due to a smaller band gap in KNbO₃ (the calculated value is 2.0eV) as compared to that in LaAlO₃ (the calculated value is 3.7eV), the KNbO₃ conduction band minimum in the KNbO₃/SrTiO₃ heterostructure lies much closer to the

Fermi energy, i.e. about 0.4eV, which makes it energetically favorable to bend and populate the conduction bands of KNbO₃ that are mainly formed by the Nb 4d-orbitals (see Figure 3.4(a)). This is different from the LaAlO₃/SrTiO₃ heterostructure where the LaAlO₃ conduction bands lie 2.6eV above the Fermi level and consequently almost do not participate in the 2DEG formation.

Next, we investigated the interface of the (KNbO₃)_{8.5}/(SrTiO₃)_{8.5} superlattice in a ferroelectric state with polarization pointing from left to right. We fix eight middle monolayers of SrTiO₃ and relax all the other atomic positions in the superlattice. Figure 3.5(a) shows the ferroelectric displacements of the cations (Nb, Ti, K, Sr) relative to the oxygen anions in the heterostructure. The symmetry between the left and right interfaces (see Figure 3.3(a)) is broken by the ferroelectricity resulting in the deviation between electronic structures at the two interfaces as compared to paraelectric (centrosymmetric) state. We find that ferroelectric displacements in the central monolayers of KNbO₃ are close to those found in the bulk KNbO₃ constrained to have the in-plane lattice constant $a = 3.905 \text{ \AA}$.



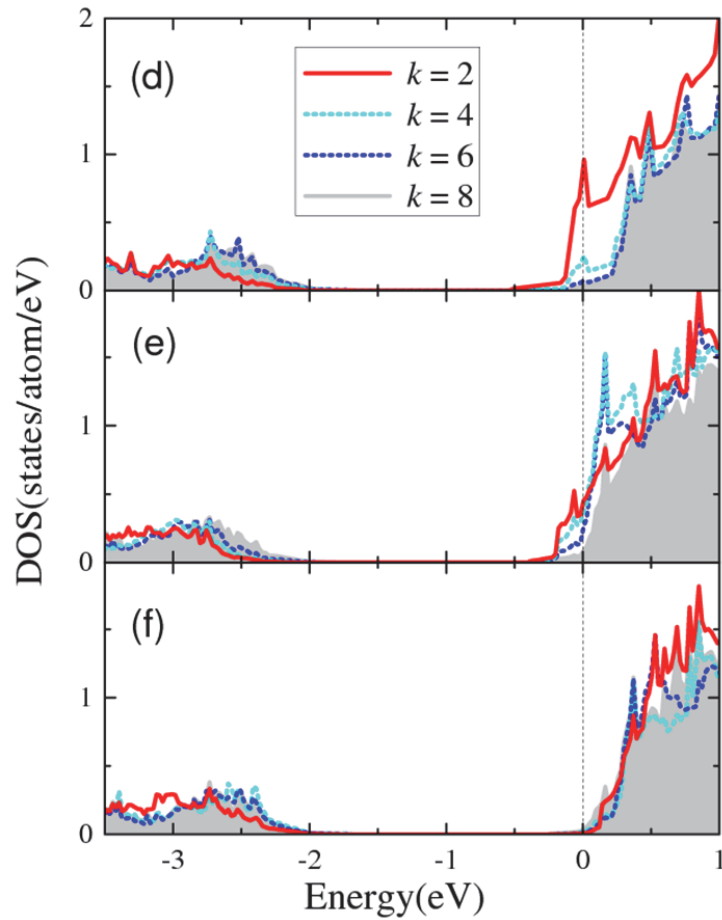
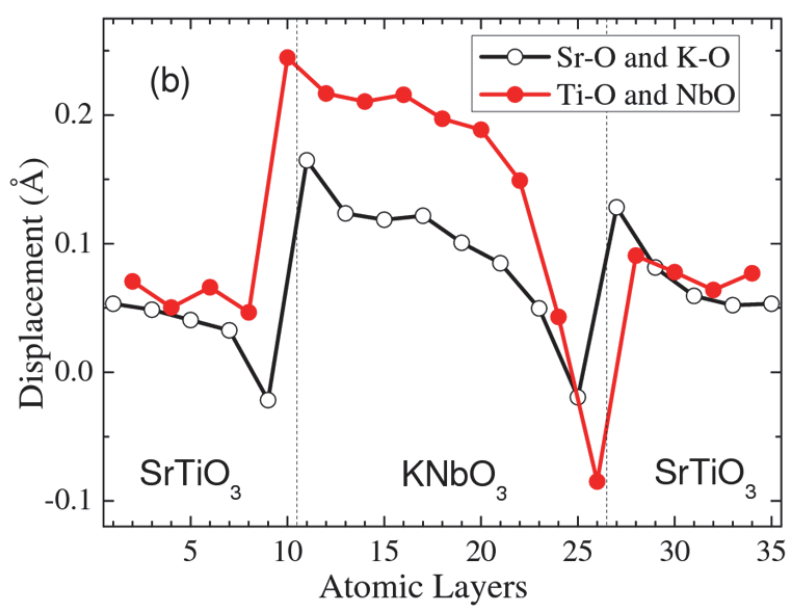
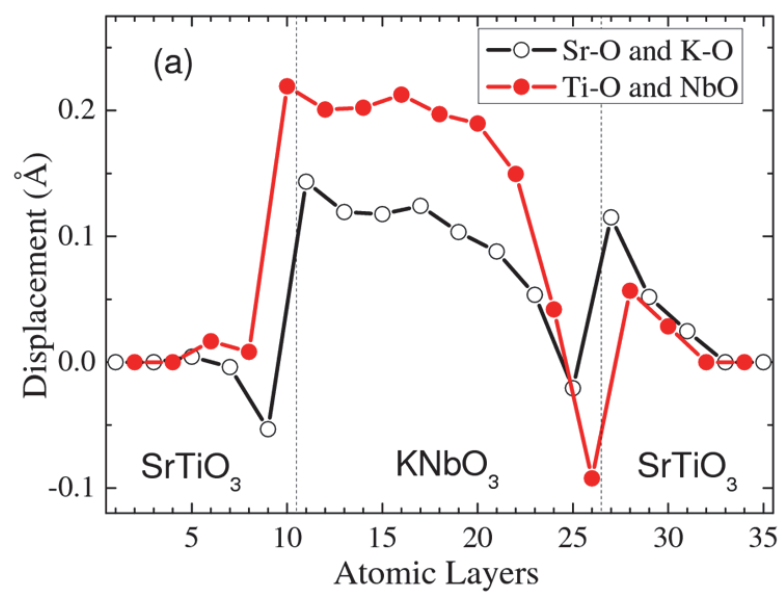


Figure 3.4 Layer-projected density of states (DOS) on 4d-orbitals of Nb atoms (a, b, c) and 3d-orbitals of Ti atoms (d, e, f) located at different NbO_2 or TiO_2 monolayers l or k from the $(\text{NbO}_2)^+ / (\text{SrO})^0$ interface respectively in the $(\text{KNbO}_3)_{8.5} / (\text{SrTiO}_3)_{8.5}$ superlattice for either interface in the paraelectric state (a, d), the right interface (b, e) and the left interface (c, f) in the ferroelectric state. Layer number indicates the layer counted from the interface. The shaded plots are the DOS of atoms in the central monolayer. The zero along the horizontal axis refers to the Fermi energy.

Figures 3.4(b,c) and Figures 3.4(e,f) show the DOS projected onto the Nb 4d-orbitals

and the Ti 3d-orbitals respectively, located at different NbO₂ or TiO₂ monolayers (l or k respectively) from the right and left of the (NbO₂)⁺/(SrO)⁰ interfaces. For the interface on the left (Figures 3.4(b,e)), the occupancies of both the Nb-4d states and Ti-3d states are reduced significantly as compared to the right interface (Figures 3.4(c,f)) due to the ferroelectric displacements. Thus, in the superlattice the two interfaces are distinguished by the orientation of the ferroelectric polarization. This implies that by reversing the electric polarization, the carrier density of 2DEG at the KNbO₃/SrTiO₃ interface could be changed significantly.

For the KNbO₃/SrTiO₃ heterostructure without constraints in the middle layers of SrTiO₃, we find ferroelectric-type displacements in SrTiO₃ which are seen in Figure 3.5 (b) and (c). An induced polarization in SrTiO₃ is known from experimental studies (see, e.g., Ref. [112]). We note, however, that in our calculations these ferroelectric displacements are partially the result of using the GGA approximation which overestimates the equilibrium lattice constant of SrTiO₃, resulting in the tetragonal distortion of SrTiO₃ when the experimental lattice constant is used to constrain the in-plane lattice parameter. We find, however, that for the superlattice with the unconstrained SrTiO₃ the layer-resolved DOS on Nb and Ti atoms are similar to those in the superlattice where eight middle monolayers in SrTiO₃ are fixed. This indicates that the induced polarization in SrTiO₃ does not affect the result qualitatively due to the fact that the SrTiO₃ subunit in the superlattice is a dielectric at the fringe of ferroelectricity with much smaller spontaneous polarization compared to KNbO₃.



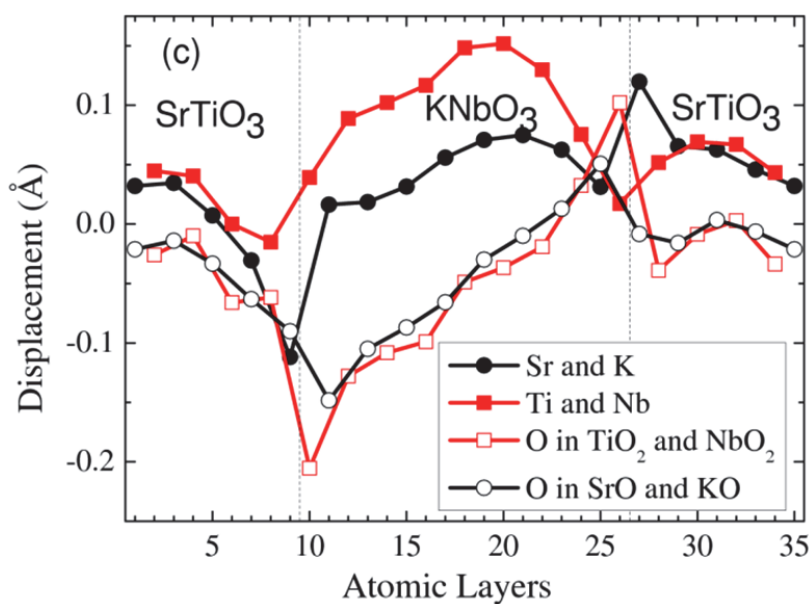
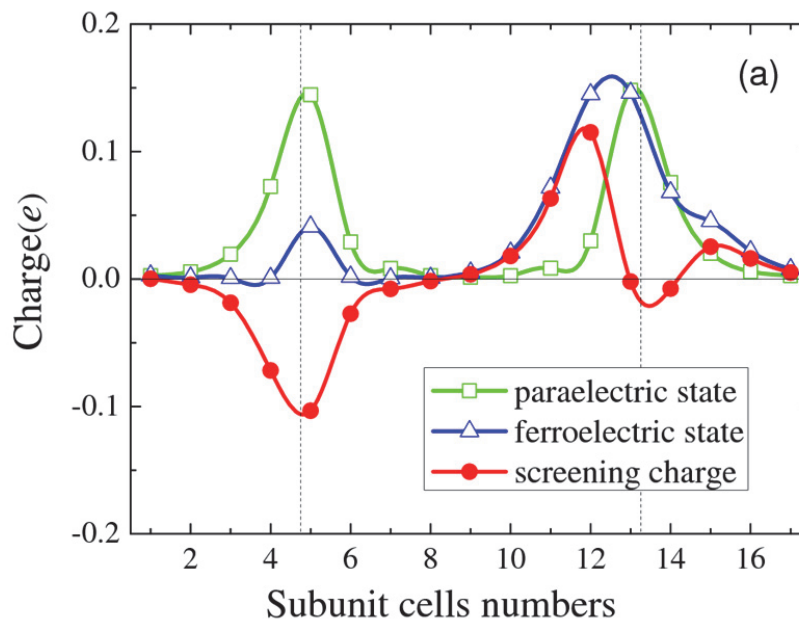


Figure 3.5 Cation (Nb, Ti, K, Sr) displacements with respect to oxygen anions in $(\text{KNbO}_3)_{8.5}/(\text{SrTiO}_3)_{8.5}$ superlattice with eight middle monolayers of SrTiO_3 fixed (a), with all the ions fully relaxed (b) and displacements of all the ions in fully relaxed ferroelectric state (c). Open and solid symbols in (a) and (b) indicate Sr-O (K-O) and Ti- O_2 (Nb- O_2) displacements respectively. Solid circles and squares in (c) indicate Sr (K) and Ti (Nb) displacements, respectively. Open circles and squares in (c) indicate displacements of O atoms in SrO (KO) and TiO_2 (NbO_2) layers, respectively. The two dashed vertical lines indicate left and right NbO_2/SrO interfaces.

The switchable behavior can be understood in terms of the screening of the polarization charge achieved by changing the free electron density of 2DEG at the interface. As discussed above the polarization in SrTiO_3 can be ignored for this consideration. The polarization in KNbO_3 is pointing from the left to the right causing

negative and positive polarization bound charges accumulated at left and right interfaces, respectively. To reduce the depolarization field and thus decrease the energy in the superlattice, the free charge is enhanced at the right interface and reduced at the left interface to compensate polarization charges. This is seen from Figure 3.6 which shows the free charge on Nb and Ti atoms in the paraelectric (open circles) and ferroelectric (open triangles) states. These charges are obtained by integrating the layer dependent DOS shown in Figure 3.4 from the conduction band minimum up to the Fermi energy. Thus each point on the curves in Figure 3.6 shows the number of free electrons on the Nb and Ti sites in the superlattice. Figure 3.6 also shows the screening charges (solid symbols) calculated from the difference between the free charges in the ferroelectric and paraelectric states.



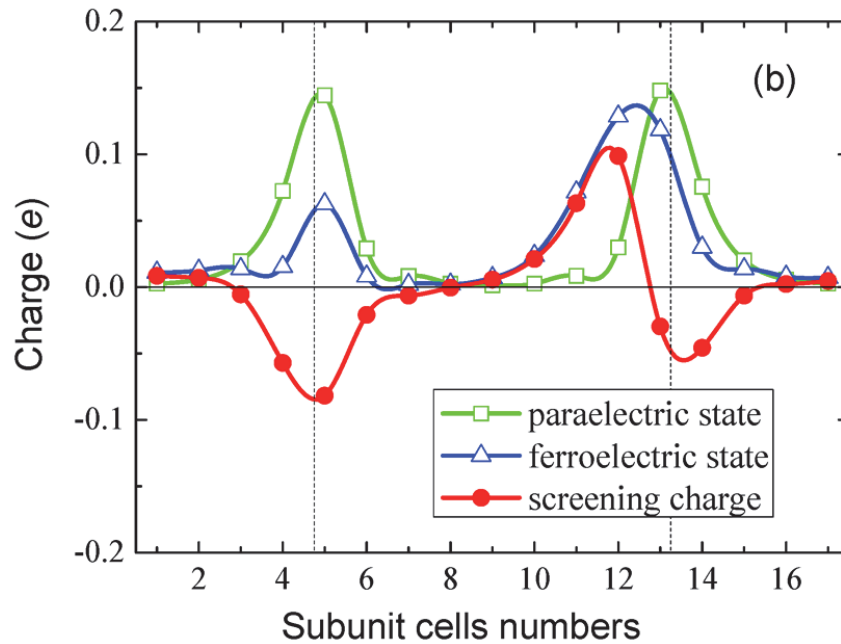


Figure 3.6 The free charge (in units of electron) on Nb and Ti atoms across the unit cell of $(\text{KNbO}_3)_{8.5}/(\text{SrTiO}_3)_{8.5}$ superlattices in paraelectric state and ferroelectric state when the middle layers in SrTiO_3 is fixed (a) and all the ions are fully relaxed (b). The screening charge is obtained by calculating the difference of the free charges on Nb and Ti atoms for ferroelectric and paraelectric states. The directions of polarization for the ferroelectric state are from left to right.

Heterostructure		Ferroelectric: Right interface			Ferroelectric: Left interface			Paraelectric: Either interface		
		Nb	Ti	Total	Nb	Ti	Total	Nb	Ti	Total
Parallel polarizations	$\text{KNbO}_3/\text{SrTiO}_3$: full relaxation	0.36	0.07	0.43	0.09	0.06	0.15	0.19	0.10	0.29
	$\text{KNbO}_3/\text{SrTiO}_3$: middle SrTiO_3 layers fixed	0.39	0.14	0.53	0.05	0.01	0.05	0.19	0.10	0.29

	KNbO ₃ /PbTiO ₃	0.00	0.00	0.00	0.25	0.47	0.72	0.16	0.11	0.27
	KNbO ₃ /BaTiO ₃	0.25	0.03	0.28	0.12	0.15	0.27	0.17	0.09	0.26
Antiparallel polarizations	KNbO ₃ /BaTiO ₃	0.46	0.12	0.58	0.00	0.00	0.00	0.19	0.09	0.26

Table 3.1 Number of electrons on Nb and Ti atoms per lateral unit cell area at two interfaces in the KNbO₃/ATiO₃ (A = Sr, Ba, Pb) heterostructures without polarizations, with parallel and with antiparallel polarizations in each constituent.

Further insight as to how polarization switching influences the density of the 2DEG can be obtained from the number of free electrons accumulated at the two interfaces. We calculate local charges using Wigner-Seitz (WS) spheres that are used by VASP to project the wave functions onto spherical harmonics to calculate partial DOS*. Table 3.1 shows the number of occupied Nb-4d and Ti-3d states integrated from conduction band minimum up to the Fermi energy and added for all the atoms from the middle layer up to the left and right interface. In the paraelectric KNbO₃/SrTiO₃ superlattice, free carriers on left and right interface are calculated to be 0.29 electrons each per unit cell area, which are equal due to the symmetry. In the ferroelectric KNbO₃/SrTiO₃ superlattice with middle layer of SrTiO₃ fixed, free carriers on right and left interface are obtained to be 0.53 electrons and 0.05 electrons per unit cell area. Comparing with the paraelectric state, extra 0.24 electrons are accumulated at the right interface and 0.24 electrons are removed from the left interface. Evidently the induced screening charge has an opposite

* There is no unambiguous way to define WS radii, and we use the default values of 2.138, 1.588, 1.979, 1.725, 1.323, 1.270, and 0.820 Angstroms for the radii of Sr, K, Ba, Pb, Ti, Nb and O atoms respectively provided by the input potential file in the VASP program.

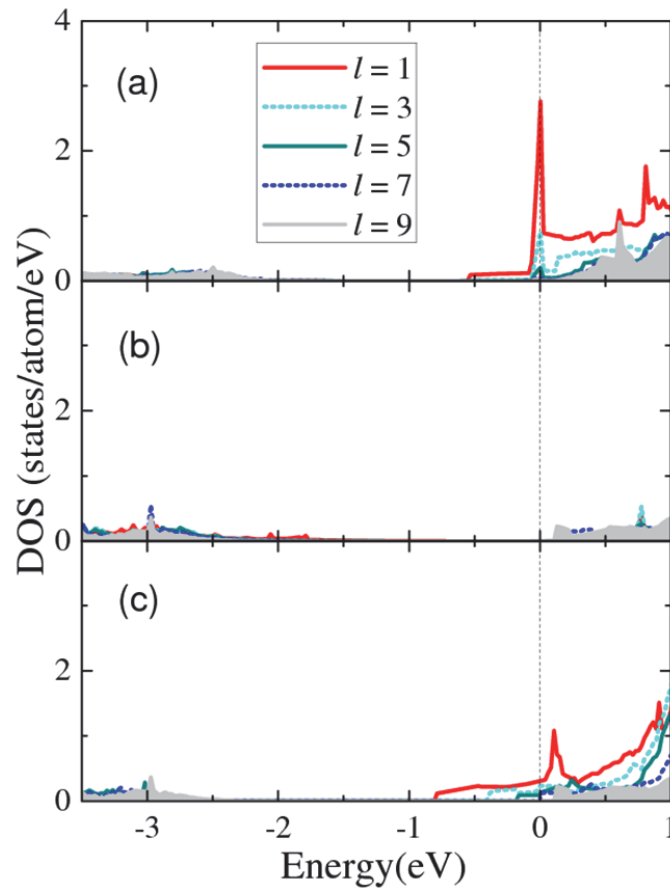
sign to the polarization charge, thereby counteracting the depolarizing electric field. The polarization charge density σ_P can be estimated from the polarization of KNbO_3 in middle layer using the Berry phase method which gives $P_{\text{KNbO}_3} = 0.41\text{C/m}^2$. This corresponds to the polarization charge per unit cell area of $\sigma_P = 0.39e$. The WS charge density at the two interfaces changes by $0.24e$ per unit cell area in going from para- to ferro-electric state. The WS charge density ($0.29e$ per unit cell area) underestimates the actual charge density ($0.5e$ per unit cell area) in the paraelectric state. When scaled with the factor $0.5/0.29$, the change in charge at either interface becomes $0.41e$ per unit cell area which is about the same as the polarization charge density.

In the heterostructure with full structural relaxation, the difference of free charges between two interfaces is not as much as that when the middle layer of SrTiO_3 is fixed due to the small induced polarization in SrTiO_3 . We obtain the polarization of SrTiO_3 from polar displacements (Figure 3.5(b)), using the Berry phase method, of about 0.17C/m^2 . From the difference of the polarizations in KNbO_3 and SrTiO_3 of 0.24C/m^2 , the polarization charge per unit cell area is $\sigma_P = 0.23e$, which is about the same as the screening charge density of $0.14e$ per unit cell area scaled with the factor $0.5/0.29$.

3.3.2 $\text{PbTiO}_3/\text{KNbO}_3$

Here we describe our investigations of the electronic properties at the polar interfaces in the $(\text{KNbO}_3)_{8.5}/(\text{PbTiO}_3)_{8.5}$ heterostructure. When both subunits are in a paraelectric state, similar to the $(\text{NbO}_2)^+/(\text{SrO})^0$ interface in the $\text{KNbO}_3/\text{SrTiO}_3$ heterostructure, the

presence of polar interfaces leads to the formation of 2DEG at the $(\text{NbO}_2)^+ / (\text{PbO})^0$ interfaces in the $\text{KNbO}_3/\text{PbTiO}_3$ heterostructure. This is evident from Figures 3.7 (a,d), which show the Nb-4d and Ti-3d DOS indicating the largest local DOS at the Fermi energy at the monolayers located close to the interface ($l = 1$ and $k = 2$). The local DOS decreases with the distance from the interface. The calculated free carrier densities are 0.27 electrons per unit cell area on both interfaces as shown in Table 3.1.



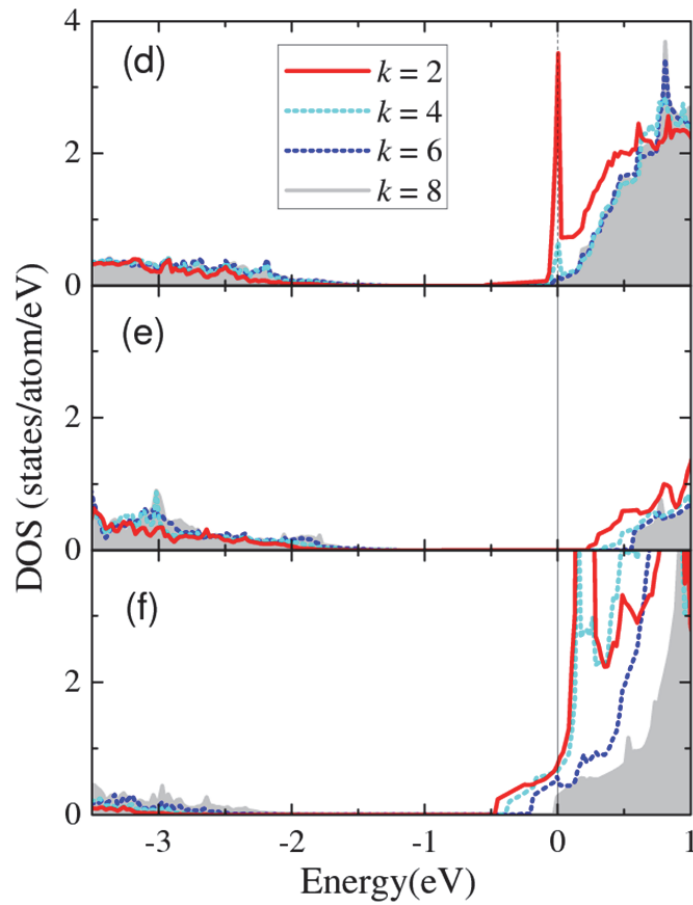


Figure 3.7 Layer-projected density of states (DOS) on 4d-orbitals of Nb atoms (a,b,c) and 3d-orbitals of Ti atoms (d,e,f) located in different monolayers l and k respectively from the $(\text{NbO}_2)^+ / (\text{PbO})^0$ interface in the $(\text{KNbO}_3)_{8.5} / (\text{PbTiO}_3)_{8.5}$ superlattice for either interface in the paraelectric state (a, d), the right interface (b, e) and the left interface (c, f) in the ferroelectric state. Layer number indicates the layer from the interface. The shaded plots are the DOS of atoms in the central monolayer. The zero along the horizontal axis refers to the Fermi energy.

Figure 3.8 shows the ferroelectric displacements of the cations (Nb, Ti, K, Pb)

relative to the oxygen anions in the heterostructure. It can be seen that in the $(\text{KNbO}_3)_{8.5}/(\text{PbTiO}_3)_{8.5}$ heterostructure, the spontaneous polarization of strained PbTiO_3 exceeds significantly the polarization of a KNbO_3 subunit, which leads to positive and negative polarization charge on the left and right interfaces, respectively, even though the polarization for the system points to the right. As follows from our discussion of the $\text{KNbO}_3/\text{SrTiO}_3$ heterostructure, this leads to more free charges at the left interface and less free charges at the right interface to compensate the polarization charges.

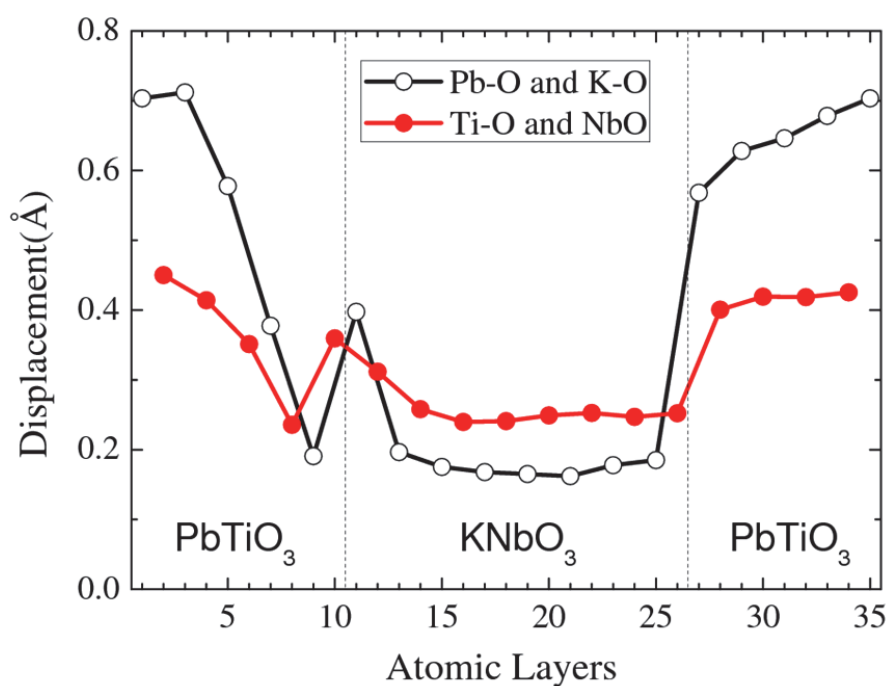


Figure 3.8 Cation (Nb, Ti, K, Pb) displacements with respect to oxygen anions in $(\text{KNbO}_3)_{8.5}/(\text{PbTiO}_3)_{8.5}$ superlattice. Open and solid and symbols indicate Pb-O (K-O) and Ti-O₂ (Nb-O₂) displacements, respectively. The two dashed vertical lines indicate left and right $(\text{NbO}_2)^0/(\text{PbO})^0$ interfaces.

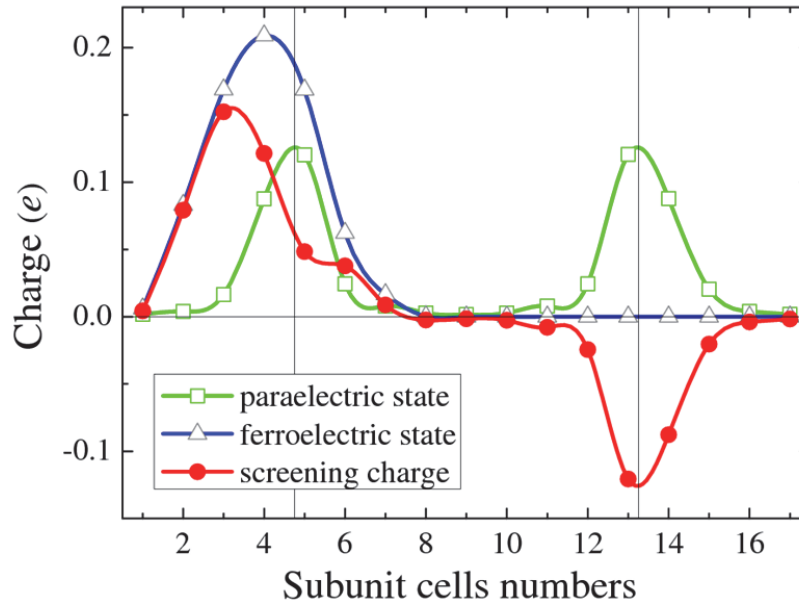


Figure 3.9 The free charge (in units of electron) on Nb and Ti atoms across the unit cell of $(\text{KNbO}_3)_{8.5}/(\text{PbTiO}_3)_{8.5}$ superlattices in paraelectric state and ferroelectric state. The screening charge is the difference of the free charges on Nb and Ti atoms for the ferroelectric and paraelectric states. The direction of the polarization for ferroelectric state is from left to right.

It is seen from Figures 3.7 (b,c,e,f) that for $(\text{KNbO}_3)_{8.5}/(\text{PbTiO}_3)_{8.5}$ heterostructure, the DOS on both the Nb and Ti atoms at the Fermi energy is very large on the left interface (Figures 3.7(c,f)) while that on the right interface is zero (Figures 3.7 (b,e)). This indicates a ferroelectrically induced metal-insulator transition at the interface as a result of polarization reversal. The origin of this behavior can be explained by the large difference in polarizations on the two constituents of the heterostructure. The

polarizations in the middle of KNbO_3 and PbTiO_3 in the superlattice are 0.47C/m^2 and 1.09C/m^2 , respectively. This results in a negative polarization charge of $0.58e$ per unit cell area at the right interface, which expels all the free carriers of $0.5e$ per unit cell area on that interface leading to an insulating right interface. This metal-insulator transition at the interface is visualized by the free charge distribution in Figure 3.9. Thus, a metal-insulator transition at the interface with polarization reversal is expected at the interface of the two constituents with a large difference in their polarizations.

3.3.3 $\text{BaTiO}_3/\text{KNbO}_3$

Similar to the polar interfaces considered above, the $\text{KNbO}_3/\text{BaTiO}_3$ system exhibits a 2DEG at the $(\text{NbO}_2)^+/(\text{BaO})^0$ interface. This is seen from the Nb-4d and Ti-3d DOS shown in Figures 3.10 (a,d) for the heterostructure in a paraelectric state. Again we see the largest occupied DOS near the Fermi energy at the interfacial layers which decreases when moving away from the interface. The calculated free carrier densities are $0.26e$ per unit cell area on both interfaces as shown in Table 3.1.

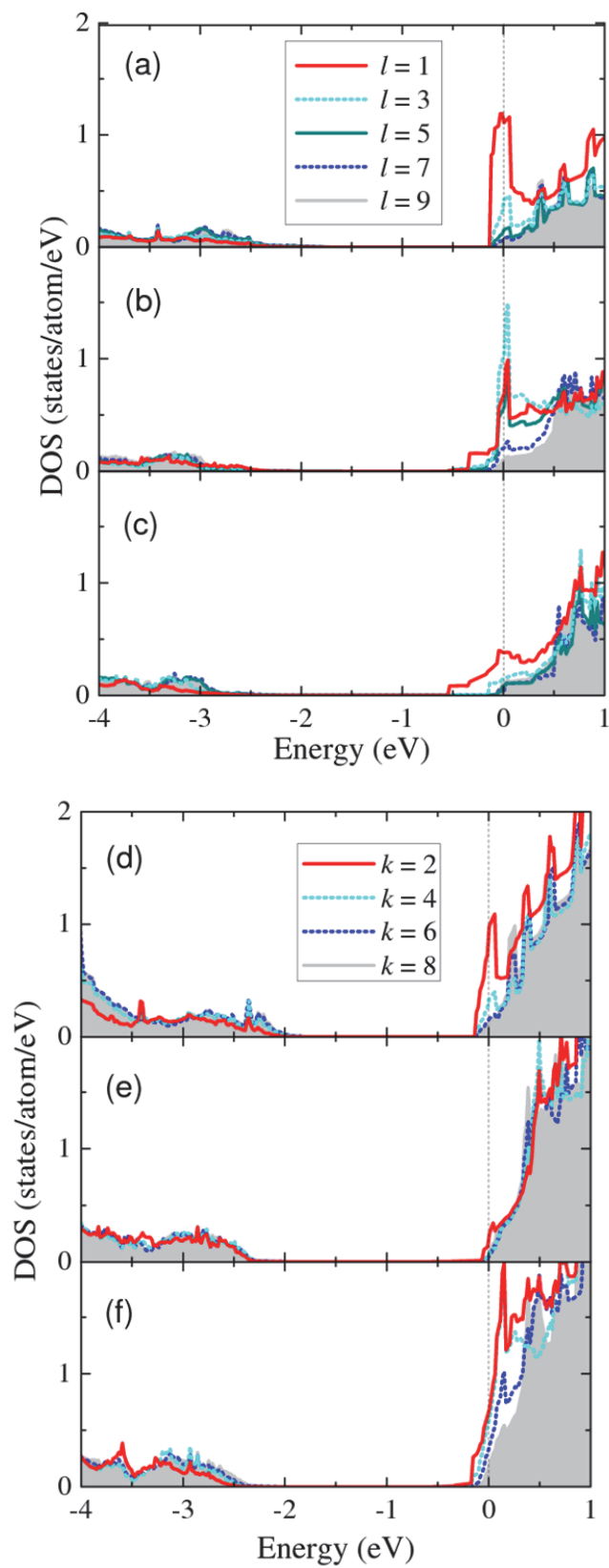


Figure 3.10 Layer-projected density of states (DOS) on 4d-orbitals of Nb atoms (a,b,c) and 3d-orbitals of Ti atoms (d,e,f) located in different monolayers l and k respectively away from the $(\text{NbO}_2)^+/\text{(BaO)}^0$ interface in the $(\text{KNbO}_3)_{8.5}/(\text{BaTiO}_3)_{8.5}$ superlattice for either interface in the paraelectric state (a, d), the right interface (b, e) and the left interface (c, f) in the ferroelectric state. Layer number indicates the layer from the interface. The shaded plots are the DOS of atoms in the central monolayer. The zero along the horizontal axis refers to the Fermi energy.

When the ferroelectric state is developed in the $\text{KNbO}_3/\text{BaTiO}_3$ heterostructure, the ferroelectric displacements in KNbO_3 and BaTiO_3 appear to be similar in magnitude. This is seen from Figure 3.11 (a), which shows the displacements of the cations (Nb, Ti, K, Ba) relative to the oxygen anions. This leads to the comparable polarizations of strained BaTiO_3 and KNbO_3 in the heterostructure, mirroring the similarity of their bulk polarizations 0.41C/m^2 and 0.43C/m^2 for KNbO_3 and BaTiO_3 , respectively. This behavior is different from $\text{KNbO}_3/\text{SrTiO}_3$ and $\text{KNbO}_3/\text{PbTiO}_3$ systems, where the polarization discontinuity was pronounced at the interfaces.

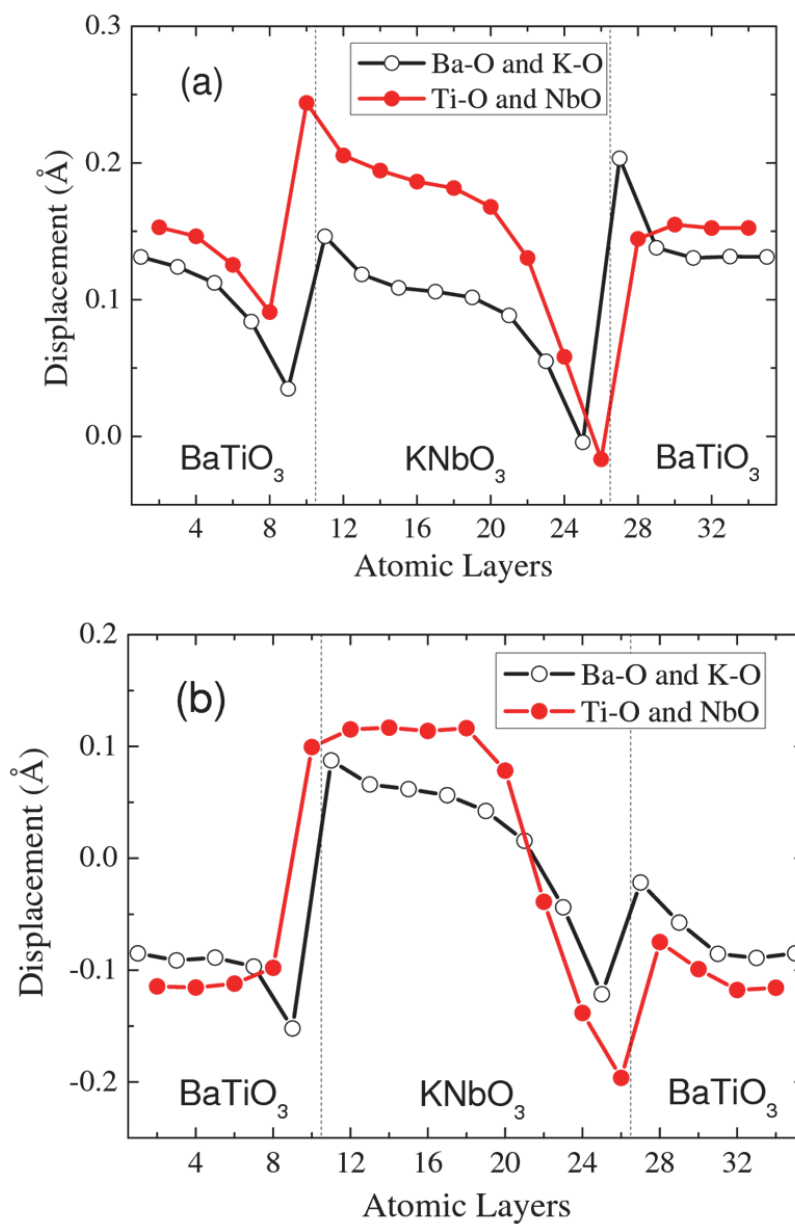
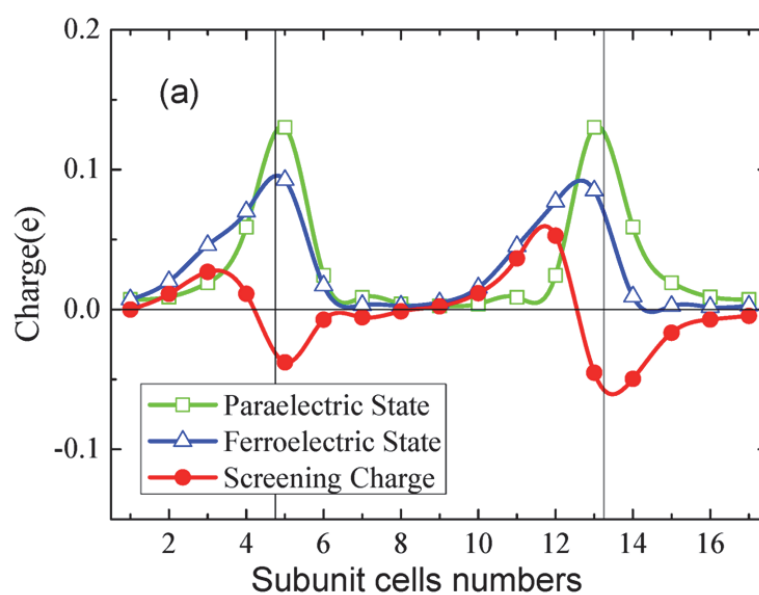


Figure 3.11 Cation (Nb, Ti, K, Ba) displacements with respect to the oxygen anions in the $(\text{KNbO}_3)_{8.5}/(\text{BaTiO}_3)_{8.5}$ superlattice with parallel polarizations pointing from left to right (a) and with antiparallel polarizations pointing toward each other (b). Open and solid symbols indicate Ba-O (K-O) and Ti-O₂ (Nb-O₂) displacements respectively. The two dashed vertical lines indicate the left and right $(\text{NbO}_2)^0/(\text{BaO})^0$ interfaces.

The similar polarization values of BaTiO₃ and KNbO₃ lead to the net polarization charge of almost zero at the two interfaces for parallel polarizations resulting in the small difference in the density of free carriers at two interfaces as indicated in Table 3.1. We note that the layer-resolved DOS of Ti is larger at the left interface than at the right interface while it is opposite for the layer-resolved DOS of Nb as is clearly seen from the comparison of Figures 3.10 (b) and (c) and Figures 3.10 (e) and (f). This asymmetric behavior is a direct result of opposite screening charges extending to several layers away from the interfaces to compensate the inhomogeneous polarization charge in each constituent. This can be seen from the screening charge distribution in each constituent in Figure 3.12(a).



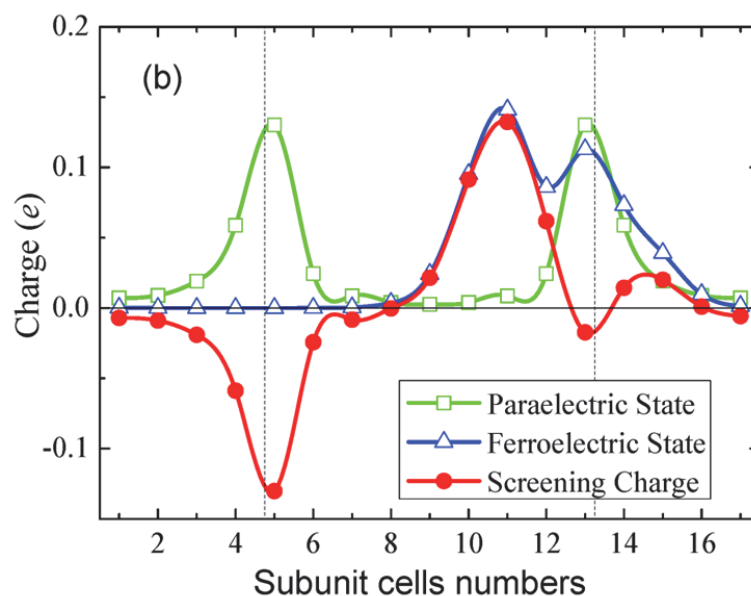


Figure 3.12 The free charge (in units of electron) on Nb and Ti atoms across the unit cell of $(\text{KNbO}_3)_{8.5}/(\text{BaTiO}_3)_{8.5}$ superlattices in paraelectric state and ferroelectric state with (a) polarizations in the same direction from left to right and (b) opposite polarizations. The screening charge is the difference of the free charges on Nb and Ti atoms for ferroelectric and paraelectric states.

We see, therefore, that there is no pronounced switching effect at the conducting NbO_2/BaO interface in the $\text{KNbO}_3/\text{BaTiO}_3$ heterostructure when polarizations of the two constituents are in the same direction. However, we predict a metal-insulator transition at the NbO_2/BaO interface with polarizations reversal when the polarizations in KNbO_3 and BaTiO_3 point opposite to each other. It has been predicted that while electrical compatibility constrain normally prevent head-to-head and tail-to-tail domain walls from

forming in ferroelectric materials, such domain walls could be stabilized by delta-doping supplying a substitutional charge density that provides a cancellation of the bound polarization charge [113]. In our case the stabilization of the domains with the opposite polarization orientation is provided by the presence of the free charges at the interfaces. This antiparallel polarization state of the $\text{KNbO}_3/\text{BaTiO}_3$ heterostructures is stable with respect to the paraelectric states by energies of -0.86eV/supercell . On the left interface, the polarizations of BaTiO_3 and KNbO_3 are pointing away from the NbO_2/BaO interface while on the right interface the polarizations are pointing toward interface as shown in Figure 3.3(b). We find that the total energy of the superlattice in the parallel polarization state is lower by 0.32eV/supercell than that in the antiparallel state. The polarizations of BaTiO_3 and KNbO_3 in the heterostructure are -0.26C/m^2 and 0.25C/m^2 , respectively, causing $-0.49e$ and $0.49e$ polarization charges per unit cell area on the left and right interface, respectively. The magnitude of the polarization charges is close to that of the free carriers (i.e. $0.5e$) at the interfaces in paraelectric heterostructure. Thus, to stabilize the ferroelectric state with the antiparallel polarization almost all the free charge needs to be removed from one interface and placed to the other interface. This causes a metal-insulator transition at the interface by the polarization reversal as explained in the section describing a $\text{KNbO}_3/\text{PbTiO}_3$ heterostructure.

The presence of the ferroelectrically induced metal-insulator transition at the interface is seen from the calculated charge distribution in the $\text{KNbO}_3/\text{BaTiO}_3$ heterostructure with antiparallel polarization as shown in Figure 3.12(b). It is seen that

while in the paraelectric state the free charge is equally localized at the two interfaces, the antiparallel ferroelectric polarization state eliminates the charge from the left interface and places it to the right interface. It is notable that the distribution of this charge is not symmetric with respect to the interface reflecting complex structural relaxations at this interface evident from Figure 3.11 (b).

3.4 Summary

We have explored the formation of 2DEG and its dependence on the electric polarization at the $(\text{NbO}_2)^+ / (\text{AO})^0$ interface in the $(\text{KNbO}_3) / (\text{ATiO}_3)$ ($A = \text{Sr, Pb, and Ba}$) oxide heterostructures using first-principles methods. The chosen structures have ferroelectric constituents besides having polar discontinuity similar to that at the interface in $(\text{LaAlO}_3) / (\text{SrTiO}_3)$ heterostructure. The interfaces are found to have occupied Nb 4d-states and Ti 3d states around the Fermi energy leading to conducting interfaces with n -type carriers.

We have predicted that the conducting properties at the two interfaces in these systems are influenced by ferroelectricity. Switching the ferroelectric polarization orientation may cause significant changes in the carrier density and consequently the conductivity of the interfacial 2DEG. The effect of the polarization reversal on the interface carrier density is understood in terms of screening by 2DEG. The magnitude of the effect is controlled by contrast between polarizations of the two constituents of the heterostructure: the larger is the difference in the two polarizations, the bigger is the

effect. Our calculations predict that a heterostructure with ferroelectric constituents can be designed such that the density of the 2DEG at the interface can be controlled by an external electric field including the possibility of switchable metal-insulator transition at the interface. These effects may be useful in controlling the interfacial conducting properties in ferroelectric oxide heterostructures by external electric fields.

Chapter 4 *Strain effect on 2DEG*

Properties of the two-dimensional electron gas (2DEG) at interface of insulating oxides LaAlO_3 and SrTiO_3 have attracted significant interest due to its potential applications in nanoelectronics. Control over this carrier density and mobility of the 2DEG is essential for applications of these novel systems, and may be achieved by epitaxial strain. Our experimental collaborators at University of Wisconsin-Madison have investigated $\text{LaAlO}_3/\text{SrTiO}_3$ interfaces with controlled levels of biaxial epitaxial strain by using different substrates with different lattice constants. They found that tensile strained SrTiO_3 destroys the conducting 2DEG, while compressively strained SrTiO_3 retains the 2DEG, but with a carrier concentration reduced in comparison to the unstrained $\text{LaAlO}_3/\text{SrTiO}_3$ interface. They also found that the critical LaAlO_3 overlayer thickness for 2DEG formation increases with SrTiO_3 compressive strain. Here we use density functional calculations to explore this behavior. Our results suggest that a strain-induced electric polarization in the SrTiO_3 layer is responsible for this behavior. We find that it is directed away from the interface and hence creates a negative polarization charge opposing that of the polar LaAlO_3 layer. This both increases the critical thickness of the LaAlO_3 layer, and reduces carrier concentration above the critical thickness, in agreement with the experimental results. Our findings suggest that epitaxial strain can be used to tailor 2DEG properties of the $\text{LaAlO}_3/\text{SrTiO}_3$ heterointerface.

4.1 Introduction

Strains have previously been used to engineer and enhance numerous properties of materials. For example, increased mobility in semiconductors [114, 115], and increased transition temperature in ferroelectric materials [116-119] and superconductors [120] have been observed. A recently discovered two-dimensional electron gas (2DEG) at the $\text{LaAlO}_3/\text{SrTiO}_3$ interface [44, 121] has attracted great interest due to its novel application to nanoscale oxide devices [47]. So far, most studies of 2DEGs at oxide interfaces were performed using TiO_2 -terminated SrTiO_3 bulk single crystal substrates. Thus, despite the rich nature of strain effects on oxide materials properties, the relationship between the strain and electrical properties of the 2DEG at the $\text{LaAlO}_3/\text{SrTiO}_3$ heterointerface remains largely unexplored.

The importance of strain effects comes from the fact that integrating 2DEGs to other functional devices or substrates always involves strain. Therefore, it is desirable to know the effect of the strain on 2DEG at the $\text{LaAlO}_3/\text{SrTiO}_3$ interface. In addition, by changing strain we might be able to obtain novel functional properties. For example, strain can induce an electric polarization in otherwise non-polar SrTiO_3 [122]. It has been predicted that polarization can be used to control 2DEG properties at oxide heterointerfaces [123, 124]. Thus by using the relation between the polarization and the strain, we could engineer 2DEG behavior.

4.2 Experimental investigation

Performed by our collaborators at University of Wisconsin-Madison, $\text{LaAlO}_3/\text{SrTiO}_3$ thin films heterostructures were grown on various single crystal substrates using pulsed-laser deposition (PLD) with *in-situ* high pressure reflection high-energy electron diffraction (RHEED) [13]. Figure 4.1 shows the schematic of the thin film heterostructure. Table 4.1 shows substrates that were used in this study to vary the SrTiO_3 strain state from biaxial compressive to biaxial tensile in the plane. As shown in Figure 4.1, (001) SrTiO_3 (STO) thin films were grown on (110) NdGaO_3 (NGO), (001) $(\text{LaAlO}_3)_{0.3}-(\text{Sr}_2\text{AlTaO}_6)_{0.7}$ (LSAT), (110) DyScO_3 (DSO) and (110) GdScO_3 (GSO) substrates. The varying lattice parameters result in an average biaxial strain ranging from -1.21% (compressive) to +1.59% (tensile) in a fully commensurate SrTiO_3 deposited film. All grown single-crystal (001) SrTiO_3 templates were fully coherent with the substrates. (001) SrTiO_3 films were also grown on (001) silicon substrates using molecular beam epitaxy. Thickness of these quasi-single-crystal (001) SrTiO_3 templates on silicon was 100 nm, and the films were almost fully relaxed. The measured SrTiO_3 lattice parameters on Si correspond to an average biaxial strain of 0.15% [125, 126]. The bi-axial strain state and lattice parameters of the strained (001) SrTiO_3 templates are summarized in Table 4.1. LaAlO_3 overlayers were deposited using PLD on these various strain Ti-terminated single crystal SrTiO_3 templates.

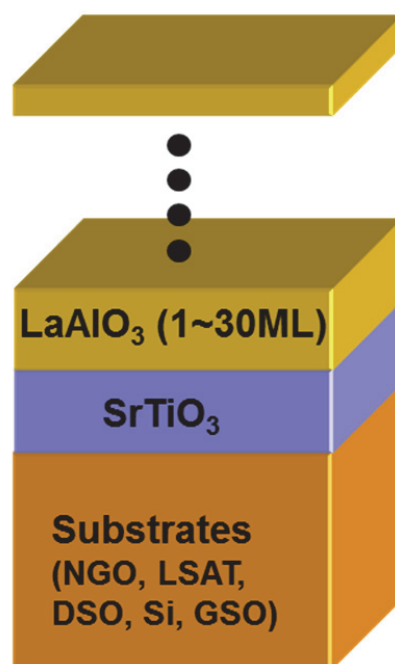


Figure 4.1 Schematic diagram of grown structures. Thickness of LaAlO_3 layer was varied from 1 to 30 unit cells on STO on LSAT, NGO, Si, DSO, GSO substrate

	a (Å)	c (Å)	bi-axial lattice mismatch
<i>LaAlO3 (10uc) on SrTiO3 (50uc) on NdGaO3</i>			
SrTiO3	3.860	3.964	-1.21%
NGO	3.859	3.866	
<i>LaAlO3 (10uc) on SrTiO3 (50uc) on LSAT</i>			
SrTiO3	3.868	3.940	-0.96%
LSAT	3.869	3.387	
<i>LaAlO3 (10uc) on SrTiO3 (120nm) on Si</i>			
SrTiO3	3.911	3.985	0.15%
Si	3.840	3.840	
<i>LaAlO3 (10uc) on SrTiO3 (20uc) on DyScO3</i>			
SrTiO3	3.944	3.939	1.11%
DyScO3	3.944	3.939	
<i>LaAlO3 (10uc) on SrTiO3 (20uc) on GdScO3</i>			
SrTiO3	3.964	3.875	1.59%
GdScO3	3.963	3.967	

Table 4.1 Results from high-resolution x-ray diffraction measurements on the films at room temperature are given. The in-plane (a) and out-of-plane (c) lattice constants and lattice mismatch between the SrTiO₃ films and single crystal substrates on average of two orthogonal directions. The a- and c-lattice parameters of single-crystalline SrTiO₃ are 3.905Å. All SrTiO₃ templates were fully coherent except STO/Si (12). (002), (101) of SrTiO₃ and cubic substrates, LSAT, Silicon (200) pseudo-cubic of (101) pseudo-cubic of orthorombic substrate, GdScO₃ and DyScO₃, NdGdO₃ were observed to determine in-plane and out-of-plane lattice parameters.

It is known experimentally that a conducting 2DEG forms at the LaAlO₃ / bulk SrTiO₃ interface only after the LaAlO₃ overlayer thickness exceeds a

critical value of 4 unit cells [46]. It was found that this critical thickness depends on the strain of the system. This was determined by measuring the conductivity of strained $\text{LaAlO}_3/\text{SrTiO}_3$ bilayers for different thickness of the LaAlO_3 layer. As shown in Figure 4.1, LaAlO_3 overlayer thickness was changed from 1 to 30 unit cells while the thickness of SrTiO_3 template on NGO, LSAT, DSO, GSO substrates was fixed at 50 unit cells. The critical thickness of LaAlO_3 on Ti-terminated (001) SrTiO_3 bulk single crystal and on quasi-single-crystal (001) SrTiO_3 templates on silicon [127] was checked as a reference.

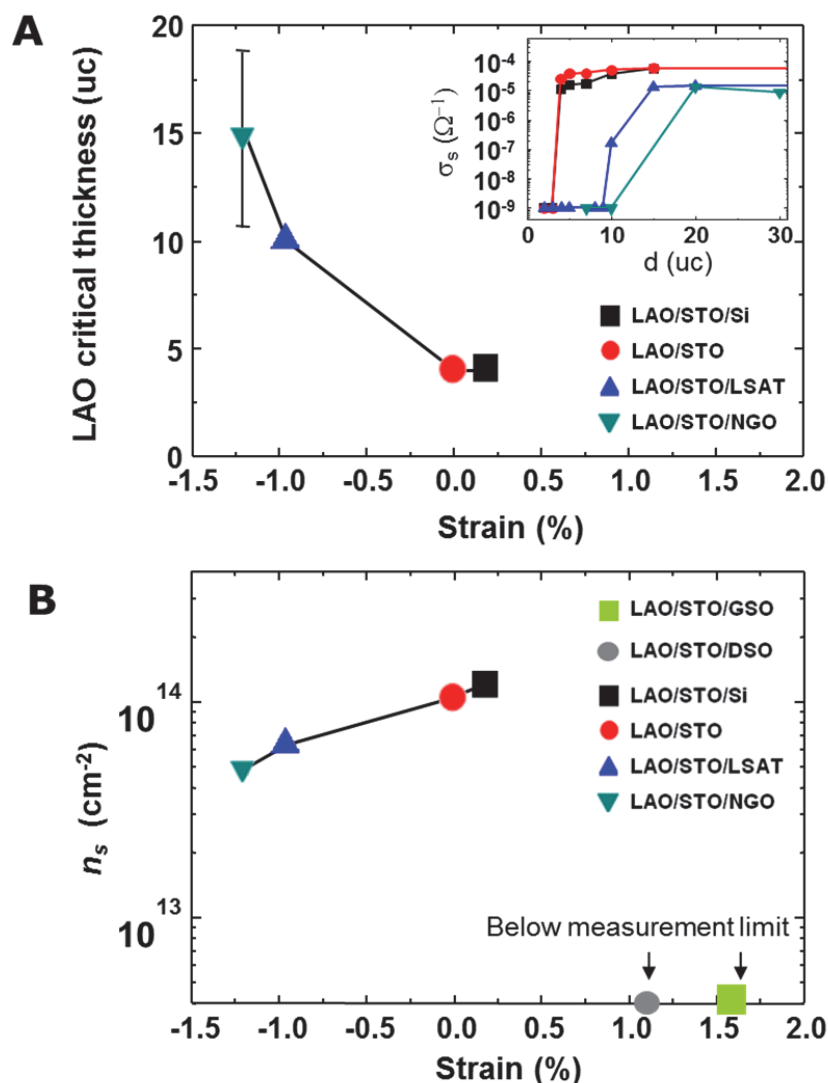


Figure 4.2 Effect of strain on 2DEG. (A) Critical thickness of LaAlO_3 under bi-axial strain. While all others samples have a 50 unit cell-thick SrTiO_3 layer, sample LAO/STO/Si has 100nm-thick STO and is the nominally unstrained STO layer on silicon. The conductivity versus thickness of LaAlO_3 in the LAO/STO interface on various substrates is given in the inset. (B) Room-temperature carrier concentrations at the LAO/STO interface under various biaxial strains. The carrier concentrations in tensile strain state were above our measurement limit.

In case of the two samples with unstrained SrTiO₃ layers (LaAlO₃ on bulk single crystal SrTiO₃ substrate and LaAlO₃ on relaxed SrTiO₃ templates on silicon), the critical thickness was in agreement with that previously reported, i.e. 4 unit cells. However, in the compressive strain states, (SrTiO₃ templates on LSAT and NGO), the critical thickness of LaAlO₃ increased to 10 unit cells and 15 unit cells, respectively, as shown in Figure 4.2 A. In all the cases, the conductivity saturate above the critical thickness of the LaAlO₃ overlayer. However, unlike the non-strained state, the conductivity versus thickness of LaAlO₃ had a gradual rather than an abrupt change at the critical thickness. For instance, in case of LaAlO₃/SrTiO₃/LSAT measurable conductivity was detected at 10 unit cells LaAlO₃ thickness, but it did not saturate until 20 unit cells. There is, however, a clear trend of increasing LaAlO₃ critical thickness with increasing compressive biaxial in-plane strain.

Figure 4.2 B shows the carrier concentration at each strain state above the critical thickness of LaAlO₃. Similar to the critical thickness of the LaAlO₃ layer, nearly the same carrier concentration was found at both near-zero strain states, LaAlO₃ on SrTiO₃ bulk single crystal and LaAlO₃ on quasi-single crystal (001) SrTiO₃ template on silicon. The saturation carrier concentration (above the critical thickness) decreased with increasing compressive strain. Although LaAlO₃/SrTiO₃ interfaces on DSO and GSO were grown and treated in the same manner, the interfaces were not conducting within our measurement limit at any thickness of LaAlO₃ overlayer in these tensile-strained

films.

The above experimental results indicate that compressively strained SrTiO₃ preserves the 2DEG, but with decreased interfacial carrier concentration. The origin of this behavior is the main subject of our theoretical investigation which is described in the next section 4.3. For the case of tensile strain in the STO layer, the experiments indicate that there is no conducting 2DEG for biaxial tensile strains above 1.1%. Free-standing SrTiO₃ has been predicted at zero temperature to develop an in-plane polarization in the (110) direction under biaxial tensile strain. Experiment suggests that, at room temperature, relaxor behavior, with nanoscale polar regions that can be aligned in an electric field, occurs in many tensile strained SrTiO₃ samples. Stabilization of a uniform in-plane polarization by the LaAlO₃ layer does not seem likely. If such nanoscale regions near to the interface were present in our samples, bound charge at polarization discontinuities between random nanopolar regions would tend to be locally screened by carriers at the 2DEG interface. This would lead to localization of these carriers, preventing us from observing conduction in these samples.

4.3 Theoretical studies

The physical origin of the experimentally observed changes of 2DEG properties under compressive strain are qualitatively explained in Figure 4.3. In the unstrained system, positively charged (LaO)⁺ atomic layers and negatively charged (AlO₂)⁻ atomic layers create an average polarization whose positive bound charge resides at the

interface, as shown schematically in the left panel of Figure 4.3 (a). This polarization charge is responsible for the intrinsic electric field E_0 in LaAlO_3 (shown by arrow in Figure 4.3 (a)) resulting in an electric potential difference between the LaAlO_3 surface and the $\text{LaAlO}_3/\text{SrTiO}_3$ interface that increases with LaAlO_3 layer thickness. Above the LaAlO_3 critical thickness, charge is transferred to the $\text{LaAlO}_3/\text{SrTiO}_3$ interface (shown by a blue filling) to avoid this polarization catastrophe.

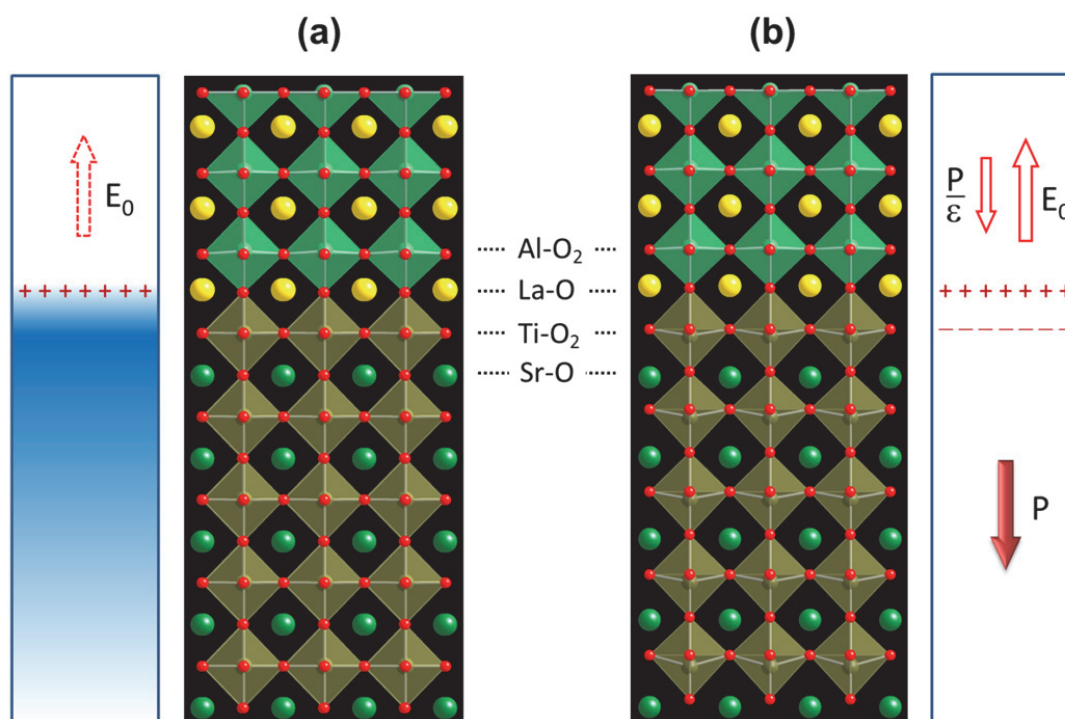


Figure 4.3 The calculated atomic structure of unstrained (A) and compressively strained (B) $\text{LaAlO}_3(3 \text{ unit cell.})/\text{SrTiO}_3$ system. In Figure B Ti-O and Sr-O displacements are amplified by a factor of eight as compared to the calculated results for visual comprehension. The left and right panels show schematically the 2DEG formation and

the effect of the polarization P in the strained SrTiO_3 on the 2DEG as described in text.

The compressively strained SrTiO_3 layer contains polar displacements of the Ti^{4+} ions with respect to the O^{2-} ions, shown in Figure 4.3 (b) for the case of uniform polarization. These displacements are responsible for a polarization P pointed away from the interface (indicated by an arrow at the bottom of the left panel of Figure 4.3 (b)). The polarization orientation is determined by the presence of the LAO layer and is likely not switchable. The polarization produces a negative bound charge at the $\text{LaAlO}_3/\text{SrTiO}_3$ interface (indicated in the left panel of Figure 4.3 (b)) that creates an additional electric field in LaAlO_3 equal to P/ϵ , where ϵ is the dielectric constant of LaAlO_3 , that opposes the intrinsic electric field E_0 . The presence of polarization in the compressively strained SrTiO_3 layer reduces the total electric field in LaAlO_3 and hence enhances the critical thickness necessary to create a 2DEG at the $\text{LaAlO}_3/\text{SrTiO}_3$ interface due to the polarization catastrophe effect. Above this critical thickness, the mobile interfacial carrier concentration would be then reduced by the interfacial bound charge [123, 124].

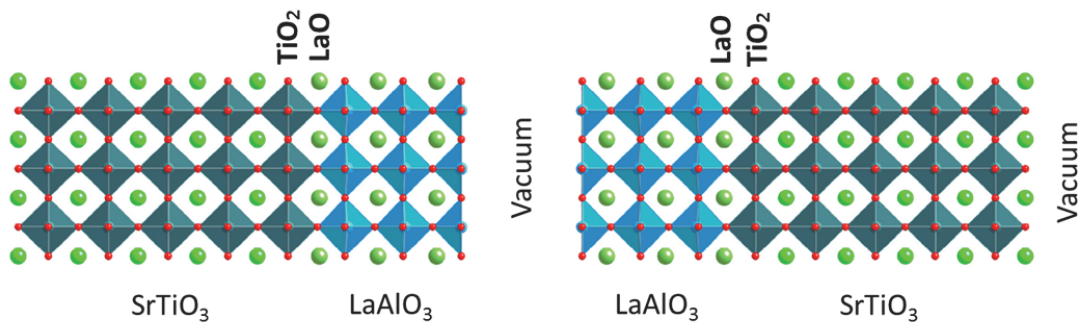


Figure 4.4 The symmetric atomic structure of $(\text{LaAlO}_3)_3/(\text{SrTiO}_3)_5$ separated by a 8 Å thick vacuum gap.

In order to quantify these effects we have performed first-principles calculations of the $\text{LaAlO}_3/\text{SrTiO}_3$ bilayer under various strain states based on methods described in chapter 2. We use density functional theory (DFT) and the local density approximation (LDA) implemented within the VASP method [79, 128]. We consider a LaO/TiO_2 -interfaced $(\text{LaAlO}_3)_n/(\text{SrTiO}_3)_m$ bilayer, where n and m are the numbers of unit cells of LaAlO_3 and SrTiO_3 respectively. The $\text{LaAlO}_3/\text{SrTiO}_3$ bilayer is placed in a $\text{LaAlO}_3/\text{SrTiO}_3/\text{vacuum}/\text{SrTiO}_3/\text{LaAlO}_3/\text{vacuum}$ supercell, as shown in Figure 4.4, where the doubled bilayer is used to avoid an unphysical electric field in vacuum which otherwise would occur due to the potential step within the LaAlO_3 layer and periodic boundary conditions of the supercell calculations. The in-plane lattice constant of the unstrained superlattice is fixed to the calculated bulk lattice constant of SrTiO_3 , *i.e.* $a = 3.871$ Å. For the strained systems the in-plane lattice constant was constrained to be by a certain percentage smaller than the bulk one. To reduce the effect of the SrTiO_3 surface on atomic structure and ionic displacements within the SrTiO_3 layer we use a boundary condition according to which the atomic positions within one unit cell on the SrTiO_3 surface are fixed to be the same as in the respectively strained bulk SrTiO_3 . The latter are computed separately for the unstrained and strained bulk SrTiO_3 . All the other atoms in the superlattices are relaxed.

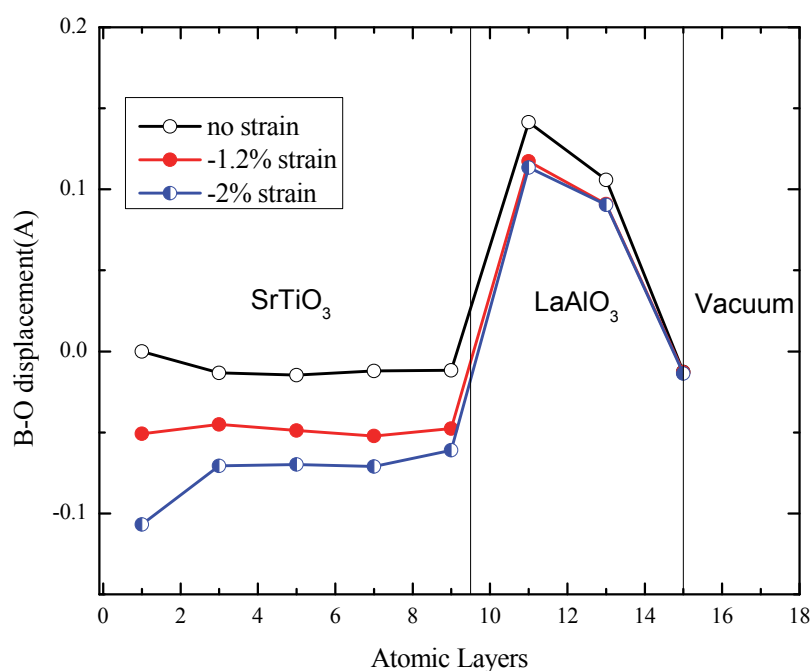


Figure 4.5 B (Ti, Al) c-site atom – oxygen (O) atom displacements in the unstrained (squares), 1.2% (circles) and 2% (half circle) compressively strained $(\text{LaAlO}_3)_3/(\text{SrTiO}_3)_5$ structure.

Figure 4.5 shows the calculated ionic displacements for the unstrained 1.2% and 2% compressively strained $(\text{LaAlO}_3)_3/(\text{SrTiO}_3)_5$ structures. It is seen that in the unstrained case polar Ti-O displacements in the SrTiO_3 layer are very small, consistent with the previous calculations [35]. The in-plane compressive strain produces sizable ionic displacements, polarizing the SrTiO_3 layer and as the compressive strain increases the induced polarization increases. The calculation predicts that the induced polarization is oriented away from the interface and is not switchable. In the case of 1.2% compressive

strain, the magnitude of the polarization is $P \approx 0.18 \text{ C/m}^2$, as found from the known polar displacements in the strained SrTiO₃ layer using the Berry phase method [102, 129].

The critical thickness t_c in the presence of a STO polarization can be estimated as follows:

$$t_c = \delta\mathcal{E} / eE, \quad (4.1)$$

where $\delta\mathcal{E} = e\mathcal{E}_g + (\mathcal{E}_{VBM}^{STO} - \mathcal{E}_{VBM}^{LAO})$, \mathcal{E}_g is the band gap of SrTiO₃, \mathcal{E}_{VBM}^{STO} and \mathcal{E}_{VBM}^{LAO} are the valence band maxima (VBM) of SrTiO₃ and LaAlO₃ respectively, and E is the electric field in LaAlO₃. In the derivation of t_c below, we only need to consider the situation that the free charge has not been transferred to the interface and the thickness of LaAlO₃ is less than t_c . E is reduced from the intrinsic value of E_0 due to polarization P of SrTiO₃, so that

$$E = E_0 - \frac{P}{\varepsilon_{LAO}}, \quad (4.2)$$

where ε_{LAO} is the dielectric constant of LaAlO₃. Due to the reduced electric field in LaAlO₃ in the presence of the SrTiO₃ polarization, the critical thickness is enhanced as indicated in Eq. (4.1). The intrinsic electric field E_0 can be estimated from the experimentally measured critical thickness $t_c^0 = 4$ unit cell. for the unstrained system. Taking into account the experimental band gap of STO $\mathcal{E}_g = 3.2 \text{ eV}$ and the CBM offset between SrTiO₃ and LaAlO₃ $\mathcal{E}_{VBM}^{STO} - \mathcal{E}_{VBM}^{LAO} = 0.35 \text{ eV}$ [130], we find that $\delta\mathcal{E} = 3.55 \text{ eV}$. Using the relationship

$$\delta\mathcal{E} = eE_0 t_c^0, \quad (4.3)$$

we obtain that $E_0 \approx 0.23\text{V}/\text{\AA}$, which is consistent with our first-principles calculation predicting $E_0 \approx 0.22\text{V}/\text{\AA}$, and calculations by others [35, 42, 52]. Using Eqs. (4.1), (4.2) and (4.3) we obtain

$$t_c = \frac{t_c^0}{1 - \frac{P}{\varepsilon_{LAO} E_0}}. \quad (4.4)$$

For the system under strain, when the thickness of LaAlO_3 is above the critical thickness, there is a transferred charge at the interface and the charge density σ is estimated as shown below. At first, it is necessary to derive the transferred charge density σ_0 for the system without strain similar to Ref. [52]. When the LaAlO_3 thickness t is above the critical t_c^0 , a free surface charge σ_0 is transferred to the $\text{LaAlO}_3/\text{SrTiO}_3$ interface. The electric field inside LaAlO_3 is then

$$E = E_0 - \frac{\sigma_0}{\varepsilon_{LAO}}. \quad (4.5)$$

The VBM of LaAlO_3 is aligned with the CBM of SrTiO_3 . Therefore

$$etE = eE_0 t_c^0 = \delta\mathcal{E}. \quad (4.6)$$

It follows from Eqs. (4.5) and (4.6) that

$$\sigma_0 = \varepsilon_{LAO} E_0 \left(1 - \frac{t_c^0}{t} \right), \quad (4.7)$$

i.e. the transferred charge density increases with the LaAlO_3 thickness which is consistent with the experimental observation, as shown in the inset of Figure 4.2 A.

Similarly, when the system is under strain, above the critical thickness t_c , electric field inside LaAlO₃ is

$$E = E_0 - \frac{\sigma_0}{\epsilon_{LAO}} - \frac{P}{\epsilon_{LAO}}. \quad (4.8)$$

Using Eqs. (4.4), (4.6) and (4.8), the transferred charge for strained system is then obtained as follows

$$\sigma = \epsilon_{LAO} E_0 \left(\frac{t_c^0}{t_c} - \frac{t_c^0}{t} \right). \quad (4.9)$$

It is clear that when there is no strain, i.e. $t_c = t_c^0$, Eq. (4.9) is identical to Eq. (7), as expected. As the strain increases, due to the increased polarization in SrTiO₃ (see Figure 4.5) we expect a larger critical thickness t_c , as indicated both by Eq (4.4) and by the experimental data shown in Figure 4.2 A. Eq. (4.9) predicts that for the same thickness t of LaAlO₃, as the strain increases, the transferred charge decreases as a result of the increased critical thickness. This prediction again agrees well with the experimental results shown in Figure 4.2 B.

Using the calculated polarization value of $P \approx 0.18 \text{ C/m}^2$ for 1.2% compressive strain in the STO layer, and the calculated electric fields in the LaAlO₃ and SrTiO₃ layers in the strained LaAlO₃/SrTiO₃ system, we estimate the dielectric constant of the 1.2% compressively strained LaAlO₃ to be $\epsilon_{LAO} \approx 18\epsilon_0$. This value is consistent with that obtained from the induced polarization of 0.34 C/m^2 in the LaAlO₃ layer, as is estimated from the calculated ionic displacements using the Berry phase method. (We note that the

estimated value of the dielectric constant of the unstrained LaAlO_3 is $\epsilon_{\text{LAO}} \approx 24\epsilon_0$ which is consistent with the previously found result [38]). Using Eq. (4.4) and the dielectric constant $\epsilon_{\text{LAO}} \approx 18\epsilon_0$ we obtain $t_c \approx 9$ unit cell. This value is higher than the critical thickness (4 unit cell.) for the unstrained system, and is consistent with the experimental result for the 1.2% strained $\text{LaAlO}_3/\text{SrTiO}_3$ structure. In the experimental situation it is expected that the surface polarization charge in LaAlO_3 is screened by adsorbents, and that the bottom polarization charge in the strained SrTiO_3 is screened by defects. In the structural model used in our DFT calculation the SrTiO_3 polarization is screened by charge transferred to the SrTiO_3 surface.

Our computations predict that at the LAO critical thickness of 3 unit cells, when the unstrained system becomes conducting, the 2% compressive strain expels the electron charge from the interface making the interface insulating. This results is seen from Figure 4.6, which shows the density of states (DOS) at the TiO_2 layer located at the interface for the unstrained, and the -2% strained $(\text{LaAlO}_3)_3/(\text{SrTiO}_3)_5$ structure. It is seen that the compressive strain eliminates the free electron charge at the unstrained interface (filled shadow under the red curve) making the system insulating.

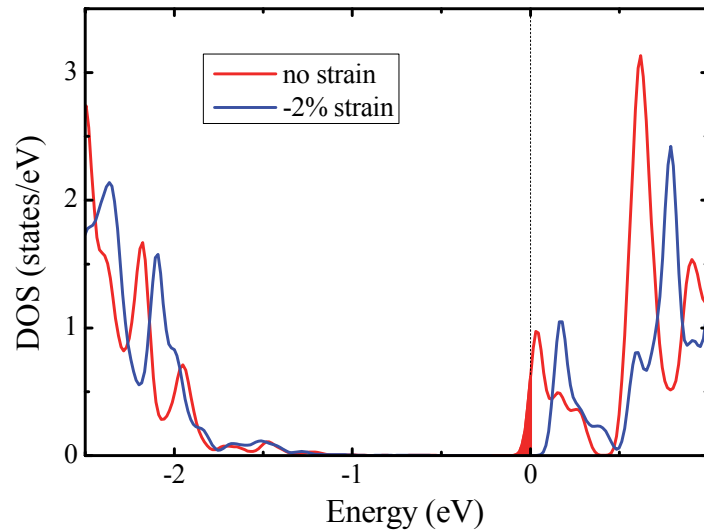


Figure 4.6: Density of electronic states at the TiO_2 monolayer located at the interface of the unstrained, and the -2% strained $(\text{LaAlO}_3)_3/(\text{SrTiO}_3)_5$ structure. The vertical line indicates the position of the Fermi energy. The filled area under the curve for the unstrained system indicates the free electron charge responsible for the formation of the 2DEG. The strain eliminates this charge making the system insulating.

4.4 Summary

We have demonstrated that properties of the 2DEG formed at the $\text{LaAlO}_3/\text{SrTiO}_3$ interface can be controlled by epitaxial strain. Both the critical thickness of the LaAlO_3 overlayer required to generate the 2DEG and the carrier concentration of the 2DEG depend on the strain of the SrTiO_3 layer. Compressive strain increases the critical thickness and decreases the saturated carrier concentration. Our DFT calculations indicate that a strain-induced polarization stabilized by the LaAlO_3 overlayer is

responsible for these changes. Changes in critical thickness and carrier concentration estimated from the DFT calculations are in agreement with the experimental data.

The dependence of the 2DEG properties at the $\text{LaAlO}_3/\text{SrTiO}_3$ interface on the strain state opens a new correlation between strain-induced polarization and the electrical properties of oxide interfaces. We believe that such strain engineering can be very useful for oxide 2DEG device applications, and the relation between strain and 2DEG properties provides a new tool in the manipulation of oxide interfacial 2DEGs.

Chapter 5 *Spin-polarized 2DEG*

Making 2DEG gas spin-polarized is a very exciting prospect for spintronics applications, where the involvement of the spin degree of freedom broadens the spectrum of potential applications. Here, using first-principles calculations, we predict the existence of a spin-polarized two-dimensional electron gas (2DEG) at the LaO/EuO interface in a LaAlO₃/EuO (001) heterostructure. We show that this polar interface favors electron doping into the Eu-5*d* conduction bands resulting in a 2DEG formed at the interface. Due to the exchange splitting of the Eu-5*d* states, the 2DEG is spin-polarized. The predicted mechanism for the formation of a spin-polarized 2DEG at the interface between polar and ferromagnetic insulators may provide a robust magnetism of the 2DEG, which is interesting for spintronics applications.

5.1 Introduction

5.1.1 Overview of spin-polarized 2DEG

Recently it was found that at ultra-low temperatures the 2DEG occurring at the interface between the non-magnetic LaAlO₃ and SrTiO₃ materials may become magnetic [48]. This behavior was attributed to the exchange splitting of the induced electrons in the Ti-3*d* conduction band, which is corroborated by spin-polarized first-principles calculations of LaAlO₃/SrTiO₃ [33, 36], as well as LaTiO₃/SrTiO₃ interfaces [31]. It was also proposed that it may be possible to create a fully spin-polarized 2DEG by

replacing one monolayer of SrO by LaO in SrMnO₃ [131]. The magnetic ground state of SrMnO₃ is G-type antiferromagnetic (AFM) with Mn⁴⁺ ($t_{2g}^3 e_g^0$), while the ground state of LaMnO₃ is A-type antiferromagnetic with Mn³⁺ ($t_{2g}^3 e_g^1$). The 2DEG is introduced by the extra charge of the LaO⁺ layer at interface, where the 2DEG occupies the Mn- e_g states near the interface. Zener double exchange helps to stabilize the ferromagnetic structure of Mn at the interface, while further layers away from interface retain antiferromagnetic configuration, and thus a spin-polarized 2DEG is created [131].

Here, we pursue a different route to achieve a spin-polarized two-dimensional electron gas, by employing a ferromagnetic insulator as one of the constituents in the oxide heterostructure. Spin-polarized properties of the 2DEG are, in this case, expected to be inherited from the ferromagnetism of the oxide, and consequently, this approach may lead to a more robust magnetism in the 2DEG, which is beneficial for applications. To illustrate the idea we consider EuO as a representative ferromagnetic insulator in conjunction with LaAlO₃ to form a spin-polarized 2DEG at the LaAlO₃/EuO(001) interface.

5.1.2 Ferromagnetic insulator EuO

EuO has a rocksalt crystal structure (Figure 5.1) and is a ferromagnetic insulator (semiconductor) with a bulk Curie temperature (T_C) of 69 K. The divalent Eu ion in EuO has a half filled 4*f* shell leading to the $^8S_{7/2}$ ground state and the magnetic moment of $7\mu_B$ per Eu ion. The Heisenberg exchange coupling between the localized 4*f* electrons causes

the ferromagnetic ordering in EuO below T_c . The half-filled $4f$ band is separated from the $5d-6s$ conduction bands by a bandgap of 1.12 eV at room temperature [132]. In the ferromagnetic state of EuO, the direct exchange interaction between the localized $4f$ moments and the delocalized $5d$ conduction band states leads to the spin splitting of the latter. The spin splitting of the $5d$ states as large as 0.6 eV produces the full spin polarization near the bottom of conduction band [133]. These features can also be seen from the electronic density of states of bulk EuO shown in Figure 5.2, which are obtained by the first-principles calculation with general description in the next section.

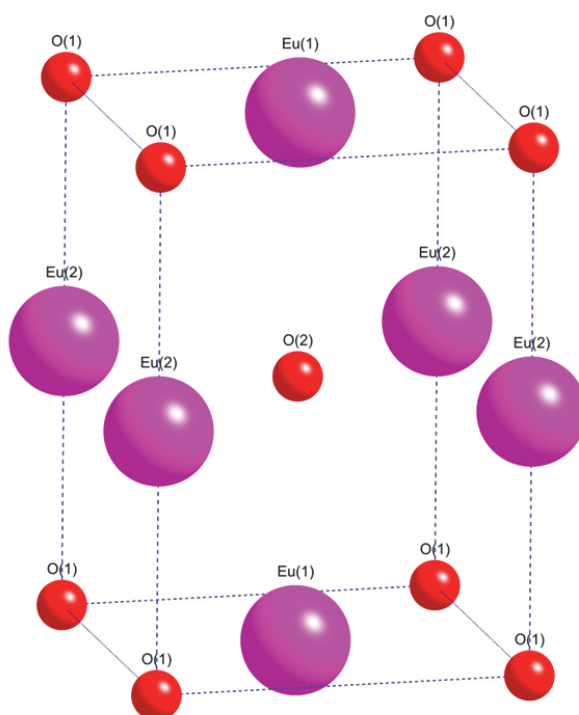


Figure 5.1 Rocksalt crystal structure of EuO.

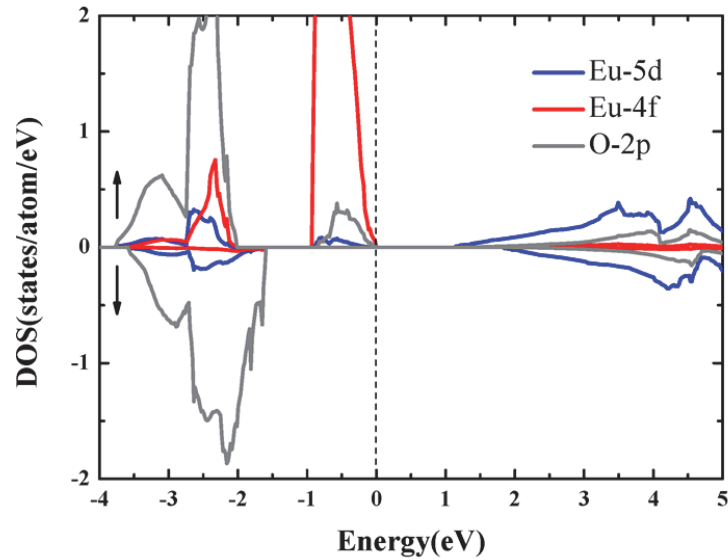


Figure 5.2 The density of states (DOS) of bulk EuO for different orbitals. The positive and negative values show the DOS for the spin-up and spin-down electrons, respectively. Fermi energy is located at zero, indicated by the dashed line.

The large splitting between spin-up and spin-down states at the bottom of the EuO conduction band allows creating a highly spin-polarized electron gas by appropriate n-doping of the material. Experimentally it was found that the transport spin polarization of conduction electrons in EuO doped with La exceeds 90% [134]. In particular, recently it has been observed that in La-doped EuO, the Curie temperature can be as high as 200 K due to the enhanced coupling between Eu 4f states and itinerant electrons in Eu 5d states [135].

5.2 Spin-polarized 2DEG in EuO based heterostructures

5.2.1 LaAlO₃/EuO

Here we demonstrate that the electron doping may be achieved locally at the LaAlO₃/EuO(001) interface to create a spin-polarized 2DEG. The mechanism responsible for the 2DEG formation is similar to that known for the LaAlO₃/SrTiO₃ interface [53]. LaAlO₃ consists of alternating (LaO)⁺ and (AlO₂)⁻ charged planes, whereas EuO consists of (EuO)⁰ neutral planes. When LaAlO₃ is deposited on top of EuO the divergence in the electrostatic potential can be avoided by transferring half an electron per two-dimensional unit cell to the LaO/EuO terminated interface. A charge transfer to the interface also occurs if the LaAlO₃ layer is non-stoichiometric and terminated with the LaO monolayers on both sides. In this case an “extra” electron is introduced into the system due to the uncompensated ionic charge on the additional (LaO)⁺ monolayer. This electronic charge is accommodated by partially occupying conduction band states near the interface, producing a 2DEG. In ferromagnetic EuO the conduction band is formed by exchange split Eu-5*d* states and so the 2DEG is expected to be spin-polarized. Thus, by forming the LaAlO₃/EuO(001) interface, one can achieve a spin-polarized 2DEG below the Curie temperature of EuO or for even higher temperature.

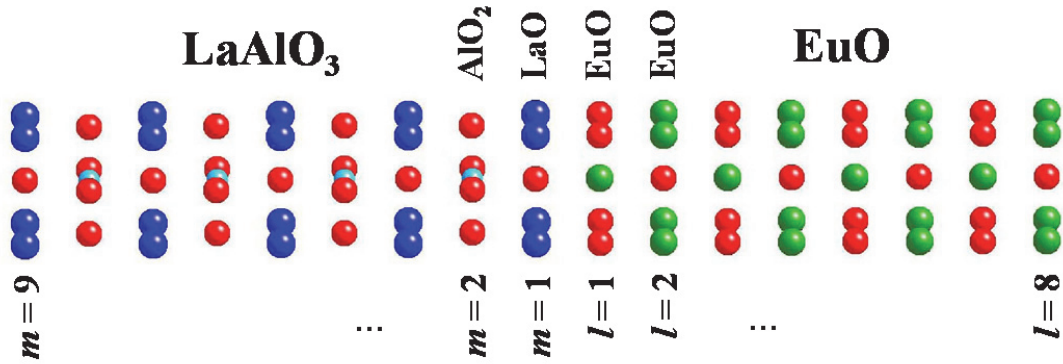


Figure 5.3 Atomic structure of the LaO/EuO interface in the $(\text{LaAlO}_3)_{8.5}/(\text{EuO})_{15}$ (001) superlattice containing 8.5 unit cells of LaAlO_3 and 15 monolayers of EuO within the supercell. Indices l and m denote atomic monolayers and are increasing with separation from the interface. $l = 8$ in EuO and $m = 9$ in LaAlO_3 correspond the middle of the respective layers.

To quantitatively demonstrate our prediction we perform first-principles calculations of the electronic structure of the $\text{LaAlO}_3/\text{EuO}$ (001) interface within the framework of density functional theory (DFT). Self-consistent calculations are performed using a plane wave basis set limited by a cutoff energy of 520eV and the $6 \times 6 \times 1$ Monkhorst-Pack k-point mesh [80] with energy converged to 10^{-5} eV/cell. Atomic relaxations are performed until the Hellmann-Feynman forces on atoms have become less than 30 meV/Å.

On-site correlations for the $\text{Eu-}4f$ orbitals are included within the local density approximation (LDA)+ U approach [73]. The value of $J = 0.6$ eV is calculated using the

constrained occupation method [136] by considering the $4f$ states as an open-core shell and finding the LDA energy difference between the $4f^{\uparrow 7}4f^{\downarrow 0}$ and $4f^{\uparrow 6}4f^{\downarrow 1}$ configurations [137]. We find, however, that the value of $U = 5.3$ eV obtained by this method appears to be too small and leads to the $4f$ states being too shallow with respect to the conduction band of EuO. This discrepancy is due to the underestimation by DFT of the intrinsic insulating gap between the O- $2p$ and Gd- $5d$ states. Therefore, we adjusted the value of U empirically and found that $U = 7.5$ eV results in a very reasonable agreement with experiment. In particular, $U + 6J = 11.1$ eV agrees well with the occupied-unoccupied $4f$ state splitting observed in photoemission-inverse photoemission for Eu metal; the optical band gap at the X point of 0.94 eV is consistent with the zero-temperature experimental value of approximately 0.95 eV [138]; and the lattice constant $a = 5.188$ Å agrees with the experimental value of $a = 5.144$ Å. The exchange splitting of the Eu $5d$ orbitals is found to be $\Delta_d = 0.75$ eV. Since the La- $4f$ bands lie at higher energy than that predicted by LDA, we impose $U = 11$ eV and $J = 0.68$ eV on these orbitals to avoid their spurious mixing with the conduction bands of LaAlO₃.

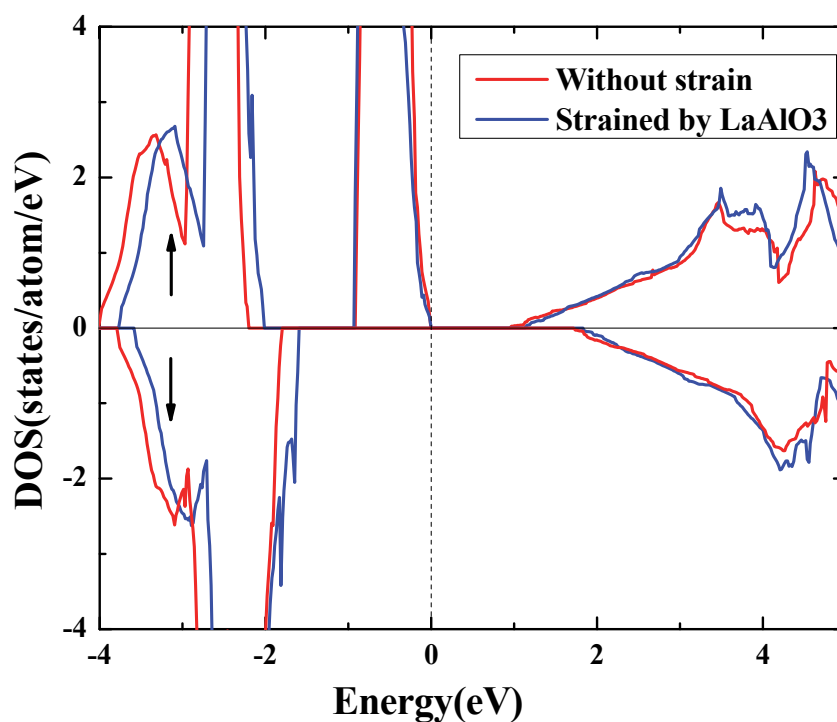


Figure 5.4 The density of state (DOS) of bulk EuO under strain by LaAlO₃ (blue) and without strain (red).

We consider the LaO/EuO terminated interface of a (LaAlO₃)_{8.5}/(EuO)₁₅ superlattice (i.e., the interface containing 8.5 unit cells of LaAlO₃ and 15 monolayers of EuO within the supercell) stacked in the [001] direction, as shown in Figure 5.3. We use periodic boundary conditions and impose mirror plane symmetry at the central EuO monolayer. The in-plane lattice constant of the superlattice is fixed to the calculated lattice constant of cubic LaAlO₃, $a = 3.81 \text{ \AA}$, which is in good agreement with the experimental value $a = 3.79 \text{ \AA}$. Under this constraint EuO exhibits tetragonal distortion of $c/a = 0.947$. This

distortion does not change significantly the electronic structure of bulk EuO in the interested energy region as shown in Figure 5.4. In particular, the band gap of EuO becomes $E_g = 1.15$ eV and the exchange splitting of the d orbitals becomes $\Delta_d = 0.66$ eV. The out-of-plane lattice constant of the supercell is determined by optimizing the interface separation distance between the LaAlO₃ and EuO sub-units keeping their bulk lattice constants fixed. Then, we fix the supercell dimensions and relax the atomic positions of all the atoms in the (LaAlO₃)_{8.5}/(EuO)₁₅ superlattice.

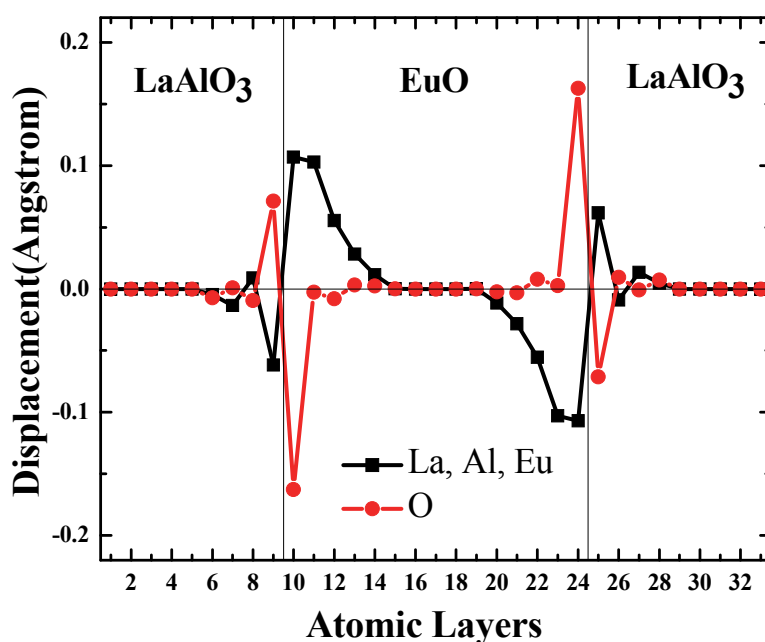


Figure 5.5 Atomic displacements in the (LaAlO₃)_{8.5}/(EuO)₁₅ (001) superlattice with respect to the atomic “bulk” positions. The latter are determined by fixing the in-plane lattice constant and optimizing the interlayer distance, as described in text. The vertical

lines indicate interfaces.

Figure 5.5 shows the calculated atomic displacements within the $(\text{LaAlO}_3)_{8.5}/(\text{EuO})_{15}$ supercell. It is seen that the largest structural relaxations occur in the vicinity of the LaO/EuO interfaces and involve a polar distortion in which the negatively charged O anions are displaced with respect to the positively charged cations (either La, Al or Eu). When moving away from the interface, the magnitude of the displacements reduces and the La-La and Eu-Eu distances revert to constant values close to those in the bulk.

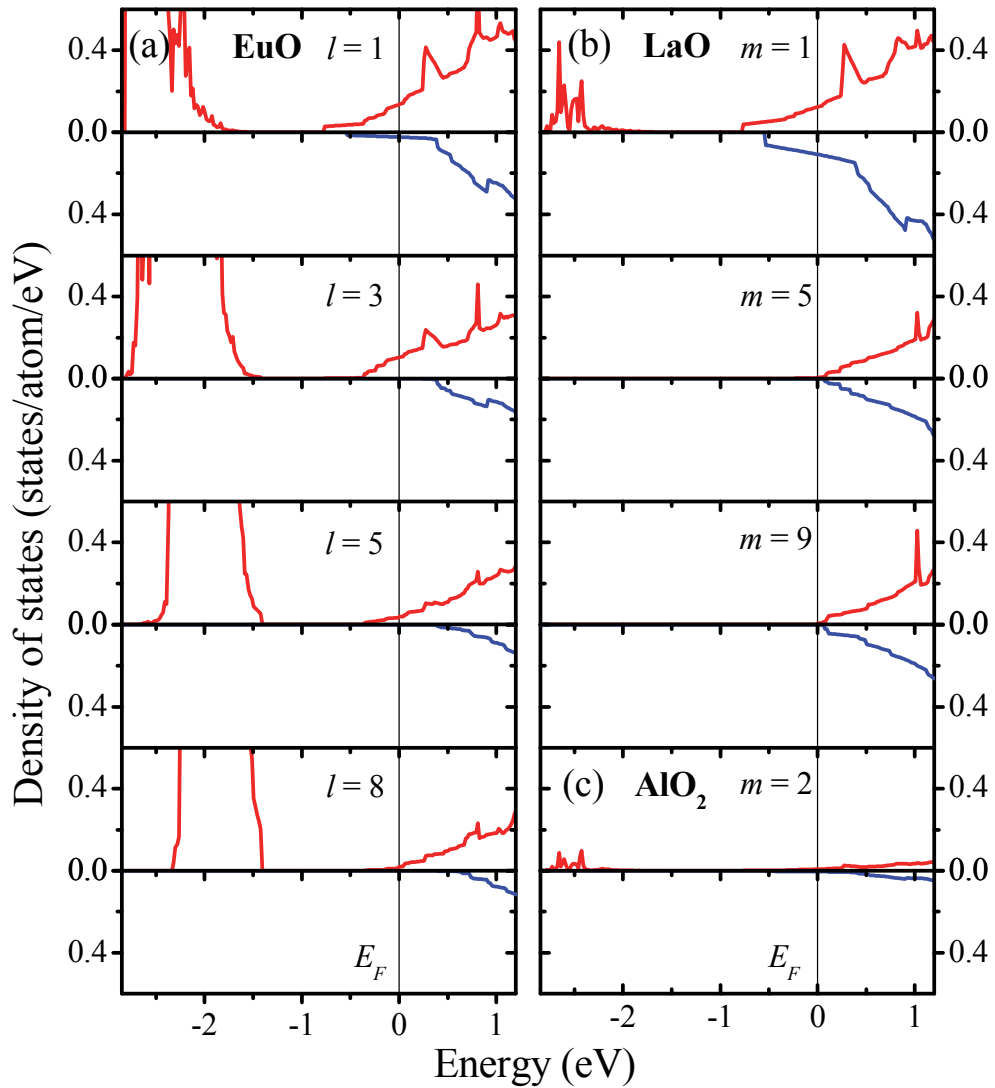


Figure 5.6: Layer- and spin-resolved density of states (DOS) on EuO (a), LaO (b) and AlO₂ (c) monolayers located at different planes l and m away from the LaO/EuO interface (as labeled in Figure 5.3). Top (bottom) panels show the majority(minority)-spin. In panel (a) the majority-spin states at energies below -1 eV are the occupied Eu-4*f* states. The vertical lines denote the Fermi energy (E_F).

Figure 5.6 shows the layer resolved majority- and minority-spin densities of states

(DOS) on the EuO (a) and LaO (b) monolayers located at different planes l and m away from the LaO/EuO interface (see labeling in Figure 5.3). It is seen that there are occupied states below the Fermi energy on both the LaO and EuO monolayers near the interface, which indicate the formation of the n-type 2DEG at the LaO/EuO interface. This 2DEG comes from the occupation of the conduction band. Although it is pointed out that metallic phase could exist at surface of EuO [139], here the DOS near the CBM varies smoothly which distinguishes itself from the sharp surface DOS. The DOS on AlO₂ monolayers (Figure 5.6c) is negligible near the Fermi energy compared to that on the LaO and EuO monolayers. Far away from the interface, the DOS at the Fermi energy on both the LaO and EuO monolayers drops to zero reflecting the insulating nature of bulk LaAlO₃ and EuO.

The central result of our calculation is the formation of spin-polarized 2DEG at the LaAlO₃/EuO (001) interface. This fact is evident from Figure 5.6a indicating a significant difference in the occupation of the EuO majority- and minority-spin conduction bands near the interface. This is the direct consequence of the exchange splitting of the conduction $5d$ states in EuO and the occupation of these states due to the electron doping of the interface. As seen from Figure 5.6a, starting from the second EuO monolayer away from the LaO/EuO interface only majority-spin states are occupied in the conduction band of EuO indicating tendency to half-metallicity known for the n-doped bulk EuO [133]. Figures 5.6b and 5.6c also indicate the spin splitting of the conduction bands of LaAlO₃ near the interface, which is the result of the exchange

interaction between the Eu-4*f* and La-5*d* states across the interface.

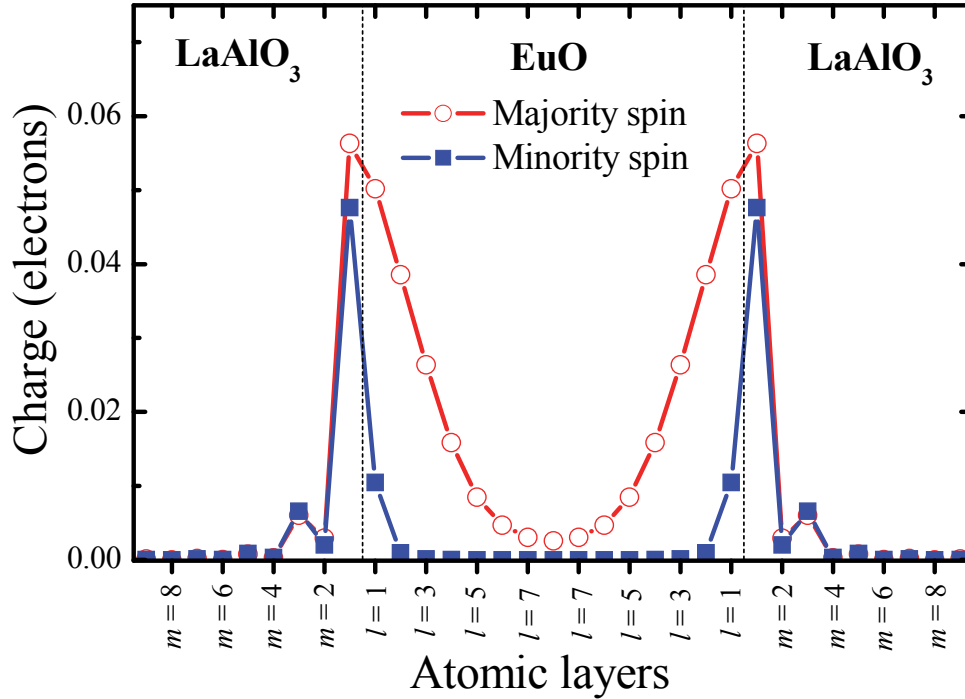


Figure 5.7 Spin-dependent charge distribution across the $(\text{LaAlO}_3)_{8.5}/(\text{EuO})_{15}$ (001) supercell. The notation for the atomic layers is the same as in Figure 5.3. The dashed lines indicate interfaces.

Similar to the case of the $\text{LaAlO}_3/\text{SrTiO}_3$ interface, where the O-2*p* valence bands of LaAlO_3 and SrTiO_3 are nearly lined up (e.g., Ref. [38]), we find for the $\text{LaAlO}_3/\text{EuO}$ interface that the top of the O-2*p* valence band lies at -3.0eV in EuO and at about -3.6eV in LaAlO_3 with respect to the Fermi energy. Due to a larger energy gap between the O-*p* valence bands and the conduction bands in LaAlO_3 than in EuO (the calculated values are 3.7eV and 2.7eV , respectively, and the experimental values are 5.6eV and

4.4eV [140], respectively), the conduction band minimum lies lower in EuO than in LaAlO₃ resulting in the charge accumulating mainly within the EuO layer. This is evident from Figure 5.7, which shows the distribution of the spin-dependent charge across the unit cell. The latter is calculated by integrating the spin- and layer-resolved DOS from the conduction band minimum up to the Fermi energy*. The large spin polarization of the 2DEG is seen at the EuO monolayers near the LaAlO₃/EuO interface. The estimated value of the spin polarization of the free charge density is about 50%.

We note that our calculation is performed for the non-stoichiometric LaAlO₃ layer which is assumed to be LaO terminated on both sides. Similar to the previous theoretical studies [29, 30], in this geometry an “extra” electron is introduced in the system due to the uncompensated ionic charge on the additional (LaO)⁺ monolayer. For a stoichiometric LaAlO₃ layer deposited on top of EuO, it is demonstrated that a 2DEG is formed at the interface due to the electronic reconstruction resulting from the charge transfer to the interface that eliminates the increasing electrostatic potential in LaAlO₃ [141].

Due to the enhanced coupling between nearest *4f* Eu by itinerant electron, the Curie temperature of this spin-polarized 2DEG at interface of stoichiometric EuO/LaAlO₃ can be as high as 105K, as predicted in Ref. [141]. For the same reason, we can expect an enhanced Curie temperature in our non-stoichiometric systems.

* The local charges are evaluated within the Wigner-Seitz spheres, as specified by VASP.

5.2.2 EuO/LaO/EuO

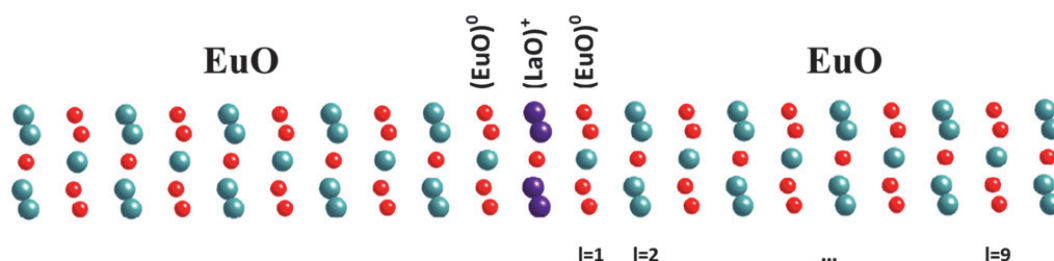


Figure 5.8 Atomic structure of $\text{LaO}/(\text{EuO})_{19}$ (001) superlattice containing one monolayer LaO and 19 monolayers of EuO. Indices l denote atomic monolayers and are increasing with separation from the interface layer LaO.

Due to the experimental difficulties of growing both EuO and LaAlO_3 in the same environment, in addition to the heterostructure studied above, here we investigate another heterostructure $\text{EuO}/\text{LaO}/\text{EuO}$ (001) at the interface of which electron doping may be achieved locally and spin-polarized. This structure could be grown experimentally by inserting one layer of LaO in the growing process of bulk EuO. The considered $\text{LaO}/(\text{EuO})_{19}$ superlattice (i.e., one monolayer LaO and 19 monolayers of EuO) is stacked in the [001] direction, as shown in Figure 5.8. We use periodic boundary conditions and impose mirror plane symmetry at the central EuO monolayer. The lattice constants used are the same as those used for $\text{LaAlO}_3/\text{EuO}$. The optimization of the superlattice spacing follows the same procedure for $\text{LaAlO}_3/\text{EuO}$. Figure 5.9 shows the calculated atomic displacements within the $\text{LaO}/(\text{EuO})_{19}$ (001) superlattice. A clear Eu-O

relative displacement occurs near the interface and reduces when moving from the interface. The associated dipole distortion pointing away from the $(\text{LaO})^+$ ionic layer, which is the same direction of the electric field produced within this layer. This distortion is the result of the ionic screening effect in addition to the possible electronic screening. This distortion makes the dielectric constant of EuO in this superstructure very different from the bulk value, and thus significantly affects the wedge-shaped electric potential, and finally strongly influences the carrier distribution near the interface [29].

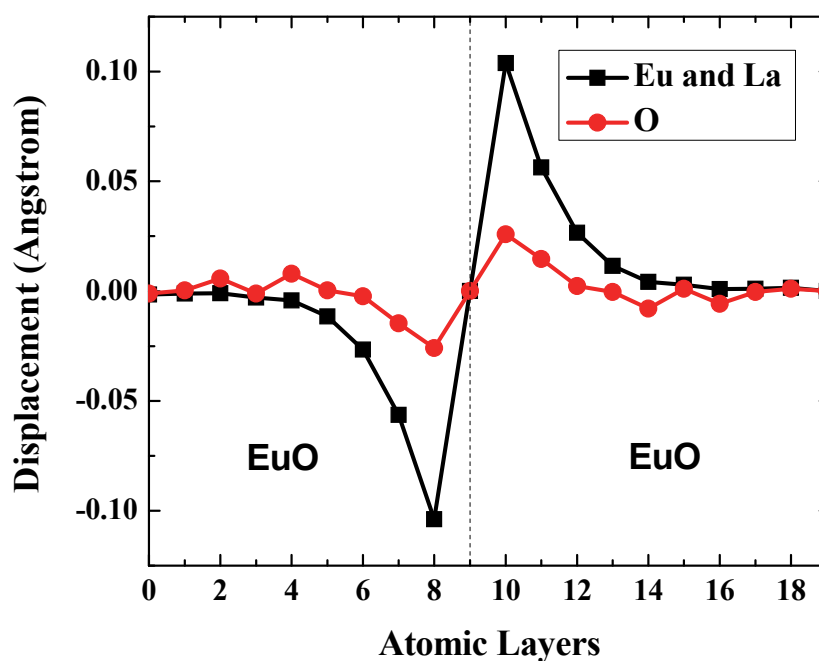


Figure 5.9 Atomic displacements in the $\text{LaO}/(\text{EuO})_{19}$ (001) superlattice with respect to the atomic “bulk” positions. The latter are determined by fixing the in-plane lattice constant and optimizing the interlayer distance, as described in the text. The vertical

dashed line indicates the interface layer LaO.

By examining layer resolved density of state in the our calculations, the electron doping is found locally near the interface of EuO/LaO/EuO(001) structure. Using the same approach of calculating the spin-dependent charge distribution in Figure 5.7, we demonstrate in Figure 5.10 that a spin-polarized 2DEG is formed in both LaO and EuO layers near the interface of LaO/EuO with a decay length smaller than that in LaAlO₃/EuO. The relatively smaller spin polarization in this superlattice compared with that in LaAlO₃/EuO is due to the large occupation of small spin-polarized states in the LaO layer.

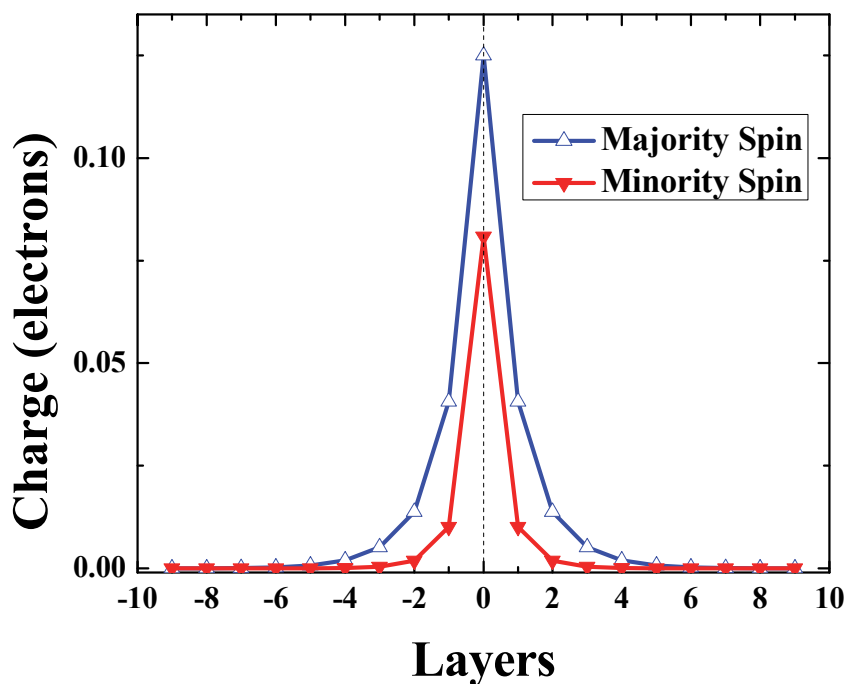


Figure 5.10 Spin-dependent charge distribution across the LaO/(EuO)₁₉ (001) supercell. The notation for the atomic layers is the same as in Figure 5.8. The dashed lines indicate the LaO interface layer.

5.3 Summary

In summary, based on first-principles calculations we have predicted the possibility to create a spin-polarized 2DEG at the LaO/EuO interface in the LaAlO₃/EuO (001) heterostructure. We demonstrated that this polar interface favors electron doping into the Eu-5*d* conduction bands rendering a 2DEG formed at the interface. Due to the exchange splitting of the Eu-5*d* states the 2DEG becomes spin-polarized. The predicted mechanism for the formation of a spin-polarized 2DEG at the interface between polar and ferromagnetic insulators may lead to a robust magnetism of a 2DEG which is interesting for spintronics applications.

References

- [1] M. Dawber, K. M. Rabe, and J. F. Scott, *Physics of thin-film ferroelectric oxides*, *Reviews of Modern Physics* **77**, 1083 (2005).
- [2] Y. Tokura, and H. Y. Hwang, *Complex oxides on fire*, *Nat Mater* **7**, 694 (2008).
- [3] M. Bibes, J. E. Villegas, and A. Barthelemy, *Ultrathin oxide films and interfaces for electronics and spintronics*, *Advances in Physics* **60**, 5 (2011).
- [4] S. E. Lister, I. Radosavljevic Evans, J. A. K. Howard, A. Coelho, and J. S. O. Evans, *Mo₂P₄O₁₅ - the most complex oxide structure solved by single crystal methods?*, *Chemical Communications*, 2540 (2004).
- [5] S. Yuasa, T. Nagahama, A. Fukushima, Y. Suzuki, and K. Ando, *Giant room-temperature magnetoresistance in single-crystal Fe/MgO/Fe magnetic tunnel junctions*, *Nat Mater* **3**, 868 (2004).
- [6] J. F. Scott, *Applications of Modern Ferroelectrics*, *Science* **315**, 954 (2007).
- [7] M. K. Wu, J. R. Ashburn, C. J. Torng, P. H. Hor, R. L. Meng, L. Gao, Z. J. Huang, Y. Q. Wang, and C. W. Chu, *Superconductivity at 93 K in a new mixed-phase Y-Ba-Cu-O compound system at ambient pressure*, *Physical Review Letters* **58**, 908 (1987).
- [8] A. A. Demkov, A. Posadas, H. Seo, J. K. Lee, and N. Sai, *Emerging physics of oxide heterostructures*, *physica status solidi (b)*, n/a (2011).

- [9] P. Zubko, S. Gariglio, M. Gabay, P. Ghosez, and J.-M. Triscone, *Interface Physics in Complex Oxide Heterostructures*, Annual Review of Condensed Matter Physics **2**, 141 (2011).
- [10] C. W. Bark, D. A. Felker, Y. Wang, Y. Zhang, H. W. Jang, C. M. Folkman, J. W. Park, S. H. Baek, H. Zhou, D. D. Fong, X. Q. Pan, E. Y. Tsymbal, M. S. Rzchowski, and C. B. Eom, *Tailoring a two-dimensional electron gas at the $LaAlO_3/SrTiO_3$ (001) interface by epitaxial strain*, Proceedings of the National Academy of Sciences (2011).
- [11] D. Dijkkamp, T. Venkatesan, X. D. Wu, S. A. Shaheen, N. Jisrawi, Y. H. Min-Lee, W. L. McLean, and M. Croft, *Preparation of Y-Ba-Cu oxide superconductor thin films using pulsed laser evaporation from high T_c bulk material*, Applied Physics Letters **51**, 619 (1987).
- [12] D. G. Schlom, J. N. Eckstein, E. S. Hellman, S. K. Streiffer, J. J. S. Harris, M. R. Beasley, J. C. Bravman, T. H. Geballe, C. Webb, K. E. von Dessenbeck, and F. Turner, *Molecular beam epitaxy of layered Dy-Ba-Cu-O compounds*, Applied Physics Letters **53**, 1660 (1988).
- [13] G. J. H. M. Rijnders, G. Koster, D. H. A. Blank, and H. Rogalla, *In situ monitoring during pulsed laser deposition of complex oxides using reflection high energy electron diffraction under high oxygen pressure*, Applied Physics Letters **70**, 1888 (1997).

- [14] J. W. Reiner, F. J. Walker, and C. H. Ahn, *Atomically Engineered Oxide Interfaces*, *Science* **323**, 1018 (2009).
- [15] J. Mannhart, and D. G. Schlom, *Oxide Interfaces - An Opportunity for Electronics*, *Science* **327**, 1607 (2010).
- [16] A. Tsukazaki, A. Ohtomo, T. Kita, Y. Ohno, H. Ohno, and M. Kawasaki, *Quantum Hall effect in polar oxide heterostructures*, *Science* **315**, 1388 (2007).
- [17] Pe, ntilde, V. a, Z. Sefrioui, D. Arias, C. Leon, J. Santamaria, J. L. Martinez, S. G. E. te Velthuis, and A. Hoffmann, *Giant Magnetoresistance in Ferromagnet/Superconductor Superlattices*, *Physical Review Letters* **94**, 057002 (2005).
- [18] J. Chakhalian, J. W. Freeland, G. Srajer, J. Stremper, G. Khaliullin, J. C. Cezar, T. Charlton, R. Dalgliesh, C. Bernhard, G. Cristiani, H. U. Habermeier, and B. Keimer, *Magnetism at the interface between ferromagnetic and superconducting oxides*, *Nat Phys* **2**, 244 (2006).
- [19] J. Chakhalian, J. W. Freeland, H. U. Habermeier, G. Cristiani, G. Khaliullin, M. van Veenendaal, and B. Keimer, *Orbital Reconstruction and Covalent Bonding at an Oxide Interface*, *Science* **318**, 1114 (2007).
- [20] N. Ogawa, T. Satoh, Y. Ogimoto, and K. Miyano, *Nonlinear optical detection of a ferromagnetic state at the single interface of an antiferromagnetic LaMnO_3 / SrMnO_3 double layer*, *Physical Review B* **78**, 212409 (2008).

- [21] Y. Tokura, *Multiferroics--toward strong coupling between magnetization and polarization in a solid*, Journal of Magnetism and Magnetic Materials **310**, 1145 (2007).
- [22] Y. Hotta, T. Susaki, and H. Y. Hwang, *Polar discontinuity doping of the $LaVO_3/SrTiO_3$ interface*, Physical Review Letters **99** (2007).
- [23] A. Kalabukhov, R. Gunnarsson, J. Borjesson, E. Olsson, T. Claeson, and D. Winkler, *Effect of oxygen vacancies in the $SrTiO_3$ substrate on the electrical properties of the $LaAlO_3/SrTiO_3$ interface*, Physical Review B **75**, 121404 (2007).
- [24] W. Siemons, G. Koster, H. Yamamoto, W. A. Harrison, G. Lucovsky, T. H. Geballe, D. H. A. Blank, and M. R. Beasley, *Origin of charge density at $LaAlO_3$ on $SrTiO_3$ heterointerfaces: Possibility of intrinsic doping*, Physical Review Letters **98**, 196802 (2007).
- [25] G. Herranz, M. Basletic, M. Bibes, C. Carretero, E. Tafra, E. Jacquet, K. Bouzehouane, C. Deranlot, A. Hamzic, J. M. Broto, A. Barthelemy, and A. Fert, *High mobility in $LaAlO_3/SrTiO_3$ heterostructures: Origin, dimensionality, and perspectives*, Physical Review Letters **98**, 216803 (2007).
- [26] K. Yoshimatsu, R. Yasuhara, H. Kumigashira, and M. Oshima, *Origin of metallic states at the heterointerface between the band insulators $LaAlO_3$ and $SrTiO_3$* , Physical Review Letters **101** (2008).
- [27] O. Copie, V. Garcia, C. Bodefeld, C. Carretero, M. Bibes, G. Herranz, E. Jacquet, J. L. Maurice, B. Vinter, S. Fusil, K. Bouzehouane, H. Jaffres, and A. Barthelemy,

- Towards Two-Dimensional Metallic Behavior at LaAlO₃/SrTiO₃ Interfaces*,
Physical Review Letters **102** (2009).
- [28] C. Bell, S. Harashima, Y. Hikita, and H. Y. Hwang, *Thickness dependence of the mobility at the LaAlO₃/SrTiO₃ interface*, Applied Physics Letters **94** (2009).
- [29] Z. S. Popovic, and S. Satpathy, *Wedge-Shaped Potential and Airy-Function Electron Localization in Oxide Superlattices*, Physical Review Letters **94**, 176805 (2005).
- [30] M. S. Park, S. H. Rhim, and A. J. Freeman, *Charge compensation and mixed valency in LaAlO₃/SrTiO₃ heterointerfaces studied by the FLAPW method*, Physical Review B **74**, 205416 (2006).
- [31] S. Okamoto, A. J. Millis, and N. A. Spaldin, *Lattice Relaxation in Oxide Heterostructures: LaTiO₃/SrTiO₃ Superlattices*, Physical Review Letters **97**, 056802 (2006).
- [32] J. M. Albina, M. Mrovec, B. Meyer, and C. Elsasser, *Structure, stability, and electronic properties of SrTiO₃/LaAlO₃ and SrTiO₃/SrRuO₃ interfaces*, Physical Review B **76**, 165103 (2007).
- [33] R. Pentcheva, and W. E. Pickett, *Charge localization or itineracy at LaAlO₃/SrTiO₃ interfaces: Hole polarons, oxygen vacancies, and mobile electrons*, Physical Review B **74**, 035112 (2006).

- [34] R. Pentcheva, and W. E. Pickett, *Correlation-Driven Charge Order at the Interface between a Mott and a Band Insulator*, Physical Review Letters **99**, 016802 (2007).
- [35] R. Pentcheva, and W. E. Pickett, *Avoiding the Polarization Catastrophe in LaAlO₃ Overlayers on SrTiO₃(001) through Polar Distortion*, Physical Review Letters **102**, 107602 (2009).
- [36] K. Janicka, J. P. Velev, and E. Y. Tsymbal, *Magnetism of LaAlO₃/SrTiO₃ superlattices*, Journal of Applied Physics **103**, 07b508 (2008).
- [37] K. Janicka, J. P. Velev, and E. Y. Tsymbal, *Quantum Nature of Two-Dimensional Electron Gas Confinement at LaAlO₃/SrTiO₃ Interfaces*, Physical Review Letters **102**, 106803 (2009).
- [38] J. Lee, and A. A. Demkov, *Charge origin and localization at the n-type SrTiO₃/LaAlO₃ interface*, Physical Review B **78**, 193104 (2008).
- [39] S. Ishibashi, and K. Terakura, *Analysis of Screening Mechanisms for Polar Discontinuity for LaAlO₃/SrTiO₃ Thin Films Based on Ab initio Calculations*, Journal of the Physical Society of Japan **77**, 104706 (2008).
- [40] Z. C. Zhong, and P. J. Kelly, *Electronic-structure-induced reconstruction and magnetic ordering at the LaAlO₃ vertical bar SrTiO₃ interface*, Epl **84**, 27001 (2008).

- [41] Y. Wang, M. K. Niranjana, J. D. Burton, J. M. An, K. D. Belashchenko, and E. Y. Tsybal, *Prediction of a spin-polarized two-dimensional electron gas at the $\text{LaAlO}_3/\text{EuO}(001)$ interface*, Physical Review B **79**, 212408 (2009).
- [42] H. Chen, A. M. Kolpak, and S. Ismail-Beigi, *Fundamental asymmetry in interfacial electronic reconstruction between insulating oxides: An ab initio study*, Physical Review B **79**, 161402 (2009).
- [43] N. C. Bristowe, E. Artacho, and P. B. Littlewood, *Oxide superlattices with alternating p and n interfaces*, Physical Review B **80**, 045425 (2009).
- [44] A. Ohtomo, and H. Y. Hwang, *A high-mobility electron gas at the $\text{LaAlO}_3/\text{SrTiO}_3$ heterointerface*, Nature **427**, 423 (2004).
- [45] H. Chen, A. M. Kolpak, and S. Ismail-Beigi, *Electronic and Magnetic Properties of $\text{SrTiO}_3/\text{LaAlO}_3$ Interfaces from First Principles*, Advanced Materials **22**, 2881 (2010).
- [46] S. Thiel, G. Hammerl, A. Schmehl, C. W. Schneider, and J. Mannhart, *Tunable Quasi-Two-Dimensional Electron Gases in Oxide Heterostructures*, Science **313**, 1942 (2006).
- [47] C. Cen, S. Thiel, J. Mannhart, and J. Levy, *Oxide Nanoelectronics on Demand*, Science **323**, 1026 (2009).
- [48] A. Brinkman, M. Huijben, M. van Zalk, J. Huijben, U. Zeitler, J. C. Maan, W. G. van der Wiel, G. Rijnders, D. H. A. Blank, and H. Hilgenkamp, *Magnetic effects at the interface between non-magnetic oxides*, Nature Materials **6**, 493 (2007).

- [49] M. Ben Shalom, C. W. Tai, Y. Lereah, M. Sachs, E. Levy, D. Rakhmilevitch, A. Palevski, and Y. Dagan, *Anisotropic magnetotransport at the SrTiO₃/LaAlO₃ interface*, Physical Review B **80**, 140403 (2009).
- [50] N. Reyren, S. Thiel, A. D. Caviglia, L. F. Kourkoutis, G. Hammerl, C. Richter, C. W. Schneider, T. Kopp, A. S. Ruetschi, D. Jaccard, M. Gabay, D. A. Muller, J. M. Triscone, and J. Mannhart, *Superconducting Interfaces Between Insulating Oxides*, Science **317**, 1196 (2007).
- [51] M. Basletic, J. L. Maurice, C. Carretero, G. Herranz, O. Copie, M. Bibes, E. Jacquet, K. Bouzehouane, S. Fusil, and A. Barthelemy, *Mapping the spatial distribution of charge carriers in LaAlO₃/SrTiO₃ heterostructures*, Nat Mater **7**, 621 (2008).
- [52] W. J. Son, E. Cho, B. Lee, J. Lee, and S. Han, *Density and spatial distribution of charge carriers in the intrinsic n-type LaAlO₃-SrTiO₃ interface*, Physical Review B **79**, 245411 (2009).
- [53] N. Nakagawa, H. Y. Hwang, and D. A. Muller, *Why some interfaces cannot be sharp*, Nat Mater **5**, 204 (2006).
- [54] P. R. Willmott, S. A. Pauli, R. Herger, C. M. Schlepütz, D. Martocchia, B. D. Patterson, B. Delley, R. Clarke, D. Kumah, C. Cionca, and Y. Yacoby, *Structural basis for the conducting interface between LaAlO₃ and SrTiO₃*, Physical Review Letters **99** (2007).

- [55] G. A. Baraff, J. A. Appelbaum, and D. R. Hamann, *Self-Consistent Calculation of the Electronic Structure at an Abrupt GaAs-Ge Interface*, Physical Review Letters **38**, 237 (1977).
- [56] T. Higuchi, Y. Hotta, T. Susaki, A. Fujimori, and H. Y. Hwang, *Modulation doping of a Mott quantum well by a proximate polar discontinuity*, Physical Review B **79**, 075415 (2009).
- [57] G. Singh-Bhalla, C. Bell, J. Ravichandran, W. Siemons, Y. Hikita, S. Salahuddin, A. F. Hebard, H. Y. Hwang, and R. Ramesh, *Built-in and induced polarization across LaAlO₃/SrTiO₃ heterojunctions*, Nature Physics **7**, 80 (2010).
- [58] M. Takizawa, Y. Hotta, T. Susaki, Y. Ishida, H. Wadati, Y. Takata, K. Horiba, M. Matsunami, S. Shin, M. Yabashi, K. Tamasaku, Y. Nishino, T. Ishikawa, A. Fujimori, and H. Y. Hwang, *Spectroscopic Evidence for Competing Reconstructions in Polar Multilayers LaAlO₃/LaVO₃/LaAlO₃*, Physical Review Letters **102**, 236401 (2009).
- [59] H. P. R. Frederikse, and W. R. Hosler, *Hall Mobility in SrTiO₃*, Physical Review **161**, 822 (1967).
- [60] Y. Tokura, Y. Taguchi, Y. Okada, Y. Fujishima, T. Arima, K. Kumagai, and Y. Iye, *Filling dependence of electronic properties on the verge of metal–Mott-insulator transition in Sr_{1-x}La_xTiO₃*, Physical Review Letters **70**, 2126 (1993).
- [61] P. Hohenberg, and W. Kohn, *Inhomogeneous Electron Gas*, Physical Review **136**, B864 (1964).

- [62] W. Kohn, and L. J. Sham, *Self-Consistent Equations Including Exchange and Correlation Effects*, Physical Review **140**, A1133 (1965).
- [63] W. M. C. Foulkes, L. Mitas, R. J. Needs, and G. Rajagopal, *Quantum Monte Carlo simulations of solids*, Reviews of Modern Physics **73**, 33 (2001).
- [64] W. G. Aulbur, L. Jonsson, J. W. Wilkins, E. Henry, and S. Frans, in *Solid State Physics* (Academic Press, 1999), pp. 1.
- [65] E. Kaxiras, *Atomic and electronic structure of solids* (Cambridge University Press, Cambridge, UK; New York, 2003).
- [66] J. P. Perdew, and A. Zunger, *Self-interaction correction to density-functional approximations for many-electron systems*, Physical Review B **23**, 5048 (1981).
- [67] R. M. Martin, *Electronic structure : basic theory and practical methods* (Cambridge University Press, Cambridge, UK; New York, 2004).
- [68] A. D. Becke, *Density-functional exchange-energy approximation with correct asymptotic behavior*, Physical Review A **38**, 3098 (1988).
- [69] J. P. Perdew, and Y. Wang, *Accurate and simple analytic representation of the electron-gas correlation energy*, Physical Review B **45**, 13244 (1992).
- [70] J. P. Perdew, K. Burke, and M. Ernzerhof, *Generalized Gradient Approximation Made Simple*, Physical Review Letters **77**, 3865 (1996).
- [71] J. Hubbard, *Electron Correlations in Narrow Energy Bands. IV. The Atomic Representation*, Proceedings of the Royal Society of London. Series A, Mathematical and Physical Sciences **285**, 542 (1965).

- [72] V. I. Anisimov, F. Aryasetiawan, and A. I. Lichtenstein, *First-principles calculations of the electronic structure and spectra of strongly correlated systems: the LDA+ U method*, Journal of Physics: Condensed Matter **9**, 767 (1997).
- [73] A. I. Liechtenstein, V. I. Anisimov, and J. Zaanen, *Density-functional theory and strong interactions: Orbital ordering in Mott-Hubbard insulators*, Physical Review B **52**, R5467 (1995).
- [74] N. W. Ashcroft, and N. D. Mermin, *Solid state physics* (Holt, Rinehart and Winston, New York, 1976).
- [75] M. C. Payne, M. P. Teter, D. C. Allan, T. A. Arias, and J. D. Joannopoulos, *Iterative minimization techniques for ab initio total-energy calculations: molecular dynamics and conjugate gradients*, Reviews of Modern Physics **64**, 1045 (1992).
- [76] N. Troullier, and J. L. Martins, *Efficient pseudopotentials for plane-wave calculations*, Physical Review B **43**, 1993 (1991).
- [77] D. Vanderbilt, *Soft self-consistent pseudopotentials in a generalized eigenvalue formalism*, Physical Review B **41**, 7892 (1990).
- [78] P. E. Blöchl, *Projector augmented-wave method*, Physical Review B **50**, 17953 (1994).
- [79] G. Kresse, and J. Furthmüller, *Efficient iterative schemes for ab initio total-energy calculations using a plane-wave basis set*, Physical Review B **54**, 11169 (1996).

- [80] H. J. Monkhorst, and J. D. Pack, *Special points for Brillouin-zone integrations*, Physical Review B **13**, 5188 (1976).
- [81] E.R. Davidson, *Methods in Computational Molecular Physics* edited by G.H.F. Diercksen and S. Wilson Vol. 113 NATO Advanced Study Institute, Series C (Plenum, New York, 1983), p. 95
- [82] P. Pulay, *Convergence acceleration of iterative sequences. the case of scf iteration*, Chemical Physics Letters **73**, 393 (1980).
- [83] D. M. Wood, and A. Zunger, *A new method for diagonalising large matrices*, Journal of Physics A: Mathematical and General **18**, 1343 (1985).
- [84] J. Hafner, *Ab-initio simulations of materials using VASP: Density-functional theory and beyond*, Journal of Computational Chemistry **29**, 2044 (2008).
- [85] M. Shishkin, and G. Kresse, *Implementation and performance of the frequency-dependent GW method within the PAW framework*, Physical Review B **74**, 035101 (2006).
- [86] F. Furche, *Molecular tests of the random phase approximation to the exchange-correlation energy functional*, Physical Review B **64**, 195120 (2001).
- [87] E. Y. Tsymbal, and H. Kohlstedt, *Tunneling Across a Ferroelectric*, Science **313**, 181 (2006).
- [88] Goldschmidt V M, Skr. Norske Vidensk.-Akad., Mat.-Naturv. Kl. No 2 , 1926
- [89] K. M. Rabe, C. H. Ahn, and J.-M. Triscone, *Physics of ferroelectrics : a modern perspective* (Springer, Berlin; New York, 2007).

- [90] C.-Z. Wang, R. Yu, and H. Krakauer, *Polarization dependence of Born effective charge and dielectric constant in KNbO_3* , Physical Review B **54**, 11161 (1996).
- [91] C. Cen, S. Thiel, G. Hammerl, C. W. Schneider, K. E. Andersen, C. S. Hellberg, J. Mannhart, and J. Levy, *Nanoscale control of an interfacial metal-insulator transition at room temperature*, Nat Mater **7**, 298 (2008).
- [92] S. Won-joon, and et al., *Hydrogen adsorption and carrier generation in LaAlO_3 - SrTiO_3 heterointerfaces: a first-principles study*, Journal of Physics: Condensed Matter **22**, 315501 (2010).
- [93] F. Bi, D. F. Bogorin, C. Cen, C. W. Bark, J.-W. Park, C.-B. Eom, and J. Levy, *“Water-cycle” mechanism for writing and erasing nanostructures at the $\text{LaAlO}_3/\text{SrTiO}_3$ interface*, Applied Physics Letters **97**, 173110 (2010).
- [94] T. Kamiya and M. Kawasaki, MRS Bull. **33**, 1061 (2008)
- [95] D. R. Hang, C. F. Huang, and Y. F. Chen, *Two-subband-populated $\text{AlGaIn}/\text{GaIn}$ heterostructures probed by electrically detected and microwave-modulated magnetotransport measurements*, Applied Physics Letters **89**, 092116 (2006).
- [96] E. D. Murray, and D. Vanderbilt, *Theoretical investigation of polarization-compensated II-IV/I-V perovskite superlattices*, Physical Review B **79**, 100102 (2009).
- [97] K. Nassau, and A. E. Miller, *Strontium titanate: An index to the literature on properties and the growth of single crystals*, Journal of Crystal Growth **91**, 373 (1988).

- [98] C. G. Duan, R. F. Sabirianov, W. N. Mei, S. S. Jaswal, and E. Y. Tsymbal, *Interface Effect on Ferroelectricity at the Nanoscale*, Nano Lett. **6**, 483 (2006).
- [99] N. Sai, A. M. Kolpak, and A. M. Rappe, *Ferroelectricity in ultrathin perovskite films*, Physical Review B **72**, 020101 (2005).
- [100] Y. Kuroiwa, S. Aoyagi, A. Sawada, J. Harada, E. Nishibori, M. Takata, and M. Sakata, *Evidence for Pb-O Covalency in Tetragonal PbTiO₃*, Physical Review Letters **87**, 217601 (2001).
- [101] Y. Umeno, B. Meyer, C. Elsasser, and P. Gumbsch, *Ab initio study of the critical thickness for ferroelectricity in ultrathin Pt/PbTiO₃/Pt films*, Physical Review B **74**, 060101 (2006).
- [102] R. D. King-Smith, and D. Vanderbilt, *Theory of polarization of crystalline solids*, Physical Review B **47**, 1651 (1993).
- [103] O. Nakagawara, T. Shimuta, T. Makino, S. Arai, H. Tabata, and T. Kawai, *Dependence of dielectric and ferroelectric behaviors on growth orientation in epitaxial BaTiO₃/SrTiO₃ superlattices*, Vacuum **66**, 397 (2002).
- [104] W. Kleemann, F. J. Schäfer, and M. D. Fontana, *Crystal optical studies of spontaneous and precursor polarization in KNbO₃*, Physical Review B **30**, 1148 (1984).
- [105] T. Morita, and Y. Cho, *Epitaxial PbTiO₃ Thin Films on SrTiO₃ (100) and SrRuO₃/SrTiO₃ (100) Substrates Deposited by a Hydrothermal Method*, Japanese Journal of Applied Physics **43**, 6535 (2004).

- [106] J. B. Neaton, and K. M. Rabe, *Theory of polarization enhancement in epitaxial BaTiO₃/SrTiO₃ superlattices*, Applied Physics Letters **82**, 1586 (2003).
- [107] T. Neumann, G. Borstel, C. Scharfschwerdt, and M. Neumann, *Electronic structure of KNbO₃ and KTaO₃*, Physical Review B **46**, 10623 (1992).
- [108] J. Robertson, and C. W. Chen, *Schottky barrier heights of tantalum oxide, barium strontium titanate, lead titanate, and strontium bismuth tantalate*, Applied Physics Letters **74**, 1168 (1999).
- [109] P. W. Peacock, and J. Robertson, *Band offsets and Schottky barrier heights of high dielectric constant oxides*, Journal of Applied Physics **92**, 4712 (2002).
- [110] R. E. Cohen, *Ferroelectricity origins*, Nature **362**, 213 (1993).
- [111] J. Junquera, and P. Ghosez, *Critical thickness for ferroelectricity in perovskite ultrathin films*, Nature **422**, 506 (2003).
- [112] J. H. Haeni, P. Irvin, W. Chang, R. Uecker, P. Reiche, Y. L. Li, S. Choudhury, W. Tian, M. E. Hawley, B. Craigo, A. K. Tagantsev, X. Q. Pan, S. K. Streiffer, L. Q. Chen, S. W. Kirchoefer, J. Levy, and D. G. Schlom, *Room-temperature ferroelectricity in strained SrTiO₃*, Nature **430**, 758 (2004).
- [113] X. Wu, and D. Vanderbilt, *Theory of hypothetical ferroelectric superlattices incorporating head-to-head and tail-to-tail 180[degree] domain walls*, Physical Review B **73**, 020103 (2006).

- [114] M. Chu, Y. Sun, U. Aghoram, and S. E. Thompson, *Strain: A Solution for Higher Carrier Mobility in Nanoscale MOSFETs*, Annual Review of Materials Research **39**, 203 (2009).
- [115] J. Welser, J. L. Hoyt, and J. F. Gibbons, *Electron-mobility enhancement in strained-si n-type metal-oxide-semiconductor field-effect transistors*, IEEE Electron Device Lett. **15**, 100 (1994).
- [116] K. J. Choi, M. Biegalski, Y. L. Li, A. Sharan, J. Schubert, R. Uecker, P. Reiche, Y. B. Chen, X. Q. Pan, V. Gopalan, L. Q. Chen, D. G. Schlom, and C. B. Eom, *Enhancement of ferroelectricity in strained BaTiO₃ thin films*, Science **306**, 1005 (2004).
- [117] M. P. Warusawithana, C. Cen, C. R. Slesman, J. C. Woicik, Y. L. Li, L. F. Kourkoutis, J. A. Klug, H. Li, P. Ryan, L. P. Wang, M. Bedzyk, D. A. Muller, L. Q. Chen, J. Levy, and D. G. Schlom, *A Ferroelectric Oxide Made Directly on Silicon*, Science **324**, 367 (2009).
- [118] J. W. Reiner, A. M. Kolpak, Y. Segal, K. F. Garrity, S. Ismail-Beigi, C. H. Ahn, and F. J. Walker, *Crystalline Oxides on Silicon*, Advanced Materials **22**, 2919 (2010).
- [119] R. Wordenweber, E. Hollmann, R. Kutzner, and J. Schubert, *Induced ferroelectricity in strained epitaxial SrTiO₃ films on various substrates*, Journal of Applied Physics **102**, 044119 (2007).

- [120] A. Gozar, G. Logvenov, L. F. Kourkoutis, A. T. Bollinger, L. A. Giannuzzi, D. A. Muller, and I. Bozovic, *High-temperature interface superconductivity between metallic and insulating copper oxides*, *Nature* **455**, 782 (2008).
- [121] A. Ohtomo, D. A. Muller, J. L. Grazul, and H. Y. Hwang, *Artificial charge-modulation in atomic-scale perovskite titanate superlattices*, *Nature* **419**, 378 (2002).
- [122] H. W. Jang, A. Kumar, S. Denev, M. D. Biegalski, P. Maksymovych, C. W. Bark, C. T. Nelson, C. M. Folkman, S. H. Baek, N. Balke, C. M. Brooks, D. A. Tenne, D. G. Schlom, L. Q. Chen, X. Q. Pan, S. V. Kalinin, V. Gopalan, and C. B. Eom, *Ferroelectricity in Strain-Free SrTiO₃ Thin Films*, *Physical Review Letters* **104**, 4 (2010).
- [123] M. K. Niranjan, Y. Wang, S. S. Jaswal, and E. Y. Tsymbal, *Prediction of a Switchable Two-Dimensional Electron Gas at Ferroelectric Oxide Interfaces*, *Physical Review Letters* **103**, 016804 (2009).
- [124] Y. Wang, M. K. Niranjan, S. S. Jaswal, and E. Y. Tsymbal, *First-principles studies of a two-dimensional electron gas at the interface in ferroelectric oxide heterostructures*, *Physical Review B* **80**, 165130 (2009).
- [125] S. Lee, J. Jiang, Y. Zhang, C. W. Bark, J. D. Weiss, C. Tarantini, C. T. Nelson, H. W. Jang, C. M. Folkman, S. H. Baek, A. Polyanskii, D. Abaimov, A. Yamamoto, J. W. Park, X. Q. Pan, E. E. Hellstrom, D. C. Larbalestier, and C. B. Eom,

- Template engineering of Co-doped BaFe₂As₂ single-crystal thin films*, Nature Materials **9**, 397 (2010).
- [126] J. W. Park, S. H. Baek, C. W. Bark, M. D. Biegalski, and C. B. Eom, *Quasi-single-crystal (001) SrTiO₃ templates on Si*, Applied Physics Letters **95**, 3 (2009).
- [127] J. W. Park, D. F. Bogorin, C. Cen, D. A. Felker, Y. Zhang, C. T. Nelson, C. W. Bark, C. M. Folkman, X. Q. Pan, M. S. Rzchowski, J. Levy, and C. B. Eom, *Creation of a two-dimensional electron gas at an oxide interface on silicon*, Nat. Commun. **1**, 6 (2010).
- [128] G. Kresse, and J. Furthmuller, *Efficiency of ab-initio total energy calculations for metals and semiconductors using a plane-wave basis set*, Comput. Mater. Sci. **6**, 15 (1996).
- [129] R. Resta, *Theory of the electric polarization in crystals*, Ferroelectrics **136**, 51 (1992).
- [130] Y. Segal, J. H. Ngai, J. W. Reiner, F. J. Walker, and C. H. Ahn, *X-ray photoemission studies of the metal-insulator transition in LaAlO₃/SrTiO₃ structures grown by molecular beam epitaxy*, Physical Review B **80**, 241107 (2009).
- [131] B. R. K. Nanda, and S. Satpathy, *Spin-Polarized Two-Dimensional Electron Gas at Oxide Interfaces*, Physical Review Letters **101**, 127201 (2008).

- [132] A. Mauger, and C. Godart, *The magnetic, optical, and transport properties of representatives of a class of magnetic semiconductors: The europium chalcogenides*, Physics Reports **141**, 51 (1986).
- [133] P. G. Steeneken, L. H. Tjeng, I. Elfimov, G. A. Sawatzky, G. Ghiringhelli, N. B. Brookes, and D. J. Huang, *Exchange Splitting and Charge Carrier Spin Polarization in EuO*, Physical Review Letters **88**, 047201 (2002).
- [134] A. Schmehl, V. Vaithyanathan, A. Herrnberger, S. Thiel, C. Richter, M. Liberati, T. Heeg, M. Rockerath, L. F. Kourkoutis, S. Muhlbauer, P. Boni, D. A. Muller, Y. Barash, J. Schubert, Y. Idzerda, J. Mannhart, and D. G. Schlom, *Epitaxial integration of the highly spin-polarized ferromagnetic semiconductor EuO with silicon and GaN*, Nat Mater **6**, 882 (2007).
- [135] H. Miyazaki, H. J. Im, K. Terashima, S. Yagi, M. Kato, K. Soda, T. Ito, and S. Kimura, *La-doped EuO: A rare earth ferromagnetic semiconductor with the highest Curie temperature*, Applied Physics Letters **96**, 232503.
- [136] P. H. Dederichs, Bl, uuml, S. gel, R. Zeller, and H. Akai, *Ground States of Constrained Systems: Application to Cerium Impurities*, Physical Review Letters **53**, 2512 (1984).
- [137] I. V. Solovyev, *Combining DFT and many-body methods to understand correlated materials*, Journal of Physics: Condensed Matter **20**, 293201 (2008).

- [138] G. Busch, and P. Wachter, *Einfluß der magnetischen Ordnung auf die optische Absorption von ferro- oder antiferromagnetischen Halbleitern*, Zeitschrift für Physik B Condensed Matter **5**, 232 (1966).
- [139] R. Schiller, and W. Nolting, *Prediction of a Surface State and a Related Surface Insulator-Metal Transition for the (100) Surface of Stoichiometric EuO*, Physical Review Letters **86**, 3847 (2001).
- [140] D. E. Eastman, F. Holtzberg, and S. Methfessel, *Photoemission Studies of the Electronic Structure of EuO, EuS, EuSe, And GdS*, Physical Review Letters **23**, 226 (1969).
- [141] J. Lee, N. Sai, and A. A. Demkov, *Spin-polarized two-dimensional electron gas through electrostatic doping in LaAlO₃/EuO heterostructures*, Physical Review B **82**, 235305 (2010).

Publications

1. “Metallic and insulating oxide interfaces controlled by electronic correlations”
H. W. Jang, D. A. Felker, C. W. Bark, **Y. Wang**, M. K. Niranjan, C. T. Nelson, Y. Zhang, D. Su, C. M. Folkman, S. H. Baek, S. Lee, K. Janicka, Y. Zhu, X. Q. Pan, D. D. Fong, E. Y. Tsymbal, M. S. Rzchowski and C. B. Eom, *Science* **331**, 886 (2011)
2. “Tailoring a two-dimensional electron gas at the LaAlO₃/SrTiO₃ (001) interface by epitaxial strain”
C. W. Bark, D. A. Felker, **Y. Wang**, Y. Zhang, H. W. Jang, C. M. Folkman, J. W. Park, S. H. Baek, X. Q. Pan, E. Y. Tsymbal, M. S. Rzchowski and C. B. Eom, *Proceedings of National Academy of Sciences*, **108**, 4720 (2011)
3. “Ferroelectric dead layer driven by a polar interface”
Y. Wang, M. K. Niranjan, K. Janicka, J. P. Velev, M. Y. Zhuravlev, S. S. Jaswal, and E. Y. Tsymbal, *Physical Review B* **82**, 094114 (2010)
4. “First-principles studies of a two-dimensional electron gas at the interface in ferroelectric oxide heterostructures”
Y. Wang, M. K. Niranjan, S. S. Jaswal, and E. Y. Tsymbal, *Physical Review B* **80**, 165130 (2009)

5. “Prediction of a spin-polarized two-dimensional electron gas at the LaAlO₃/EuO(001) interface”

Y. Wang, M. K. Niranjana, J. D. Burton, J. M. An, K. D. Belashchenko, and E. Y. Tsymbal, *Physical Review B* **79**, 212408 (2009)

6. “Prediction of a switchable two-dimensional electron gas at ferroelectric oxide interfaces”

M. K. Niranjana, **Y. Wang**, S. S. Jaswal, and E. Y. Tsymbal, *Physical Review Letters* **103**, 016804 (2009)

7. “Tunneling electroresistance in ferroelectric tunnel junctions with a composite barrier”

M. Y. Zhuravlev, **Y. Wang**, S. Maekawa, and E. Y. Tsymbal, *Applied Physics Letters* **95**, 052902 (2009)

8. “Tunneling electroresistance effect in ferroelectric tunnel junctions at the nanoscale”

A. Gruverman, D. Wu, H. Lu, **Y. Wang**, H. W. Jang, C. M. Folkman, M. Y. Zhuravlev, D. Felker, M. Rzchowski, C. B. Eom, and E. Y. Tsymbal, *Nano Letters* **9**, 3539 (2009)

Presentations

1. **Y. Wang**, M. K. Niranjana, K. Janicka, J. P. Velev, M. Y. Zhuravlev, S. S. Jaswal, and E. Y. Tsymbal, “Effect of polar interfaces on thin-film ferroelectricity”, *APS March Meeting*, Dallas, Texas, March 2011
2. **Y. Wang**, M. K. Niranjana, K. Janicka, J. P. Velev, M. Y. Zhuravlev, S. S. Jaswal, and E. Y. Tsymbal, “Critical thickness of ferroelectric thin films controlled by polar interfaces”, *MRS Spring Meeting*, San Francisco, CA, April 2011
3. **Y. Wang**, M. K. Niranjana, J. D. Burton, J. M. An, K. D. Belashchenko, and E. Y. Tsymbal, “Prediction of a spin-polarized two-dimensional electron gas at the $\text{LaAlO}_3/\text{EuO}(001)$ Interface”, *APS March Meeting*, Portland, Oregon, March 2010
4. Mikhail Y. Zhuravlev, **Yong Wang**, Sadamichi Maekawa and Evgeny Y. Tsymbal, “Tunneling electroresistance effect in ferroelectric tunnel junctions with a composite barrier”, *APS March Meeting*, Portland, Oregon, March 2010
5. **Y. Wang**, M. K. Niranjana, J. D. Burton, J. M. An, K. D. Belashchenko, and E. Y. Tsymbal, “Prediction of a spin-polarized two-dimensional electron gas at the $\text{LaAlO}_3/\text{EuO}(001)$ Interface”, *11th Joint MMM-Intermag Conference*, Washington, DC, January 2010
6. **Yong Wang**, Manish K. Niranjana, Sitaram S. Jaswal and Evgeny Y. Tsymbal, “Prediction of a switchable two-dimensional electron gas at ferroelectric $\text{KNbO}_3/\text{ATiO}_3$ ($A = \text{Sr}, \text{Ba}, \text{Pb}$) interfaces”, *MRS Fall Meeting*, Boston, MA,

November 2009

7. **Y. Wang**, M. K. Niranjana, J. D. Burton, J. M. An, K. D. Belashchenko, and E. Y. Tsybal, "Prediction of a Spin-Polarized Two-Dimensional Electron Gas at the $\text{LaAlO}_3/\text{EuO}(001)$ Interface", *MRS Fall Meeting*, Boston, MA, November 2009
8. Mikhail Y. Zhuravlev, **Yong Wang**, Sadamichi Maekawa and Evgeny Y. Tsybal, "Tunneling electroresistance effect in ferroelectric tunnel junctions with a composite barrier", *MRS Fall Meeting 2009*, Boston, MA, November 2009
9. **Yong Wang**, Manish Niranjana, Sitaram Jaswal, Evgeny Tsybal, "Prediction of a switchable two-dimensional electron gas at $\text{KNbO}_3/\text{ATiO}_3$ (A=Sr, Ba, Pb) interfaces", *55th Midwest Solid State Conference*, Iowa, April 2009
10. **Yong Wang**, Manish Niranjana, Sitaram Jaswal, Evgeny Tsybal, "Prediction of a switchable two-dimensional electron gas at $\text{KNbO}_3/\text{ATiO}_3$ (A = Sr, Ba, Pb) interfaces", *APS March Meeting*, Pittsburgh, Pennsylvania, March 2009
11. **Yong Wang**, Jihee Kim, Nick Reding, Kristin Kraemer, Stephen Ducharme, Zhongxin Ge, James M. Takacs, "Structure of Langmuir-Blodgett Films of Vinylidene Fluoride Oligomers", *54th Midwest Solid State Conference*, Lincoln, NE, October 2007